Quantitative Prediction of Crystal Nucleation Rates for Spherical Colloids: A Computational Study

Quantitative Prediction of Crystal Nucleation Rates for Spherical Colloids: A Computational Study

ACADEMISCH PROEFSCHRIFT

ter verkrijging van de graad van doctor
aan de Universiteit van Amsterdam,
op gezag van de Rector Magnificus
Prof.dr. P. F. van der Heijden ten overstaan van een
door het college voor promoties ingestelde commissie,
in het openbaar te verdedigen in de Aula der Universiteit
op woensdag 27 november 2002 te 12.00 uur door

Stefan Alexander Auer
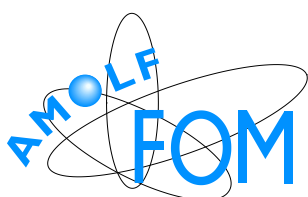geboren te Stuttgart

Promotor:

- Prof.dr. D. Frenkel, Universiteit van Amsterdam

Overige leden:

- Prof.dr. B. Smit, Universiteit van Amsterdam

- Dr. G.H. Wegdam , Universiteit van Amsterdam

- Prof.dr. J. Walraven, Universiteit van Amsterdam

- Prof.dr. A. van Blaaderen, Universiteit Utrecht

- Prof.dr. T. Palberg, Johannes Gutenberg-Universität, Mainz

- Prof.dr. W.C.K. Poon, University of Edingburgh

Faculteit: Natuurwetenschappen, Wiskunde en Informatica

The following papers are based on this thesis:

- Chapter 5:
  Prediction of absolute crystal-nucleation rate in hard-sphere colloids,
  S. Auer and D. Frenkel, Nature **409**, 1020 (2001).

- Chapter 6:
  *Suppression of crystal nucleation in polydisperse colloids
  due to increase of the surface free energy*,
  S. Auer and D. Frenkel, Nature **413**, 711 (2001).

  Related news and views article:
  Diversity suppresses growth,
  D. Oxtoby, Nature **413**, 694 (2001).

- Chapter 7:
  Crystallization of weakly charged colloidal spheres: A numerical study
  S. Auer and D. Frenkel, J. Phys.: Condens. Matter **14**, 7667 (2002).

Other publications by the author of this thesis:

- *Computersimulaties onthullen mechanisme van kristalnucleatie*,
  S. Auer, P. R. ten Wolde and D. Frenkel,
  Nederlands Tijdschrift voor Natuurkunde, **68**, 50 (2002).

Contents

1

Introduction

1.1 Nucleation rate experiments and classical nucleation theory

Heating a block of ice will result in melting. Cooling the resulting water will freeze it again. Water and ice can coexist at only one temperature. This temperature is so important for everyday life, that it has been defined as the zero-point of the most widely used temperature scale invented by the Swedish physicist Celsius. A closer inspection of this melting and freezing transition showed that this transition is not so symmetric. Ice heated above $0°$ C always melts, whereas cooling it below $0°$ C does not result immediately in freezing. In fact water and most other liquids can be cooled significantly below their freezing temperature and kept there without crystallizing [1,2]. This phenomena is known as undercooling. An undercooled liquid can be triggered into freezing by adding a little bit of the corresponding solid. A single snowflake in a glass of undercooled water will induce freezing of water that touches it and grow rapidly into a big chunk of ice. Other disturbances, such as dust or even shocks, can trigger the freezing of undercooled liquids as well. It thus seems that the freezing process has great difficulty to start spontaneously, but becomes very easy once it is started. The spontaneous formation of a piece of solid is an example of nucleation.

The fact that a liquid can be undercooled is best understood qualitatively in the framework of classical nucleation theory (CNT). According to CNT the free energy of a spherical nucleus that forms in a supersaturated solution contains two terms. The first is a bulk term, which takes care of the fact that the solid phase is more stable than the liquid. This term is negative and proportional to the volume of the nucleus. The second term is the surface term which describes the free energy needed to create a liquid-solid interface. This term is positive and proportional to the surface area of the nucleus. The (Gibbs) free energy of a spherical nucleus of radius R has the following form:

$$\Delta G = \frac{4}{3}\pi R^3 \rho_s \Delta\mu + 4\pi R^2 \gamma, \tag{1.1}$$

where ρ_s is the number density of the bulk solid, $\Delta\mu$ the difference in chemical potential between the liquid and the solid, and γ is the liquid-solid surface free energy density. The function ΔG goes through a maximum at $R = 2\gamma/(\rho_s|\Delta\mu|)$ and the corresponding height of the nucleation barrier is given by

$$\Delta G_{\mathrm{crit}} = \frac{16\pi}{3}\frac{\gamma^3}{(\rho_s|\Delta\mu|)^2}. \tag{1.2}$$

For small nuclei the surface term dominates and the free energy increases. Only if this nucleus exceeds a critical size does its free energy decrease and the liquid start to crystallize, see Fig. 1.1.
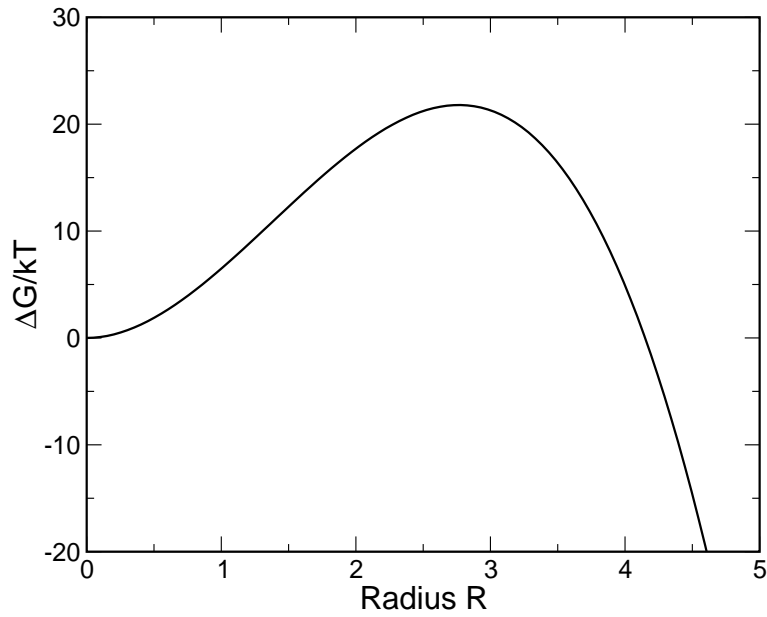
Figure 1.1: Free energy barrier of a spherical nucleus described by classical nucleation theory Eq. (1.1). For small radii the surface term dominates and the free energy increases. The function then goes through a maximum and for larger radii the bulk term dominates and the free energy decreases.

We note from the above equation that for a constant surface free energy γ the nucleation barrier decreases with supersaturation $\Delta\mu$. The probability for the formation of a critical nucleus depends exponentially on its free energy of formation:

$$P_{crit} \propto \exp(-\Delta G_{crit}/k_B T). \tag{1.3}$$

The crystal nucleation rate is given by the product of P_{crit} and a kinetic factor κ, which describes the rate with which a critical nucleus grows, and the corresponding expression from CNT is:

$$I = \kappa \exp\left[-\frac{16\pi}{3k_B T}\frac{\gamma^3}{(\rho_s|\Delta\mu|)^2}\right], \tag{1.4}$$

with $\kappa = 24\rho_l Z D_S n_{crit}^{2/3}/\lambda^2$. Here ρ_l is the number density of the liquid, $Z = \sqrt{|\Delta\mu|/6\pi k_B T n_{crit}}$ is the Zeldovitch factor, D_S is a self-diffusion coefficient and λ is a typical diffusion distance for particles to attach to the critical nucleus. The above expression for the nucleation rate is the one most commonly used to analyse crystal nucleation rate experiments. The problem with the CNT approach is however that, in most cases, neither λ nor γ are accurately known. Both parameters are used to fit the experimental observations. The result is often that estimates for the kinetic prefactor seem unphysical. To illustrate the problems that can arise from this approach we give two examples.

Let us start with Turnbull's first quantitative measurement of a nucleation rate in liquid mercury [2], see Fig. 1.2. For the interpretation of his data he used Eq. (1.4), where he estimated the difference in chemical potential between the two phases by $\Delta\mu \approx \Delta h(T_m - T)/T_m$. Here Δh is the enthalpy change per particle on freezing at coexistence, T_m is the coexistence temperature and T is the temperature of the liquid mercury. A plot of $\log(I)$ versus $1/T\Delta T^2$ should give a straight line with the slope proportional to γ^3 and the intercept equal to $\log(\kappa)$. From this two parameter fit we see that the functional form given by CNT for the nucleation rate reproduces
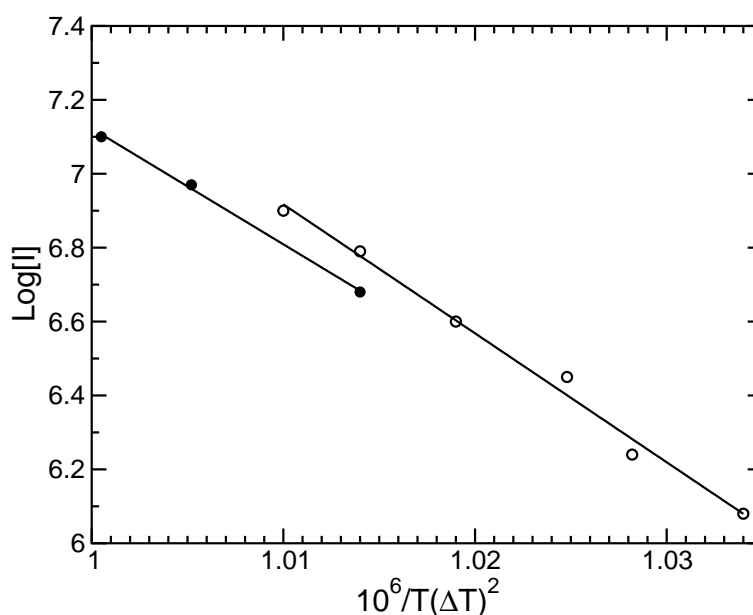
Figure 1.2: The steady state nucleation rate, I in units of $1/(m^3s)$, as a function of undercooling in Kelvin for liquid mercury from Ref. [2]. The open and the filled circles correspond to two different samples. The solid lines result from a two parameter fit of Eq. (1.4) to the experimental data.

the experimental data. However, the resulting value of κ is about 10^7 larger than predicted from CNT. The corresponding estimate for the typical diffusion constant λ is many orders of magnitude too small. To explain this Turnbull noted is his paper: *...suppose that γ depends upon temperature according to the equation:* $\gamma = \gamma_0 + bT$, [where γ_0 is the value at coexistence and b is a constant], ... *a value of b=0.0008/K is sufficient to change the apparent value of the kinetic factor by six orders of magnitude.* A remarkable statement which might be correct, but at the time direct corroboration was not possible because of the absence of a priori knowledge of both fit parameters.

The major problem of experimental investigations of crystallization kinetics in atomic systems is the high speed of nucleus formation and subsequent crystal growth, as well as the difficulty of preventing heterogeneous nucleation. The second example we take from more recent experiments on the crystallization kinetics in a suspension of hard-sphere colloids. Crystallization in colloidal suspensions is interesting because it can be studied in considerable detail, since colloidal particles are much larger than atoms. Colloids therefore crystallize on a timescale which is about ten orders of magnitude longer than that for an atomic liquid. Moreover because of their size, colloids can be probed by powerful optical methods such as time-resolved static laser light scattering and confocal microscopy. In these systems it is also somewhat easier to control heterogeneous nucleation. In Fig. 1.3 we show the results from crystallization rate measurements in hard-sphere colloids, performed by two different groups [3,4]. For this system the difference in chemical potential between the two phases can be calculated accurately from existing analytical expressions for the equation of state. The curves in the figure result from a two parameter fit of Eq. (1.4) to the experimental data. Palberg [5] fitted the data from Harland and van Megen [3] and obtained $\gamma = 0.5k_BT/\sigma^2$ and $\lambda = 17d_{NN}$, while for the data from Heymann et al. [4] he found $\gamma = 0.54k_BT/\sigma^2$ and $\lambda = 2.8d_{NN}$, where σ is the particle diameter and d_{NN} is the nearest neighbor distance. Again, the functional form is described well by the CNT expression for the nucleation rate. The estimates for the surface free energy are now known to be rather
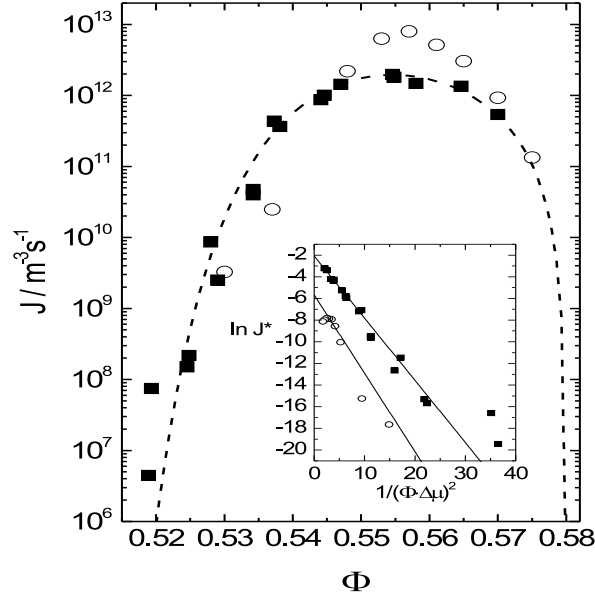
Figure 1.3: Measured crystal nucleation rates I as of function of volume fraction ϕ in a system of hard-sphere colloids. The data are taken from Ref. [3] (open circles) and Ref. [4] (filled cubes). The lines result from a two parameter fit of Eq. (1.4) to the experimental data. The inset shows the dimensionless nucleation rate densities plotted logarithmically versus $1/(\phi\Delta\mu)^2$. The figure is taken from Ref. [5].

low [6]. In addition, the values of the effective jump length λ seem rather extreme. However, as the experimental results could be fitted with Eq. (1.4), there was little reason to doubt the values of the fit parameters thus obtained from experiment. As the crystal nucleation rate is a difficult quantity to measure there is a clear need for a first principle prediction of a crystal nucleation rate.

In this thesis we approach this problem by using a combination of numerical techniques to simulate the crystal nucleation process. We use umbrella sampling, in combination with local bond-order analysis for the identification of crystal nuclei, to compute the shape and height of the nucleation barrier and to study the structure of critical nuclei. Our barrier calculations in combination with a precise knowledge of the difference in chemical potential between the two phases enable us to deduce the surface free energy for the critical nucleus. This allows us to detect any dependence of the surface free energy on supersaturation. In addition we perform kinetic Monte Carlo simulations to compute the actual nucleation rate. The result can be compared directly with experiments without any adjustable parameter.

1.2 Overview

This thesis is devoted to the numerical study of crystallization in a suspension of spherical colloids. It is divided into two parts. The first part contains a brief review of the relevant theoretical background and a description of the methods used. In the second part we apply these techniques to several model colloids.

In chapter 2 we give a summary of the general formulation of the theory of rare events in the framework of linear response theory. Our aim is to illustrate how molecular simulations

can be used to compute the rate of activated processes. At the end of this chapter we apply this formulation to the special case of diffusive barrier crossing, which is appropriate for crystal nucleation. We continue in chapter 3 with a detailed discussion of classical nucleation theory, which is widely used to analyse crystallization rates, both in experiments and in computer simulations. We also make the connection between the results for the nucleation rate from chapter 2. In chapter 4 we give a practical introduction to the numerical techniques needed for a quantitative prediction of a nucleation rate.

In the second part, we first study the crystallization kinetics in hard-sphere colloids (chapter 5). As crystallization of hard-sphere colloids has been extensively studied experimentally this system was an obvious choice. To our knowledge, this work constitutes the first example where computer simulations of crystal nucleation rates are compared quantitatively with experiment. Furthermore a comparison with CNT is made. Secondly, we study the effect of polydispersity on the crystallization kinetics, again in a system of hard-sphere colloids (chapter 6). This project was mainly driven by the experimental observation that polydispersity suppresses crystal nucleation. These simulations shed a new and rather surprising light on this subject. The third project (chapter 7) was motivated by the experimental observation that charged colloidal spheres seem to crystallize much faster than hard-spheres. In addition, there were observations of the formation of crystal nuclei with a body centered cubic structure in a region of the phase diagram where a close packed structure is stable. Based on our simulation results, we can give explanations for both observations. Chapter 8 is an extension of the previous project. We study the effect of a slight softness on the phase behavior and the crystallization kinetics compared to hard-spheres. The motivation for this project arises from the fact that experimental hard-sphere colloids are actually slightly soft. At present, there is little a priori knowledge of the effect of this softness on crystal nucleation. Here again our simulation results can be directly compared to the experiments. We end part two with chapter 9 where we apply our techniques to a heterogeneous system. We study how the presence of a flat hard wall influences the crystallization barrier in a hard-sphere system. This constitutes an example of a free energy calculation for a heterogeneous nucleation process.

Part I

Theoretical and technical introduction

2

Rare events

In this chapter we illustrate how molecular simulations can be used for the calculation of a reaction rate constant, where the rate limiting step is a classical barrier crossing. Examples are the trans-to-gauche transition in an alkane or ion pair dissociation. This is done in the framework of linear response theory, where we follow the book of Frenkel and Smit [7]. Here, however we will not give the detailed derivation of the final results, but focus more on the general concept and their practical application. This background is needed to place the work presented in a broader content. Finally, we derive an expression for the rate constant for the special case where the barrier crossing is diffusive. The result will be applied to the calculation of a crystallization rate.

2.1 Phenomenological rate equation

Consider a unimolecular reaction $A \rightleftharpoons B$, in which species A is transformed to species B. Let us assume that the rate limiting step of the reaction is a classical barrier crossing. We first look at the phenomenological description of this process. We assume that the reaction can be described by a first order rate equation, where c_A and c_B are the number density of molecules in state A and B:

$$\frac{dc_A(t)}{dt} = -k_{AB}c_A(t) + k_{BA}c_B(t) \tag{2.1}$$

$$\frac{dc_B(t)}{dt} = +k_{AB}c_A(t) - k_{BA}c_B(t). \tag{2.2}$$

Here k_{AB} and k_{BA} are the rate constants of the reaction and we assume that the total number density is conserved

$$\frac{d[c_A(t) + c_B(t)]}{dt} = 0. \tag{2.3}$$

In equilibrium the concentrations of molecules in states A and B are time independent, $\dot{c}_A = \dot{c}_B = 0$, and the solution of the rate equation is stationary:

$$\frac{k_{AB}}{k_{BA}} = \frac{\langle c_A \rangle}{\langle c_B \rangle}. \tag{2.4}$$

Here the $\langle \rangle$ denote an ensemble average. If we apply a small perturbation to the system, the decay is described by Eq. (2.1):

$$\frac{d\Delta c_A(t)}{dt} = -k_{AB}\Delta c_A(t) + k_{BA}\Delta c_A(t), \tag{2.5}$$

where we have used Eq. (2.3) and Eq. (2.4) and defined $\Delta c_A(t) = c_A(t) - \langle c_A \rangle$. The solution is :

$$\Delta c_A(t) = \Delta c_A(0) \exp(-t/\tau), \tag{2.6}$$

where $\tau = (k_{BA} + k_{AB})^{-1}$ is the reaction time constant. Using Eq. (2.4) we can rewrite it as:

$$\tau = \frac{\langle c_B \rangle}{k_{AB}}, \tag{2.7}$$

where we have normalized the total number density $c_A + c_B = 1$. c_A and c_B are therefore the probabilities that a given molecule is in state A or B.

2.2 Microscopic description

In the case of classical barrier crossing the rate constant of the reaction can be computed with molecular simulations. To see this we need to write down a microscopic expression for the rate constant k_{AB}. This is done in the framework of linear response theory. In what follows we present only the essentials of the derivation. For more details see Ref. [7]. First we need a reaction coordinate q, which measures how far the reaction has progressed. In general q can be a complicated function of the coordinates of all particles. As q is increased the system is driven from state A to state B. The free energy $F(q)$ as a function of q first increases, goes through a maximum at q^*, and then starts to decrease. We now apply a small external perturbation to the system which changes the concentration of the molecules in state A (and B equivalently):

$$c_A \to c_A + \Delta c_A. \tag{2.8}$$

This perturbation is achieved by adding a term to the Hamiltonian H_0 of the system, that for example lowers the potential energy for all states with $q < q^*$ relative to those with $q > q^*$:

$$H = H_0 - \lambda g_A(q - q^*). \tag{2.9}$$

Here λ is the strength of the perturbation and g_A is the perturbation function. In the following we assume that the perturbation function $g_A(q - q^*)$ varies smoothly from 1 to 0 in the barrier region, and is 1 in state A and 0 in state B. With this definition the average value of g_A is simply equal to the probability of finding the system in state A and we also note that

$$\Delta c_A = \langle c_A \rangle_\lambda - \langle c_A \rangle = \langle g_A \rangle_\lambda - \langle g_A \rangle, \tag{2.10}$$

where $\langle \rangle_\lambda$ is the ensemble average with the Hamiltonian H in Eq. (2.9). This identification is possible, because by definition c_A and g_A may differ only in the barrier region, where the system does not spend much time. In the limit of a small perturbation $\lambda \to 0$ we can use linear response theory to describe the relaxation process. Onsager's famous regression hypothesis says that the relaxation of the macroscopic system is governed by the same laws as the regression of the spontaneous microscopic fluctuations of the system. If we switch off a perturbation g_A at time $t = 0$ the concentration c_A will relax to its equilibrium value as follows:

$$\frac{\Delta c_A(t)}{\Delta c_A(0)} = \frac{\langle \Delta g_A(0) \Delta c_A(t) \rangle}{\langle \Delta g_A(0) \Delta c_A(0) \rangle} = \frac{\langle \Delta g_A(0) \Delta g_A(t) \rangle}{\langle \Delta g_A(0) \Delta g_A(0) \rangle}, \tag{2.11}$$

where we have used Eq. (2.10). The basic idea of finding a microscopic expression for the rate constant k_{AB} is based on the identification of Eq. (2.11) with Eq. (2.6). However one needs to be careful, as for very short times (such as the average time that the system spends in the barrier

region), one should not expect the auto-correlation function to relax exponentially. Only at times that are long compared to typical barrier-crossing times this should be correct. For times t much larger compared to molecular times but still much shorter than the regression time τ, the reaction rate is given by

$$k_{AB} = \frac{\langle \dot{q}(0)\partial_q g_B(0)g_B(t)\rangle}{\langle c_A \rangle}, \tag{2.12}$$

where we have defined a function $g_B = 1 - g_A$. Here the right side of the equation explicitly depends on time, whereas k_{AB} does not. Therefore the above expression is only valid after a transient time, where the system relaxes to its steady state and reaches a plateau value. The expression above is general for the calculation of rate constant. It is still necessary to rewrite it in a form that is convenient for a numerical calculation. In particular the choice of the perturbation function g_A turns out to be important for the efficiency of the numerical calculation. In the following we show the well-known Bennett-Chandler expression for the rate and a revised version of it that is particularly efficient for diffusive barrier crossing. It should be stressed that, apart from computational efficiency, both expressions yield identical results. The expressions differ only in the choice of g_A.

2.3   Bennett-Chandler approach

If we use for the perturbation function $g_A = \Theta(q - q^*)$ the Heaviside function, we get the Bennett-Chandler expression for the rate [8]:

$$k_{AB} = \frac{\langle \dot{q}(0)\delta(q(0) - q^*)\Theta(q - q^*)\rangle}{\langle \Theta(q^* - q)\rangle}. \tag{2.13}$$

In practice it is more convenient to write the rate in a slightly different form. We multiply Eq. (2.13) by $\langle \delta(q - q^*)\rangle / \langle \delta(q - q^*)\rangle$ to get:

$$k_{AB} = \frac{\langle \dot{q}(0)\delta(q(0) - q^*)\Theta(q - q^*)\rangle}{\langle \delta(q^* - q)\rangle} \times \frac{\langle \delta(q^* - q)\rangle}{\Theta(q - q^*)}. \tag{2.14}$$

The first term on the right hand side describes the average flux over the top of the barrier. In a molecular simulation one needs to compute the product of the derivative of the generalized velocity $\dot{q}$ at $t = 0$, multiplied by the probability that the system is at point q^* at time $t = 0$, and this is then multiplied by one if the system ends up in state B or zero otherwise. As the barrier is usually much higher than the thermal energy $k_B T$, it is not possible to get an good estimate for the average flux using a conventional molecular simulation, since the statistics would be very poor. Rather one has to use constrained dynamics or a biased Monte Carlo scheme to generate a sequence of configurations at the transition state.

In the present thesis, we use biased Monte Carlo sampling to generate an ensemble at the top of the barrier. The implementation of this biasing scheme is straightforward and will be shown later in section 4.1.4.

The second term on the right hand side of Eq. (2.14) is the probability density of finding the system at the top of the barrier divided by the probability of finding the system in state A:

$$\frac{\langle \delta(q^* - q)\rangle}{\Theta(q - q^*)} = \frac{\exp(-\beta F(q^*))}{\int_0^{q^*} dq \exp(-\beta F(q))}, \tag{2.15}$$

where $\beta = 1/k_B T$. This is an equilibrium quantity that can be computed with a Monte Carlo simulation. However as the probability is very small one needs to use biased sampling.

2.4 Diffusive barrier crossing

The Bennett-Chandler expression for the rate constant for classical barrier crossing is widely used in numerical simulations. However it becomes inefficient for diffusive barrier crossing. The reason is that it prepares the system far from the steady state and the relaxation process for diffusive barrier crossing can be very slow. Furthermore, it uses the noisy Θ−function to detect whether the system is in state A or B. The result is a poor statistical accuracy. In an improved version of this scheme [9] Ruiz-Montero et al. used a perturbation function which prepares the system closer to the steady state and also replaces the detector function by a much smoother function. The expression for the rate constant then has the following form [9]:

$$k_{AB} = \int_0^\infty dt \langle \dot{q}(0)\dot{q}(t) \exp[\beta\{F(q(t)) - F(q(0))\}]\rangle_P \frac{N'\langle P\rangle}{N^2 \langle c_A\rangle} \quad \text{with} \quad (2.16)$$

$$N = \int_{q_A}^{q_B} dq \exp(\beta F(q)) \qquad \text{and}$$

$$N' = \int_{q_A}^{q_B} dq \exp(2\beta F(q)) \qquad \text{and}$$

$$P(q) = \frac{\exp(2\beta F(q))}{N'}.$$

Here q_A and q_B are the values of the reaction coordinate in states A and B. The index $\langle ...\rangle_P$ indicates, that the ensemble average is biased by the distribution function $\exp(2\beta F(q))$. The function $2\beta F(q)$ acts as a biasing potential which forces the system to sample at the top of the barrier. The term $\langle ...\rangle_P$ is a kinetic factor which can be computed in a molecular dynamics simulation. If we compare this factor with Eq. (2.14), we see that the starting points of the trajectories are no longer exactly constrained to the top of barrier. They are generated by the distribution that is proportional to $\exp(-\beta F(q)) \times \exp(2\beta F(q)) = \exp(\beta F(q))$.

The calculation of the rate constant is then again split into two parts. First one computes the static term $N'\langle P\rangle/N^2\langle c_A\rangle$. The static term can be computed in a biased Monte Carlo simulation. The average $\langle P\rangle$ is proportional to the probability density of finding the system at the top of the barrier. The quantities $\langle P\rangle$, N and N' can all be computed once $F(q)$ has been chosen. Then the kinetic term can be computed in a molecular dynamics simulation. In practice it may be convenient to generate an ensemble of configurations at the top of the barrier using a biased Monte Carlo simulation. Each configuration is then the starting point of a molecular dynamics trajectory and one measures the reaction coordinate q as a function of time.

It should be stressed that the above expression is valid for any choice of $F(q)$. Even if we have only a rough estimate of the free energy barrier the rate constant can be computed. It is also not necessary that the barrier crossing be truly diffusive. Note also that the function $\exp[\beta\{F(q(t)) - F(q(0))\}]$ decreases rapidly once the system moves out of the barrier region. This means that the main contribution to the average will come from trajectories close to the top of the barrier. If we approximate the top of the barrier by a parabolic function, and if the mean free path is much shorter than the width of the barrier, than Eq. (2.16) reduces to the diffusive limit:

$$k_{AB} \approx D \sqrt{\frac{|F''|}{2\pi kT}} \frac{\rho_{eq}(q^*)}{\langle c_A\rangle}, \qquad (2.20)$$

where the diffusion constant D is defined by the Green-Kubo relation:

$$D \equiv \int_0^\infty dt \langle \dot{q}(0)\dot{q}(t)\rangle. \qquad (2.21)$$

Moreover we used the fact that $\langle P \rangle = (1/\sqrt{2})\rho_{eq}(q^*)$, where $\rho_{eq}(q^*) = \rho_A \exp(-\beta F(q^*))$ is the equilibrium density at the top of the barrier, and ρ_A is the number density of state A.

In nucleation it is necessary to think of c_A as the probability that the system is in state A. Note that the diffusion coefficient results from the correlation function of the reaction coordinate and therefore in nucleation, where our reaction coordinate is the size of a cluster, it is related to the attachment rate of particles to the critical cluster. The above expression is then identical with the expression for the steady state nucleation rate from the classical theory of nucleation, which we will derive in section 3.1.

3

Classical theory: Steady-state nucleation

In this chapter we first discuss classical nucleation theory (CNT): the simplest and most widely used theory that describes a nucleation process. The present form was developed in the first half of the 20th century. As early as the end of the 19th century, J. W. Gibbs [10,11] showed that, due to the work required to form an interface between the new phase and its parent phase, a nucleus of the new phase can only grow after it reaches a critical size. In the 1920's Volmer and Weber [12] initiated a kinetic theory for the formation of a nucleus. This theory was further developed by Faruas [13] and subsequently by Becker and Döring [14], Zeldovich [15] and Frenkel [16]. In our discussion of CNT we follow Kelton [17]. We extend the thermodynamic expression for the nucleation barrier to a multicomponent system and discuss the thermodynamics of curved interfaces.

3.1 Kinetics

Consider a liquid with a given distribution N_n of clusters, where N_n is the number of clusters of size n. We are interested in the change in cluster size distribution due to an abrupt change of the pressure or density of the liquid. The transient behavior can be described by a set of coupled rate equations for the number densities of the clusters. However, in order to do this one has to make a couple of assumptions. We assume that the mechanisms by which a cluster can grow or shrink are the attachment and detachment of single molecules. This assumes that we have a method to identify a cluster and to assign a size to it. Furthermore, events where pre-existing clusters collide and fuse, or where a cluster splits into two or more smaller cluster are ignored. In addition we assume that the events by which a cluster gains or loses particles are not correlated, or in other words, that there are no correlations between successive events. The rate equations for the time-dependent cluster density N_n then have the following form:

$$\frac{dN_n}{dt} = f_{n-1}^+ N_{n-1}(t) - b_n^- N_n(t) - f_n^+ N_n(t) + b_{n+1}^- N_{n+1}(t), \tag{3.1}$$

where f_n^+ is the forward rate for the attachment of particles to a cluster of size n and b_n^- the corresponding backward rate. We can define a flux $k_n(t)$ or net rate at which clusters of size n become clusters of size $n + 1$:

$$k_n(t) = f_n^+ N_n(t) - b_{n+1}^- N_{n+1}(t). \tag{3.2}$$

In the steady state the flux is constant and equal for all sizes:

$$k = f_n^+ N_n(t) - b_{n+1}^- N_{n+1}(t) = f_{n+1}^+ N_{n+1}(t) - b_{n+2}^- N_{n+2}(t) = \dots \tag{3.3}$$

In the following we want to solve this equation. After the abrupt change it is generally assumed that after a transient time τ, during which the cluster size distribution changes, a steady state is reached in which there is a continuous flux of monomers to larger cluster sizes. However the cluster size distribution does not change any more and $N_n(t)$ is time independent. The liquid is, due to the very small steady state flux, in a kind of quasi equilibrium, where for small cluster sizes $n \ll n_{crit}$, where n_{crit} is the critical cluster size, the steady state cluster size distribution is almost equal to the equilibrium Boltzmann distribution: $N_n^{ss} \approx N_n^{eq}$. However for large cluster sizes $n \gg n_{crit}$ the steady state cluster size distribution $N_n^{ss} \to 0$ vanishes while the corresponding Boltzmann distribution starts to increase and is much larger: $N_n^{ss} \gg N_n^{eq}$. Making use of the fact that there is no net flux in equilibrium: $f_n^+ N_n^{eq} - b_{n+1} N_{n+1}^{eq} = 0$ or $b_n^- = f_n^+ N_n^{eq}/N_{n+1}^{eq}$ we can eliminate the backward rate from Eq. (3.1):

$$k = f_n^+ N_n^{eq} \left(\frac{N_n}{N_n^{eq}} - \frac{N_{n+1}}{N_{n+1}^{eq}} \right). \tag{3.4}$$

Dividing Eq. (3.4) by $f_n^+ N_n^{eq}$ and summing both sides over cluster sizes from $L \ll n_{crit}$ to $H \gg n_{crit}$ yields:

$$k \sum_{n=L}^{H} \frac{1}{f_n^+ N_n^{eq}} = \sum_{n=L}^{H} \left(\frac{N_n}{N_n^{eq}} - \frac{N_{n+1}}{N_{n+1}^{eq}} \right) = \frac{N_L}{N_L^{eq}} - \frac{N_{H+1}}{N_{H+1}^{eq}}, \tag{3.5}$$

as all intermediate terms on the right side cancel each other. If we make now use of the fact that for $L \ll n_{crit}$: $N_L^{ss} \approx N_L^{eq}$ and for $H \gg n_{crit}$: $N_{H+1}^{ss}/N_{H+1}^{eq} \to 0$ we get

$$k \sum_{n=L}^{H} \frac{1}{f_n^+ N_n^{eq}} = 1. \tag{3.6}$$

It is reasonable to assume that the sum is dominated by cluster sizes close to the top of the nucleation barrier, as there $1/N_n^{eq}$ has its maximum. We therefore Taylor expand the nucleation barrier around its maximum up to quadratic order. Furthermore we assume that the attachment rates near the maximum are constant $f_n^+ \approx f_{n_{crit}}^+$. If we extend the summation over $\Delta n = n - n_{crit}$ from $-\infty$ to $+\infty$ and replace it by an integral we find the final form of the steady state nucleation rate:

$$k = Z f_{n_{crit}}^+ N_1 \exp(-\Delta G(n_{crit})/k_B T), \tag{3.7}$$

where $Z = \sqrt{|\Delta G(n_{crit})''|/2\pi k_B T}$ is the Zeldovich factor. Here we have already made use of the fact that the equilibrium cluster size distribution at the top of the nucleation barrier is given by the Boltzmann factor: $N_{n_{crit}}^{eq} = N_1 \exp(-\Delta G(n_{crit})/k_B T)$. The only difference in the steady state nucleation rate compared to the solution one gets if the back flux is set to zero and the N_n are set to the equilibrium distribution, is the Zeldovich factor.

The steady state nucleation rate can therefore be interpreted as the product of the probability that a critical nuclei is formed: $P(n_{crit}) = \exp(-\Delta G(n_{crit})/k_B T)$, times the number of monomers, times the rate with which a critical nuclei grows, times the Zeldovich factor, which takes care of the fact that not all particles at the top of the nucleation barrier end up in the solid phase, but can also recross and dissolve again.

We can also make a simple estimate for the attachment rate of particles to the critical cluster. To this end we multiply the number of monomers available at the surface of the nuclei, which is proportional to $n_{crit}^{2/3}$, with a typical transition rate of these particles to become part of the nucleus. This transition rate is proportional to D_S/λ^2, where D_S is a self-diffusion coefficient and

λ a typical distance over which the diffusion takes place - of the order of the particle diameter. The attachment rate of particles to the critical cluster is then given by:

$$f^+_{n_{\text{crit}}} = \frac{24 D_S n_{\text{crit}}^{2/3}}{\lambda^2}. \tag{3.8}$$

3.2   Nucleation barrier

Let us consider two systems. System (I) contains the homogeneous, metastable phase β. System (II) contains the parent phase β with a nucleus of phase α. The height of the nucleation barrier can be computed in several ways, depending on the thermodynamic variables that we keep fixed. For instance, for a system with fixed number of particles N at constant pressure p and temperature T, the nucleation barrier is given by the difference in Gibbs free energy between the states II and I. In order to compute this barrier we first evaluate the difference in the internal energy

$$\Delta U = U^{\text{II}} - U^{\text{I}}. \tag{3.9}$$

The internal energy of system I is given by

$$U^{\text{I}} = T^{\text{I}} S^{\text{I}} - p^{\text{I}} V^{\text{I}} + \mu^{\text{I}} N, \tag{3.10}$$

where S is the entropy, V^{I} the volume and μ^{I} the chemical potential of system I. As state II is also in equilibrium, albeit it an unstable one, the chemical potential is constant throughout the system - even though the system itself is inhomogeneous. The internal energy of system II is given by

$$
\begin{aligned}
U^{\text{II}} &= T^{\text{II}} S^{\text{II}} - p^{\text{II}}_\alpha V^{\text{II}}_\alpha - p^{\text{II}}_\beta V^{\text{II}}_\beta + \gamma A + \mu^{\text{II}} N \\
&= T^{\text{II}} S^{\text{II}} + (p^{\text{II}}_\beta - p^{\text{II}}_\alpha) V^{\text{II}}_\alpha - p^{\text{II}}_\beta V^{\text{II}} + \gamma A + \mu^{\text{II}} N
\end{aligned} \tag{3.11}
$$

We consider the situation that the nucleus is formed at constant pressure and temperature. In that case $p^{\text{I}} = p^{\text{II}}_\beta = p, T^{\text{I}} = T^{\text{II}} = T$ and $\mu^{\text{I}} = \mu^{\text{II}} = \mu$. The last equality follows because the chemical potential in the parent phase is a function of p and T only. The difference in the internal energies of systems I and II is then given by

$$\Delta U = T\Delta S + (p - p^{\text{II}}_\alpha) V^{\text{II}}_\alpha + \gamma A - p\Delta V, \tag{3.12}$$

where $\Delta S = S^{\text{II}} - S^{\text{I}}$ and $\Delta V = V^{\text{II}} - V^{\text{I}}$. Note that the terms involving the chemical potentials drop out of the expression for ΔU. The expression for the nucleation barrier then becomes

$$
\begin{aligned}
\Delta G &= \Delta U + p\Delta V - T\Delta S \\
&= (p - p^{\text{II}}_\alpha) V^{\text{II}}_\alpha + \gamma A.
\end{aligned} \tag{3.13}
$$

 This equation holds for every dividing surface. Moreover we did not make any approximations concerning the compressibility of either phase, nor concerning the interfacial free energy. If we choose the surface of tension to be the dividing surface (see appendix 3.3), then we can use the Laplace equation ($\Delta p = 2\gamma_S / R_S$) to express the height of the barrier as

$$
\begin{aligned}
\Delta G &= \frac{4}{3}\pi R_S^2 \gamma_S \\
&= \frac{2}{3}\pi \Delta p R_S^3.
\end{aligned} \tag{3.14}
$$
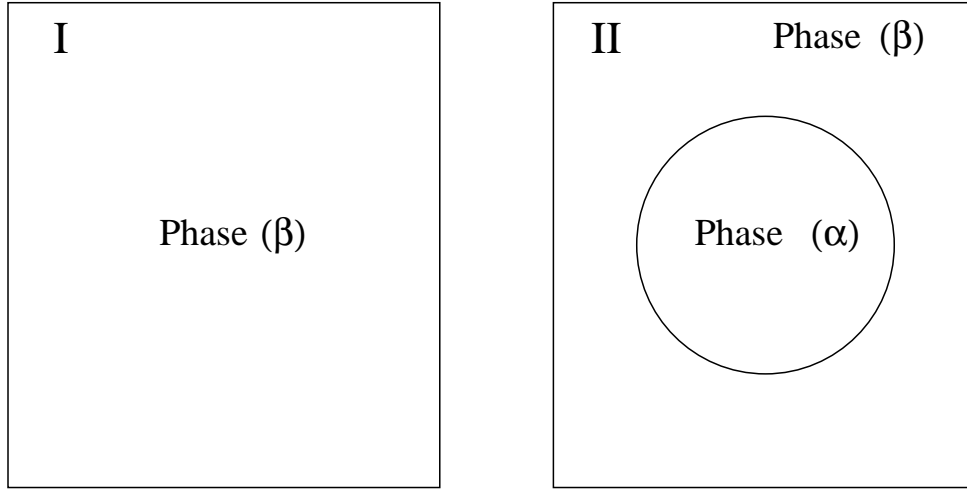
Figure 3.1: Formations of a nucleus of a stable phase α in a metastable phase β. The nucleation barrier is given by the free energy difference of the two systems.

In what follows it will be convenient to express the surface tension γ_S in terms of the barrier height ΔG and the Laplace pressure Δp

$$\gamma_S = \left(\frac{3}{16\pi}\right)^{1/3} \Delta G^{1/3} \Delta p^{2/3}. \tag{3.15}$$

In the following chapters we will use this equation to calculate the surface tension from the measured barrier height and the Laplace pressure.

In order to derive the expression from CNT for the barrier height, we continue with equation Eq. (3.13). If we make use of the Gibbs-Duhem relation for a isothermal variation of the pressure in system II and assume in addition that the fluid is incompressible ($\rho_\alpha = \rho_\beta$) we get

$$\mu_\alpha^{II}(p_\alpha^{II}) - \mu_\alpha^{II}(p_\beta^{II}) = \frac{p_\alpha^{II} - p_\beta^{II}}{\rho_\alpha}. \tag{3.16}$$

Using this relation Eq. (3.13) becomes

$$\Delta G = [\mu_\alpha^{II}(p_\alpha^{II}) - \mu_\alpha^{II}(p_\beta^{II})]N_\alpha + \gamma A, \tag{3.17}$$

where N_α is the number of particles in the parent phase α. As the chemical potentials of the parent phase and the nucleus are the same $\mu_\alpha^{II}(p_\alpha^{II}) = \mu_\beta^{II}(p_\beta^{II})$, we retrieve the CNT expression the nucleation barrier

$$\Delta G = \Delta\mu N_\alpha + \gamma A, \tag{3.18}$$

where $\Delta\mu = \mu_\alpha^{II}(p_\beta^{II}) - \mu_\beta^{II}(p_\beta^{II})$ is the difference in chemical potential between the two phases at pressure p_β. Assuming that the nucleus is spherical $A = 4\pi R^2$, the barrier height is given by

$$\Delta G^* = \frac{16\pi}{3} \frac{\gamma^3}{\rho_\alpha \Delta\mu^2} \tag{3.19}$$

while the critical radius is

$$R^* = \frac{2\gamma}{\rho_\alpha \Delta\mu}, \tag{3.20}$$

see also Fig. 1.1.

3.2.1 Multicomponent system

It is straightforward to generalize the expression for the nucleation barrier from CNT to a multi-component system. The internal energies U^I and U^{II} are given by Eqs. (3.10),(3.11), but we have to replace the term of the chemical potential by a sum over all species $\sum_{i=1}^{n} \mu_i N_i$. We should note that the general expression for the barrier height Eq. (3.13) is the same for a multicomponent system, as all terms including the chemical potentials drop out. We stress that for every component the chemical potentials in the parent phase and in the critical nuclei are the same $\mu_i^I = \mu_i^{II} = \mu_i$. In the absence of the Laplace pressure, the chemical potentials in phase α would be lower than those in phase β. The effect of the Laplace pressure is to compensate this difference for every component i. At the first sight, it would seem that the computation of Δp is an intractable problem for a multicomponent system - to satisfy the condition that $\mu_i^\alpha = \mu_i^\beta$ for all i it is not enough to compress phase α; we should also change its composition. The situation is greatly simplified if we make use of the semi-grand canonical ensemble. In this ensemble, the independent variables that describe the state of an n-component system are the temperature T, the pressure p, the total number of particles N and the set of $n-1$ differences in the chemical potential $\Delta \mu_i$ between a reference species, say $i = 1$ and all other species $i \neq 1$. The number of components n can be infinite. At coexistence the chemical potentials of all species i in the two phases are equal $\mu_i^\beta = \mu_i^\alpha$. This means in the semi-grand ensemble that the temperature and pressure as well as the reference chemical potential μ_1 and all the $\Delta \mu_i$ are equal. Now we consider what happens if we supersaturate the parent phase by compression. In the semi-grand ensemble we perform this by increasing p, while keeping T and all $\Delta \mu_i$ constant. Note that this does not correspond to the experimental route for supersaturation as there the composition of the system cannot change. In this case all $\Delta \mu_i$ change by different amounts, and it is precisely this factor that complicates the analysis in multicomponent systems. Suppose that we have compressed the system up to a pressure p_β, where μ_1 and all μ_i increased by an amount $\Delta \mu^\beta$. An equal compression of phase α leads to an increase $\Delta \mu^\alpha$ for all species. Obviously $\Delta \mu^\alpha$ is less than $\Delta \mu^\beta$ because beyond coexistence phase β is metastable. However we can compress phase α to a higher pressure p_α such that

$$\Delta \mu^\alpha(p_\alpha) = \Delta \mu^\beta(p_\beta). \tag{3.21}$$

Thus, working in the semi-grand ensemble we have achieved equality of the chemical potentials of all species in the multicomponent mixture. In homogeneous nucleation it is the Laplace pressure that ensures that the chemical potentials of all species are equal and we can make the following identification

$$\Delta p = p_\alpha - p_\beta. \tag{3.22}$$

Note also that only after we have determined the pressure p_α, the density and the composition of phase α can be measured. To solve Eq. (3.21) we can use the following thermodynamic relation

$$\frac{\partial \mu_1}{\partial p} = \frac{V}{p}, \tag{3.23}$$

which is just the combination of the Gibbs-Duhem relation and the change of the Gibbs free energy for isothermal compression. We can then write Eq. (3.21) as

$$\int_{p_{coex}}^{p_\beta + \Delta p} \langle V(p) \rangle_\alpha dp = \int_{p_{coex}}^{p_\beta} \langle V(p) \rangle_\beta dp \qquad \text{or} \tag{3.24}$$

$$\int_{p_{coex}}^{p_\beta + \Delta p} \langle V(p) \rangle_\alpha dp = \Delta \mu^\beta(p_\beta) \tag{3.25}$$

In practice to determine the Laplace pressure one measures in a semi-grand simulation the average volume V as a function of pressure in both phases. Integrating the average volume over the pressure from coexistence p_{coex} to p_β yields the chemical potential differences in both phases $\Delta\mu_\beta$ and $\Delta\mu_\alpha$. Using Eq. (3.25) one can determine the Laplace pressure by continuing the integration over phase α until the chemical potential difference is equal to that of phase β. The procedure in a one component system is the same, one only uses the $NpT-$ ensemble.

3.3 Appendix: Surface tension of a curved surface

3.3.1 General definition of a surface tension

Let us consider a system with two phases β and α at coexistence. The two phase equilibrium is characterized by equality of temperature $T_\alpha = T_\beta$, pressure $p_\alpha = p_\beta$ and chemical potential $\mu_\alpha = \mu_\beta$ in the bulk phases. However, the density profile in the interface region varies continuously between the bulk densities of the two phases. This density variation gives rise to an extra contribution in the thermodynamic functions, which need to include the work γA to create the surface area A, where γ is the surface tension. If we assume that this system has a fixed number of particles N, at constant volume V and temperature T, the Helmholtz free energy is given by

$$F = -ST - pV + \gamma A + \mu N, \tag{3.26}$$

where S is the entropy and μ the chemical potential of the system. The thermodynamic definition of the surface tension is then given by

$$\gamma = \left(\frac{\partial F}{\partial A}\right)_{N,V,T}. \tag{3.27}$$

Following Gibbs we now introduce a dividing surface of zero width in the interface region, which establishes a boundary between the two bulk phases. The position of the dividing surface is usually located in the transition zone and the volumes of the two phases are fixed $V = V_\alpha + V_\beta$. The idea of Gibbs was that any extensive thermodynamic quantity can be written as a sum of bulk contributions and a contribution which is assigned to the dividing surface. Examples are the total number of particles in the system $N = N_\alpha + N_\beta + N^S$ or the Helmholtz free energy $F = F_\alpha + F_\beta + F^S$. Here the index S indicates the contribution from the dividing surface. For a planar interface the surface tension does not depend on the location of the dividing surface, as the surface area does not change. For a spherical interface, as we will have in nucleation, this is not the case. The position of the dividing surface determines not only the volume of the two bulk phases, but also the interfacial area.

3.3.2 Curved surfaces

Let us consider a spherical nucleus inside a fixed volume V, containing N particles at temperature T, see Fig. 3.2. We choose a spherical dividing surface with radius R and the corresponding volumes of phases α and β are

$$V_\alpha = \frac{4\pi}{3}R^3, \qquad\qquad V_\beta = V - \frac{4\pi}{3}R^3. \tag{3.28}$$

The Helmholtz free energy of this system is

$$F = -ST - p_\alpha V_\alpha - p_\beta V_\beta + 4\pi R^2 \gamma + \mu N, \tag{3.29}$$
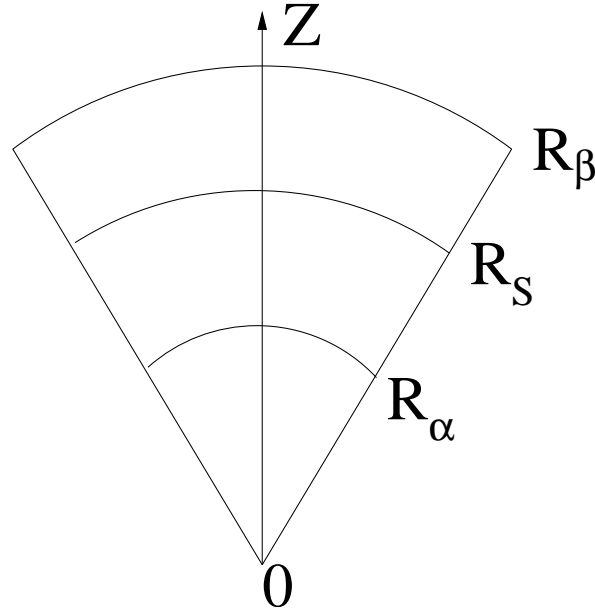
Figure 3.2: Sketch of a spherical interface. For radii $R < R_\alpha$ or $R > R_\beta$ the densities are those of the corresponding bulk phases. Radii $R_\alpha < R < R_\beta$ constitute the transient region. In this area we define a dividing surface R_s, which corresponds to the surface of tension.

where p_α and p_β are the pressures in the two bulk phases and $4\pi R^2 \gamma$ is the surface energy for a given dividing surface. Note that the definition of a dividing surface does not affect the physical parameters in the system, e.g. $F, p_\alpha, p_\beta, \mu, N$. Therefore for a small (mathematical) displacement of the dividing surface we get from Eq. (3.29)

$$[dF] = -\Delta p 4\pi R^2 [dR] + 8\pi R \gamma [dR] + 4\pi R^2 [d\gamma], \tag{3.30}$$

where we defined the Laplace pressure $\Delta p = p_\alpha - p_\beta$. We denote by the differential in square brackets a mathematical displacement of the dividing surface. Differentiation with respect to R leads us to the generalized Laplace equation

$$\Delta p = \frac{2\gamma}{R} + \left[\frac{d\gamma}{dR}\right]. \tag{3.31}$$

The Laplace equation relates the pressure difference between the two phases to the surface tension. The pressure difference arises to ensure equality of the chemical potentials. If the two phases are in equilibrium, be it stable or metastable, the pressure in the droplet of phase α is higher than that of phase β. If we choose the dividing surface such that

$$\left[\frac{d\gamma}{dR}\right]_{R=R_s} = 0, \tag{3.32}$$

then Eq. (3.31) reduces to the standard Laplace equation

$$\Delta p = \frac{2\gamma_s}{R_s}, \tag{3.33}$$

where $\gamma_s = \gamma[R_s]$ is called the surface of tension. We can now easily obtain the complete dependence of γ on R. Therefore we write the generalized Laplace equation Eq. (3.31) in a slightly
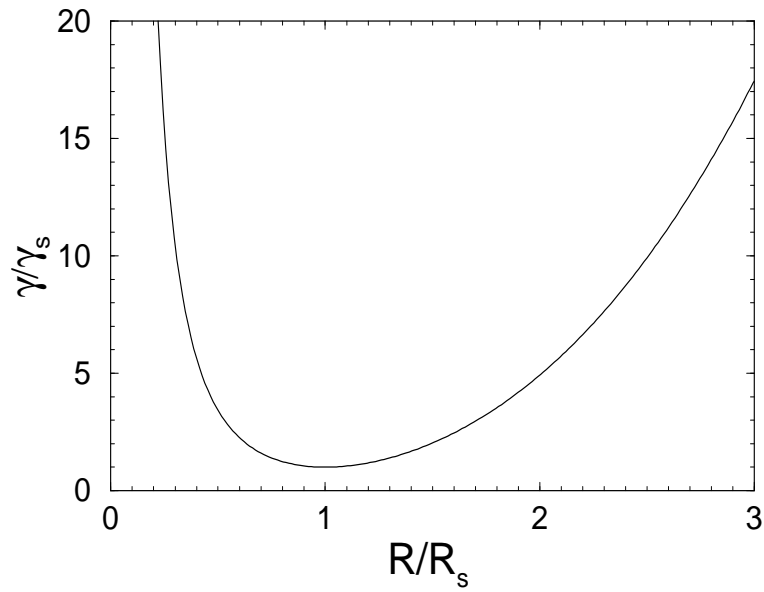
Figure 3.3: Dependence of the surface tension on the radius of the dividing surface Eq. (3.36). The surface tension has a minimum at the surface of tension.

different form

$$\Delta p R^2 = \left[\frac{d}{dR} \right] R^2 \gamma. \tag{3.34}$$

Integration over R from R_s to an arbitrary R gives

$$\gamma(R) = \left(\frac{R_s}{R} \right)^2 \gamma_s + \frac{\Delta p}{3} \left(\frac{R^3}{R_s^2} - R_s \right). \tag{3.35}$$

Using Eq. (3.33) we arrive at

$$\gamma(R) = \gamma_s \left\{ \left(\frac{R_s}{R} \right)^2 + \frac{2}{3} \left[\left(\frac{R}{R_s} \right)^3 - 1 \right] \right\}. \tag{3.36}$$

From Fig 3.3 we see that the surface of tension is at the minimum. The surface tension at any other position in the interface region will be higher.

4

Quantitative prediction of a nucleation rate: A computational approach

The aim of this chapter is to illustrate in some detail how a nucleation rate can be calculated numerically. From Eq. (2.20) or Eq. (3.7) we know that the nucleation rate has the following form:

$$I = \kappa \exp[-\Delta G(n_{crit})/k_B T], \tag{4.1}$$

where κ is the kinetic factor and $\Delta G(n_{crit})$ is the free energy needed for the formation of a critical cluster. The calculation of the nucleation rate is split into two parts. First we compute the nucleation barrier and second we compute the kinetic factor. In the following we discuss the procedure step-by-step using the hard sphere system as an example. We start with the calculation of the nucleation barrier, and then move onto the kinetic factor.

4.1 Calculation of the nucleation barrier

In order to compute the free energy barrier that separates the liquid from the solid state, we need to choose a reaction coordinate that connects the two phases. It has been shown that it is better to use a global rather than a local reaction coordinate and we use the cluster size [18, 19]. We can then use the theory of thermodynamic fluctuations [20], which relates the probability $P(n)$ for the formation of a cluster of size n to the corresponding Gibbs free energy:

$$G(n) = \text{constant} - \ln[P(n)]. \tag{4.2}$$

In the following we first derive an expression for the probability distribution function $P(n)$. Next we discuss how clusters can be identified using local bond-order parameters, and finally we show how we compute the equilibrium distribution function in a Monte Carlo simulation.

4.1.1 Distribution of cluster sizes in equilibrium

The distribution can be derived both macroscopically from thermodynamics, and microcopically from statistical mechanics. We describe the two approaches in turn.

Thermodynamic description

We first compute the equilibrium distribution of cluster sizes of phase α in the metastable supersaturated phase β, see Fig. 3.1, using a thermodynamic description. To this end, we assume that

the concentration of clusters is low enough that we can ignore interactions between them. Then we can treat the system as an ideal mixture of clusters consisting of N_1 monomers, N_2 dimers, ..., N_n n-mers, where $N_t = \sum_{i=1}^{\infty} N_i$ is the total number of clusters. Before we can calculate the cluster size distribution, we recall some thermodynamic relations for an ideal mixture. The Gibbs free energy of this system is given by

$$G(P, T) = \sum_{i=1}^{\infty} N_i \mu_i(P, T), \tag{4.3}$$

where $\mu_i(P, T)$ is the chemical potential of a cluster of size i at pressure P and temperature T. We should also note that after mixing, each n-mer exerts a partial pressure p_n, such that $\sum p_n = P$. The chemical potential of a cluster of size n is then given by

$$\mu_n(p_n, T) = \mu_n(P, T) + kT \ln[p_n/P] \tag{4.4}$$
$$= \mu_n(P, T) + kT \ln[N_n/N_t], \tag{4.5}$$

where we used the fact that the ratio of the partial pressure p_n and the pressure P is equal to the ratio N_n/N_t (Raoult's law). Combining Eq. (4.3) with Eq. (4.5) yields

$$G(P, T) = \sum_{n=1}^{\infty} N_n \{\mu_n(P, T) + kT \ln[N_n/N_t]\} \tag{4.6}$$
$$= \sum_{n=1}^{\infty} N_n \mu_n(P, T) + TS_{mix}, \tag{4.7}$$

where $S_{mix} = -k \sum_{n=1}^{\infty} N_n \ln[N_n/N_t]$ is the entropy of mixing the clusters.

We can now calculate the difference in Gibbs free energy between system I, containing N nuclei of size one, and system II, containing one nucleus of size n and $N - n$ nuclei of size one. Using Eq. (4.3) the difference in Gibbs free energy between the two systems is

$$\Delta G(n) = G^{II}(P, T) - G^I(P, T) = \mu_n(P, T) - n\mu_1(P, T). \tag{4.8}$$

We can now obtain the cluster size distribution from the equilibrium condition $\mu_n(p_n, T) = n\mu_1(p_1, T)$. Insertion of Eq. (4.5) in Eq. (4.8) yields

$$\Delta G(n) = kT \ln[N_n/N_t] - kT \ln[(N_1/N_t)^n]. \tag{4.9}$$

The probability for the formation of a nucleus of size n is then just given by

$$\exp[-\Delta G(n)/k_B T] = \frac{N_n N_t^n}{N_t N_1^n} = \frac{N_n}{N_1}, \tag{4.10}$$

where we have used the fact that the number of monomers is almost equal to the total number of nuclei $N_1 \approx N_t$. As the monomers are often in large excess, we can also approximate N_1 by N to get

$$P(n) = \frac{N_n}{N}. \tag{4.11}$$

Statistical mechanical description

We turn now to a statistical mechanical derivation of the cluster size distribution. The derivation is based on Refs. [18,19,21]. The partition function of a system containing N particles in a volume V at temperature T is given by

$$Q(N, V, T) = \frac{1}{\Lambda^{3N} N!} \int d\mathbf{r}^N \exp[-\beta U(\mathbf{r}^N)]. \tag{4.12}$$

Here $U(\mathbf{r}^N)$ is the potential energy of the configuration with coordinates $\mathbf{r}^N$ and $\Lambda = h/\sqrt{2\pi mkT}$ is the thermal de Broglie wavelength. Now we assume that we have a criterion, that enables us to identify a cluster in our system. We then define a function $w_n(\mathbf{r}^n)$ such that

$$w_n(\mathbf{r}^n) = \begin{cases} 1 & \text{If all } n \text{ particles belong to the cluster} \\ 0 & \text{otherwise.} \end{cases} \qquad (4.13)$$

In addition, we define a function $w_{rest}(\mathbf{r}^N) = \prod_{i=n+1}^{N}[1 - w_{n+1}(\mathbf{r}^n, \mathbf{r}_i)]$, which ensures that all other particles do not belong to the cluster

$$w_{rest}(\mathbf{r}^N) = \begin{cases} 1 & \text{if no other particle belongs to the cluster} \\ 0 & \text{if any other particle belongs to the cluster.} \end{cases} \qquad (4.14)$$

We can then define a partition function for a subsystem, that contains at least one n-particle cluster

$$\begin{aligned} Q_n(N, V, T) &= \frac{1}{\Lambda^{3n}n!} \frac{1}{\Lambda^{3(N-n)}(N-n)!} \times \\ &\int d\mathbf{r}^n \int d\mathbf{r}^{N-n} w_n(\mathbf{r}^n) w_{rest}(\mathbf{r}^N) \exp[-\beta U(\mathbf{r}^n, \mathbf{r}^{N-n})], \end{aligned} \qquad (4.15)$$

where we have used the fact that there are $N!/(n!(N-n)!)$ ways to select an n-particle cluster. Note that the remaining particles may still form additional clusters of size n. The product $w_n(\mathbf{r}^n)w_{rest}(\mathbf{r}^{N-n}) = 1$, only if all $\mathbf{r}^n$ particles belong to a cluster and all the other $\mathbf{r}^{N-n}$ do not. We now rewrite the potential energy of the system as the product of contributions, which come from the particles in the cluster $U_n(\mathbf{r}^n)$, times the contribution from all other particles $U_{N-n}(\mathbf{r}^{N-n})$, times the contribution from the interactions between particles in the cluster and the others $U_{n,N-n}(\mathbf{r}^n, \mathbf{r}^{N-n})$. The partition function then becomes

$$\begin{aligned} Q_n(N, V, T) &= \frac{1}{\Lambda^{3n}n!} \frac{1}{\Lambda^{3(N-n)}(N-n)!} \int d\mathbf{r}^{N-n} \exp[-\beta U_{N-n}(\mathbf{r}^{N-n})] \times \\ &\int d\mathbf{r}^n w_n(\mathbf{r}^n) w_{rest}(\mathbf{r}^N) \exp[-\beta U_n(\mathbf{r}^n)] \exp[-\beta U_{n,N-n}(\mathbf{r}^n, \mathbf{r}^{N-n})]. \end{aligned} \qquad (4.16)$$

We can now define effective potentials for all the particles in the cluster

$$U_n' = U_n - kT \ln[w_n], \qquad (4.17)$$

and the interaction between cluster particles and the others

$$U_{n,N-n}' = U_{n,N-n} - kT \ln[w_{rest}], \qquad (4.18)$$

yielding

$$\begin{aligned} Q_n(N, V, T) &= \frac{1}{\Lambda^{3(N-n)}(N-n)!} \frac{1}{\Lambda^{3n}n!} \int d\mathbf{r}^{N-n} \exp[-\beta U_{N-n}(\mathbf{r}^{N-n})] \\ &\int d\mathbf{r}^n \exp[-\beta U_n'] \exp[-\beta U_{n,N-n}']. \end{aligned} \qquad (4.19)$$

Multiplication of the right side by $Q(N-n, V, T)/Q(N-n, V, T)$ gives

$$Q_n(N, V, T) = \frac{1}{n!\Lambda^{3n}} Q(N-n, V, T) \int d\mathbf{r}^n \langle \exp[-\beta U_{n,N-n}'] \rangle \exp[-\beta U_n'], \qquad (4.20)$$

where we have defined a potential of mean force

$$\langle\exp[-\beta U'_{n,N-n}]\rangle = \frac{\int d\mathbf{r}^{N-n}\exp[-\beta U'_{n,N-n}]\exp[-\beta U_{N-n}(\mathbf{r}^{N-n})]}{(N-n)!\Lambda^{3(N-n)}Q(N-n,V,T)}. \tag{4.21}$$

It is the average potential the particles in the cluster feel due to the interactions with all other particles. We define now the partition function of an n-mer as

$$q_n(V,T) = \frac{1}{n!\Lambda^{3n}}\int d\mathbf{r}^n\langle\exp[-\beta U'_{n,N-n}]\rangle\exp[-\beta U'_n]. \tag{4.22}$$

Note that $q_n(V,T,\mu)$ is the partition function of a cluster in which the interaction with the remaining $(N-n)$ molecules is included in the factor $\langle\exp[-\beta U'_{n,N-n}]\rangle$. The interaction with possible other clusters is also included as such clusters can still exist in the remaining $(N-n)$ particles. The partition function Eq. (4.20) can then be written as

$$Q_n(N,V,T) = Q(N-n,V,T)q_n(V,T). \tag{4.23}$$

The probability to find at least one cluster of size n is then given by

$$P_n = \frac{Q_n(N,V,T)}{Q(N,V,T)} = \frac{Q(N-n,V,T)}{Q(N,V,T)}q_n(V,T). \tag{4.24}$$

As the free energy of the system is given by $F = -kT\ln[Q]$, the above equation becomes

$$P_n = q_n(V,T)\exp[-\beta(F(N-n,V,T)-F(N,V,T))]. \tag{4.25}$$

Using

$$F(N-n,V,T) \approx F(N,V,T) - \left(\frac{\partial F}{\partial N}\right)_{V,T}n \tag{4.26}$$

it follows that

$$P_n = q_n(V,T)\exp[+\beta\mu n]. \tag{4.27}$$

The problem with this definition of the probability is that it depends on the volume V. To see this we rewrite Eq. (4.22)

$$q_n(V,T) = \frac{1}{n!\Lambda^{3n}}\int d\mathbf{r}^n\exp[-\beta U_{eff}], \tag{4.28}$$

where we defined an effective potential $U_{eff} = \langle U'_{n,N-n}\rangle + U'_n$. Rewriting the partition function in terms of the center of mass of the cluster yields

$$q_n(V,T) = \frac{n^3}{n!\Lambda^{3n}}\int dR_{CM}\int d\mathbf{r}'^{n-1}\exp[-\beta U_{eff}]. \tag{4.29}$$

Performing the integral over the center of mass and defining a partition function of the cluster in terms of the internal coordinates we get

$$q_n = \frac{V}{\Lambda_n^3}\times q_n^{internal}, \tag{4.30}$$

where $\Lambda_n = h/\sqrt{2\pi nmkT}$ is the de Broglie wavelength of the cluster and

$$q_n^{internal} = \frac{n^{3/2}}{\Lambda^{3(n-1)}n!}\int d\mathbf{r}'^{n-1}\exp[-\beta U_{eff}]. \tag{4.31}$$

It is better to define an intensive probability distribution

$$\frac{P_n}{N} = \frac{1}{\rho \Lambda_n^3} q_n^{internal} \exp[-\beta \mu n], \tag{4.32}$$

where ρ is the number density of the system. For rare clusters we can write the probability as

$$P_n = p_n(1) + p_n(2) + ... \approx p_n(1), \tag{4.33}$$

where $p_n(i)$ is the probability that there are exactly i clusters of size n. If we assume that the formation of different clusters is uncorrelated $p_n(i) = [p_n(1)]^i$, then we can neglect higher order terms provided the probabilities are small, $p_n(1) \ll 1$. As the average number of clusters of size n is equal to

$$N_n = 1 p_n(1) + 2 p_n(2) + 3 p_n(3) + ... \tag{4.34}$$

we can write in the case of rare clusters

$$\frac{P_n}{N} = \frac{1}{\rho \Lambda_n^3} q_n^{internal} \exp[-\beta \mu n] \approx \frac{N_n}{N} \tag{4.35}$$

We note that this is a classical result and should not depend on Planck's constant h, and, in fact it does not, as the ideal gas part of the chemical potential

$$\mu = \mu^{ex} + kT \ln[\Lambda] \tag{4.36}$$

cancels the h in Λ_n.

The main point of Eq. (4.35) is that we can write down a microscopic expression for the equilibrium number of n-cluster if this number, which is equal to the probability of finding one cluster of size 1, is much less than one.

4.1.2 Identification of solid clusters: Local bond-order analysis

For the identification of solid-like particles we use a local bond-order analysis based on that of ten Wolde [18]. The advantage of this analysis is that it is only sensitive to the overall degree of crystallinity in the system, but independent of any specific crystal structure. This requirement is important as otherwise we would apply an external biasing potential, which could force the system to crystallize in a specific structure. A second advantage is that these bond-order parameters can be constructed so as to be independent of the reference frame.

The local bond-order parameters are a measure of the local structure around a particle and are constructed as follows. First we define a $(2l + 1)$ dimensional complex vector with the components

$$q_{lm}(i) = \frac{1}{N_b(i)} \sum_{j=1}^{N_b(i)} Y_{lm}(\hat{\mathbf{r}}_{ij}), \tag{4.37}$$

where the sum goes over all neighboring particles $N_b(i)$ of particle i. Neighbors are usually defined as all particles that are within a given radius r_q around particle i. $Y_{lm}(\hat{\mathbf{r}}_{ij})$ are the spherical harmonics evaluated for the normalized direction vector $\hat{\mathbf{r}}_{ij}$ between the neighbors. The orientation of the unit vector $\hat{\mathbf{r}}_{ij}$ is determined by the polar and azimuthal angles θ_{ij} and ϕ_{ij}. The rotationally invariant local bond-order parameters are then defined as follows

$$q_l(i) = \left(\frac{4\pi}{2l+1} \sum_{m=-l}^{l} |q_{lm}(i)|^2 \right)^{1/2} \tag{4.38}$$
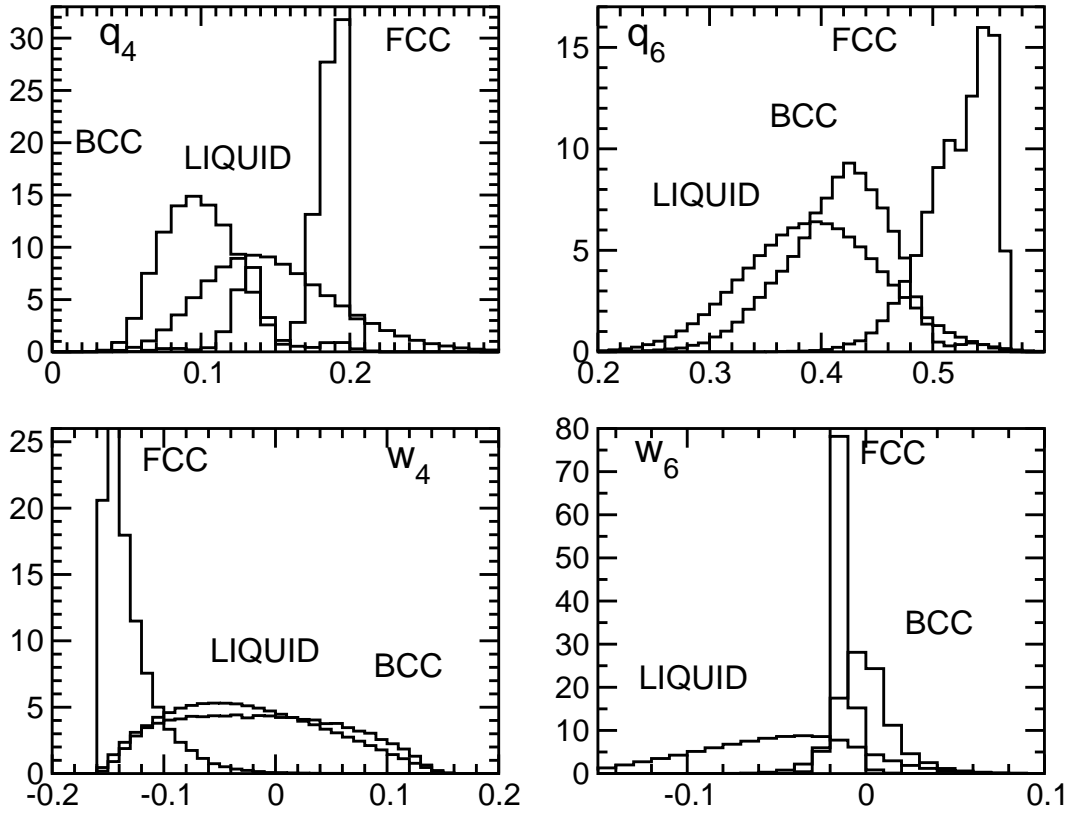
Figure 4.1: Typical distribution functions of the local bond-order parameters from Monte Carlo simulations in a hard-sphere system. Here the cutoff radius r_q for the local environment of a particle is chosen to be 1.4σ, where σ is the hard-core diameter. This means that we included the first, and in some cases also the second nearest neighbors.

and

$$w_l(i) = \frac{\hat{w}_l(i)}{\left(\sum_{m=-l}^{l} |q_{lm}(i)|^2\right)^{3/2}} \tag{4.39}$$

with

$$\hat{w}_l(i) = \sum_{\substack{m_1, m_2, m_3 \\ m_1 + m_2 + m_3 = 0}} \begin{pmatrix} l & l & l \\ m_1 & m_2 & m_3 \end{pmatrix} q_{lm_1}(i) q_{lm_2}(i) q_{lm_3}(i). \tag{4.40}$$

The term in brackets in Eq. (4.40) is the Wigner-3j symbol. These order parameters are sensitive to the degree of orientational correlations of the vectors that join neighboring particles. In simple liquids we expect that there are no preferred orientations around a particle and therefore the correlations decay rapidly. In contrast, for a particle with a solid-like environment the vectors are correlated and as result there should be a clear separation between distribution functions for the bond-order parameter. In Fig. 4.1 we show typical distribution functions of the local bond-order parameters one gets from Monte Carlo simulations of a hard-sphere system, under conditions close to the coexistence point, where the liquid and the solid phase are equally stable. The figure illustrates that there is some separation between the distribution functions obtained from the liquid and those obtained from the solid, but the separation is never very pronounced. Sometimes, there is a separation between the solid structures themselves, a property which we will use later to distinguish between different solid structures. For the identification of solid-like particles we have to choose an order parameter that is able to distinguish between the liquid
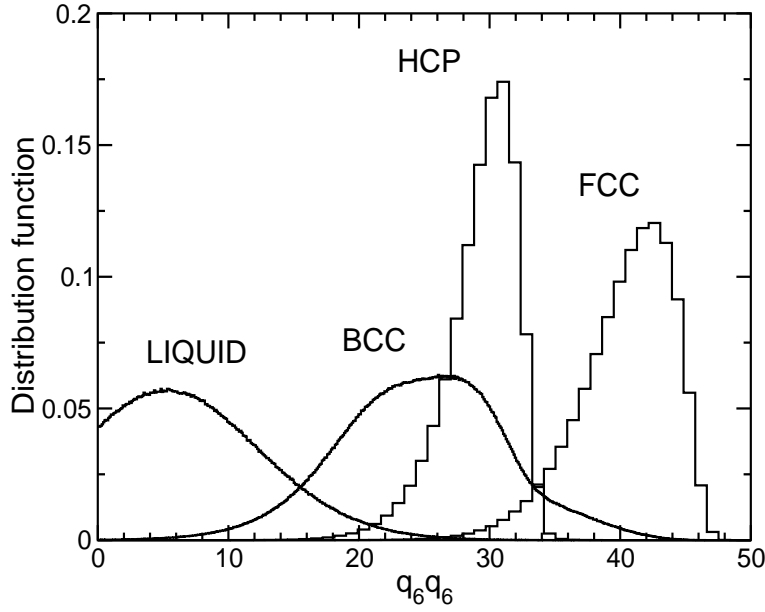
Figure 4.2: Distribution functions of the dot product $\mathbf{q}_6(i) \cdot \mathbf{q}_6(j)$ from Monte Carlo simulations in a hard-sphere system.

and all possible solid structures. From Fig. 4.1 we see that q_6 has some of the desired properties, as the values of the solid phases are all shifted to higher values compared to the liquid. As mentioned above, we can enhance this separation of the distribution function by calculating the correlation function of the vectors $\mathbf{q}_6$ of neighboring particles i and j

$$\mathbf{q}_6(i) \cdot \mathbf{q}_6(j) = \sum_{m=-6}^{6} q_{6m}(i) \cdot q_{6m}(j)^*, \tag{4.41}$$

where the $*$ indicates the complex conjugate. In Fig. 4.2 we show the corresponding distribution functions one get for the hard-sphere system. In this case we did not normalize the dot-product to one, as it just causes additional calculations. In this case the relevant solid structures (FCC, HCP and BCC) yield much higher values for the dot-product than the liquid. We now define two neighboring particles i and j to be connected, if the dot-product exceeds a certain threshold, in our case 20. By using this definition we can identify all particles in a solid to be solid-like, however also in the liquid it happens quite frequently that a particle has more than one connection. To illustrate this, we show in Fig. 4.3 the distribution functions for the number of connections per particle. We note that the peak for the solid structures is at 12 for FCC, HCP and around 13 for BCC. These numbers correspond to the first, or first and second nearest neighbors, which were included in the local environment. In the case of the BCC structure the peak is slightly shifted to lower values, which is due to the fact that the BCC structure is quite disordered. As the BCC lattice of hard-spheres always melts, we could generate all the distribution functions only be adding a polydispersity of 3% to the particles. Therefore it is better to apply a second criterion for particles to be solid-like, which is a threshold to the number of connections a particle has with its neighbors. Thereby we have to consider that for a small nucleus almost all particles are at the surface, and they need to be considered as solid-like as well. For this reason we choose threshold values between 6 and 8. In summary we can say that this analysis provides an unambiguous local criterion to identifying solid-like particles. Finally, we need to have a criterion for identifying clusters. The criterion we applied is that if two solid-like particles are less
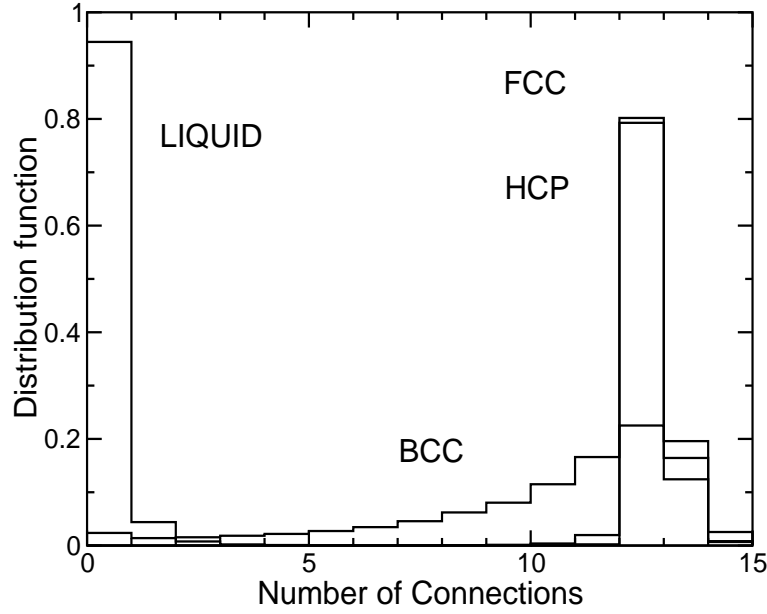
Figure 4.3: Distribution functions of the number of connections per particle from Monte Carlo simulations in a hard-sphere system.

than a certain threshold distance apart, then they belong to the same cluster. This threshold is usually chosen between $1.5\sigma - 2\sigma$.

4.1.3 Monte Carlo simulation

To calculate the nucleation barrier, we need to sample the equilibrium distribution function for the probability $P(n)$, see Eq. (4.2). In section 4.1.1 we derived this probability to be N_n/N, where N_n is the number of clusters of size n in a system containing N particles, see Eq. (4.11) and Eq. (4.35). In the previous section we illustrated how a local bond-order analysis can be used to identify clusters in a system, which will be used for the calculation of $N_n = \langle N_n(\mathbf{r}^N) \rangle$ in a Monte Carlo simulation. This is the subject of this section.

In all cases we performed Monte Carlo simulations in the isobaric-isothermal (NPT) ensemble. In this ensemble the average of a microscopic quantity A is given by

$$\langle A \rangle_{\text{NPT}} = \frac{\int dV \int d\mathbf{r}^N A(\mathbf{r}^N) \exp[-\beta(U(\mathbf{r}^N) + PV)]}{\int dV \int d\mathbf{r}^N \exp[-\beta(U(\mathbf{r}^N) + PV)]}, \tag{4.42}$$

where $U(\mathbf{r}^N)$ is the potential energy of the system with particle positions $\mathbf{r}^N$. $\beta = 1/(k_B T)$ is the reciprocal of the thermal energy, N the number of particles and P the applied pressure. In a Metropolis Monte Carlo simulation the above ensemble average is approximated by

$$\langle A \rangle_{\text{NPT}} \approx \frac{1}{M} \sum_{i=1}^{M} A(\mathbf{r_i}^N), \tag{4.43}$$

where M is the total number of measurements and $A(\mathbf{r_i}^N)$ the value of our property A associated with configuration $\mathbf{r_i}^N$.

In the case of crystal nucleation we need to calculate the average number of clusters of size n and Eq. (4.43) becomes

$$\langle N_n \rangle_{\text{NPT}} \approx \frac{1}{M} \sum_{i=1}^{M} N_n(\mathbf{r_i}^N). \tag{4.44}$$
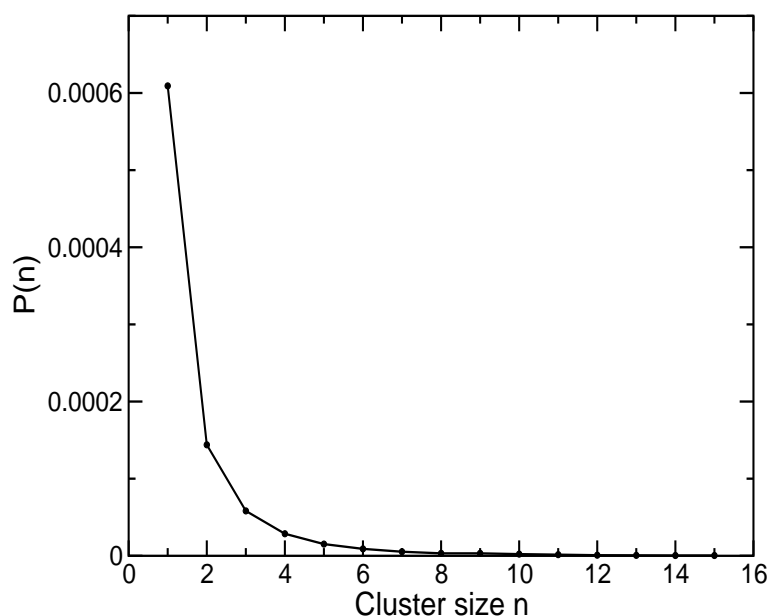
Figure 4.4: Measured probability distribution $P(n)$ from Monte Carlo Simulations in a system of hard-spheres.

As an example we show the results from a Monte Carlo simulations in a system of hard-spheres. In the simulations we used $N = 3375$ particles and applied a pressure $\beta P\sigma^3 = 16$. At this pressure, the liquid phase is meta stable with respect to the solid, but does not crystallize spontaneously as the Gibbs free energy barrier between the two states is too high. The temperature T does not play a role in that system. After equilibrating the system, one could in principle measure the cluster size distribution after every Monte Carlo move, however this would be computationally expensive and statistics would still be poor, as the measurements are strongly correlated. Instead we measure the cluster size distribution after one trajectory, which consists of 20 moves per particle (plus some volume moves) in the case for the simulations in a hard-sphere system. The total length of each simulation was 100000 trajectories. In Fig. 4.4 we show the results for the probability distribution $P(n)$ for the formation of a cluster of size n. From this probability distribution we can calculate the corresponding Gibbs free energy Eq. (4.2) for the formation of such a cluster, which is shown in Fig. 4.5. In this simulation we could measure cluster sizes up to $n = 12$ particles. The formation of larger cluster was so rare that the statistical accuracy was too poor. In order to sample larger cluster sizes we needed to apply the umbrella sampling technique of Torrie and Valleau [22], which we describe in the next section.

4.1.4 Umbrella Sampling with parallel tempering

The umbrella sampling scheme was proposed to handle situations where important contributions to the ensemble average come from configurations whose Boltzmann factor is small, leading to poor statistical accuracy. The method is based on the idea that the ensemble average can
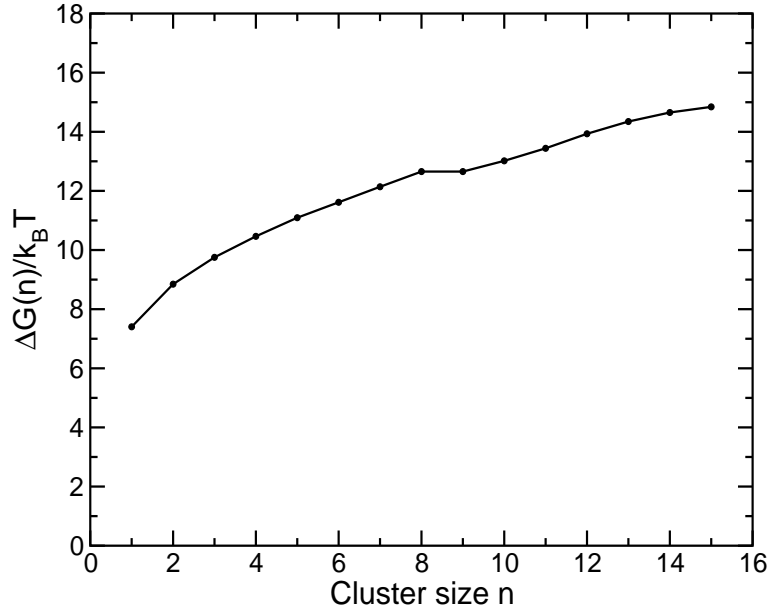
Figure 4.5: Corresponding Gibbs free energy $\Delta G(n)/k_B T = -\ln[P(n)]$ for the formation of a cluster of size n.

be rewritten as follows

$$
\begin{aligned}
\langle A \rangle_{NPT} &= \frac{\int dV \int d\mathbf{r}^N A(\mathbf{r}^N) \exp[-\beta(U(\mathbf{r}^N) + PV)] W(\mathbf{r}^N)^{-1} W(\mathbf{r}^N)}{\int dV \int d\mathbf{r}^N \exp[-\beta(U(\mathbf{r}^N) + PV)] W(\mathbf{r}^N)^{-1} W(\mathbf{r}^N)} \\
&\quad \times \frac{\int dV \int d\mathbf{r}^N W(\mathbf{r}^N) \exp[-\beta(U(\mathbf{r}^N) + PV)]}{\int dV \int d\mathbf{r}^N W(\mathbf{r}^N) \exp[-\beta(U(\mathbf{r}^N) + PV)]} \\
&= \frac{\langle A/W(\mathbf{r}^N) \rangle_W}{\langle W(\mathbf{r}^N)^{-1} \rangle_W},
\end{aligned}
$$

(4.45)

(4.46)

where we have introduced a, as yet, unspecified weighting function $W(\mathbf{r}^N) = \exp[-\beta\omega(\mathbf{r}^N)]$, where $\omega(\mathbf{r}^N)$ is the so-called biasing potential. Instead of performing a Monte Carlo simulation using the original Boltzmann distribution function, we now sample phase space according to the biased distribution function $\exp[-\beta U(\mathbf{r}^N) + PV)] W(\mathbf{r}^N)$, which is indicated by the subscript $\langle ... \rangle_W$. By specifying the weighting function W we can force the system to sample in that region of phase space which is important to improve the statistical accuracy.

In the case of crystal nucleation we can calculate the ensemble average according to the weighted ensemble Eq. (4.46) as follows

$$
\langle N_n \rangle_{NPT} \approx \frac{\sum_i^M [N_n(\mathbf{r_i}^N)/W(\mathbf{r_i}^N)]}{\sum_i^M [W(\mathbf{r_i}^N)^{-1}]},
$$

(4.47)

where the sum goes over all measurements M. We now need to consider the choice of the weighting function. In section 4.1.1 we showed that the probability for the formation of a larger cluster is so small, it can be approximated by the probability to find one cluster of a certain size in the system, see Eq. (4.33). For this reason we can choose a bias potential that just controls the size of the largest cluster in the system. In all cases the bias potential was chosen to be a harmonic function of the size of the largest cluster in the system

$$
\omega[n(\mathbf{r}^N)] = \frac{1}{2} k_n [n(\mathbf{r}^N) - n_0]^2.
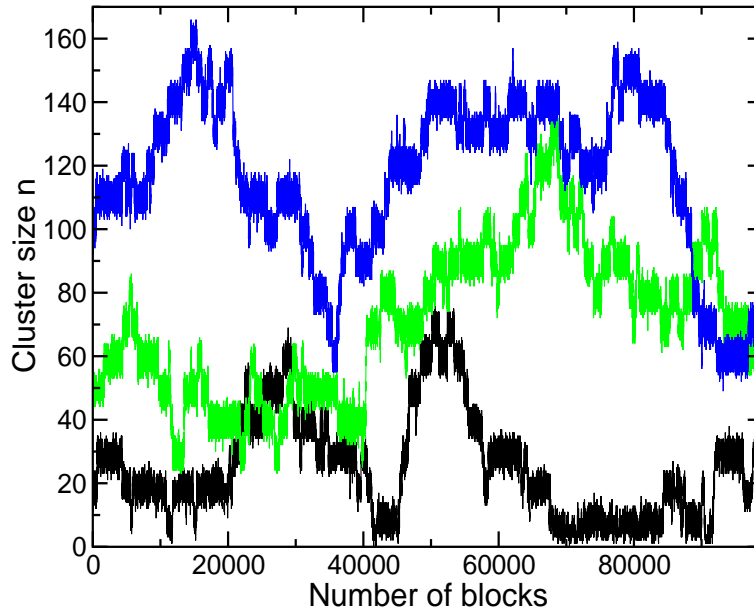$$

(4.48)

Figure 4.6: Examples of the cluster size sampled during one simulation. The different configurations started with clusters of sizes $n = 20, 50$ and 110. Due to the parallel tempering technique, swapping between different windows is possible and the configurations could sample almost all possible cluster sizes.

The constant k_n determines the range of sizes sampled in one simulation, whereas the minimum n_0 determines which cluster sizes are sampled most.

The implementation of the biasing potential in the Monte Carlo simulation is straightforward. As in the unbiased run we try to avoid calculating the size of the largest cluster after every Monte Carlo move. Instead we perform a trajectory of a certain number of Monte Carlo moves per particle according to the unbiased potential $U(\mathbf{r}^N)$. We then re-calculate the cluster size and accept or reject the whole trajectory according to the pure biasing potential $\exp[-\beta\Delta\omega]$, where $\Delta\omega$ is the difference in the biasing potential after and before the trajectory. This is equivalent to applying the bias potential after every trial move, but computationally much cheaper. Intuitively, it might seem easier to sample all cluster sizes in one run, but it can be shown that this is not the case [7], mainly because such a simulation would take too long. Instead we split the simulation into a number of smaller simulations that were restricted to sample a sequence of narrow, but overlapping windows of different cluster sizes n. In practice it turned out that it is best to sample only about 15 different cluster sizes in one window, to ensure high accuracy. This implies that the sequence of minima needed to be placed in steps of ten $n_0 = 10, 20, ...,$ up to sizes slightly larger than critical cluster size.

In addition we implemented the parallel tempering scheme of Geyer and Thompson [23]. The main reason for using this scheme is that stacking rearrangements in the nuclei are very slow. With the parallel tempering scheme the phase space can be sampled more efficiently. The idea is to run all the simulations in the different windows in parallel and allow them to exchange clusters between adjacent windows.

To illustrate this, we consider again the example of the hard-sphere system. In this case we needed to calculate the Gibbs free energy of a cluster up to a size of about $n = 170$. We therefore split the simulations into 16 windows, where the sequence of minima was placed in steps of ten: $n_0 = 10, 20, ..., 160$. In order to obtain the 16 starting configurations we grew clusters from the liquid. We always started from the liquid, applying the bias potential with $n_0 = 10$. Every
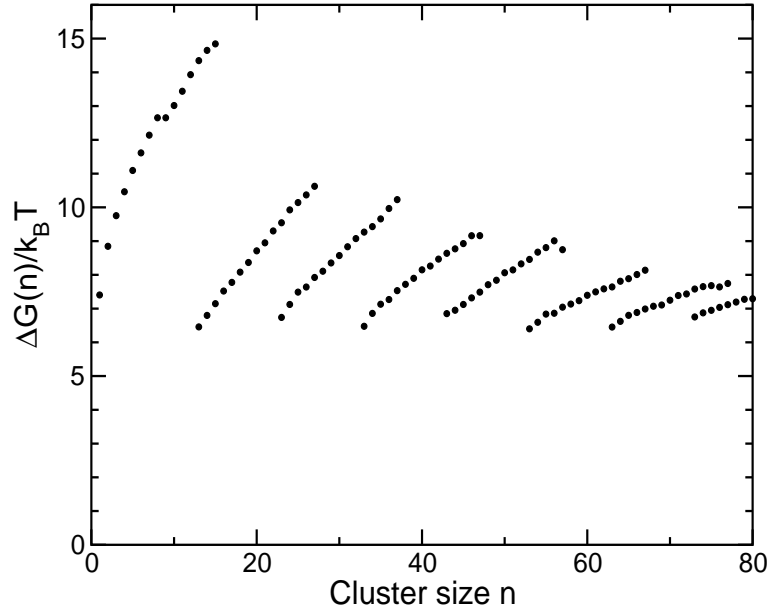
Figure 4.7: Sequence of measured Gibbs free energies $\Delta G_i(n)/k_BT + b_i$ from Monte Carlo Simulations in a system of hard-spheres in different windows.

time a cluster was stabilized, the minimum n_0 was increased in steps of 10. In the parallel tempering simulation we started all simulations at the same time, but stopped them after 5 trajectories, to allow neighboring windows to exchange clusters. Before that, we need to decide which sequence we should use to change, either the windows $n_0 = 10$ with 20, 30 with 40, and so on, or the sequence 20 with 30, 40 with 50, and so on. This was done by generating a random number. The actual change between windows i, j is accepted according to $\exp[-\beta(w_n - w_o)]$, where $w_o = k_i/2(n_i - n_{0,i})^2 + k_j/2(n_j - n_{0,j})^2$ is the energy of the biasing potential before and $w_n = k_i/2(n_j - n_{0,i})^2 + k_j/2(n_i - n_{0,j})^2$ after the change. In practice it is more convenient to exchange the minima of the bias potential rather than configurations. This requires much less communication between different computer nodes. As a result, each initial configuration is able to reach in principle all cluster sizes in course of the simulation. In Fig. 4.6 we show the cluster sizes sampled during one simulation for three configurations, which started with cluster sizes $n_0 = 20, 50$ and 110. The value for the constant of the bias potential was $k_n = k = 0.15$ in all windows. As in the unbiased run, the length of one trajectory was 20 moves per particle (plus some volume moves) and in total we performed 100000 trajectories.

In Fig. 4.7 we show the results for the Gibbs free energy of a nucleus obtained from the simulations in each window (unbiased+biased runs). The Gibbs free energies in the different windows are determined up to a constant $\Delta G_i(n)/k_BT + b_i$, where the subscript i indicates the number of the window. In order to determine the constants b_i we fitted all the free energy estimates in the different windows to one polynomial in n. This can be done by a linear least-square fit, where we minimize

$$\chi = \sum_{n=1}^{n_{max}} \left\{ \sum_{i=1}^{n_w} w_i(n)[\Delta G_i(n) - \sum_{k=1}^{k_{max}} a_k n^k - b_i]^2 \right\}. \qquad (4.49)$$

Here $w_i(n) = 1/\sigma^2_{\Delta G_i(n)}$ is the statistical weight determined by the variance $\sigma^2_{\Delta G_i(n)}$ of the free energy measurement and n_w the total number of windows used in the simulation. The maximum order of the polynomial used was $k_{max} = 10$. The linear least-square fit can be performed
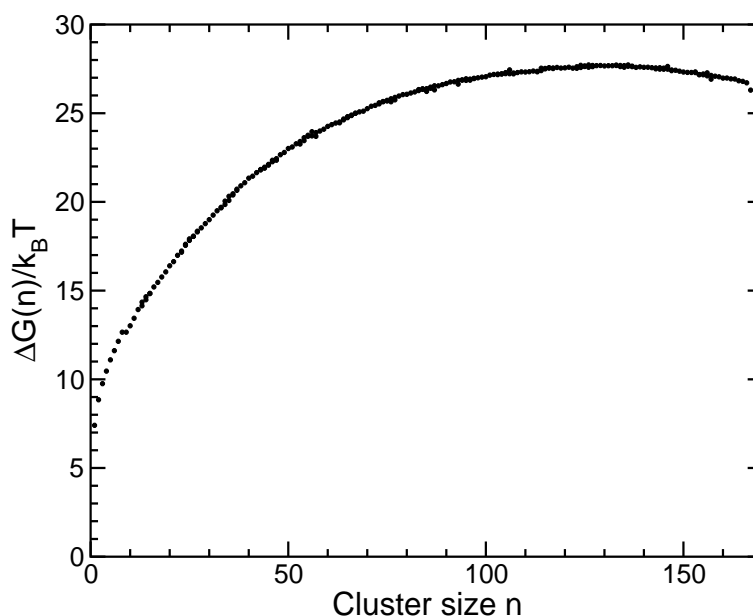
Figure 4.8: Gibbs free energy for the formation of a cluster of n hard-spheres, after fitting the results for the free energy in the different windows to one polynomial.

by using the algorithms in Ref. [24]. Note that by using a high-order polynomial, we do not assume a functional form of the nucleation barrier (the barrier might be correctly described by CNT). From the unbiased simulation we get the absolute Gibbs free energy for the formation of a cluster of size n with respect to the liquid state. Therefore the constant b_1 is known. In Fig. 4.8 we show the final result for the calculation of a nucleation barrier in a hard-sphere system.

4.2 Calculation of the kinetic prefactor

4.2.1 General approach

We have developed a new scheme for the calculation of the kinetic factor for diffusive barrier crossing. Traditionally the kinetic factor has been calculated using the Bennett-Chandler scheme or a more efficient revised version by Ruiz-Montero et al., as discussed in chapter 2. The principle of both methods is to generate a large number of independent configurations at the top of the barrier. These configurations are then used as the starting point for an unbiased trajectory in which one determines weather the nucleus grows and the system crystallizes, or if it shrinks. From the number of nuclei that grow and shrink one can extract the kinetic factor. However, in order to get a reasonable estimate one has to simulate a rather large number of trajectories. In a more recent publication ten Wolde et al. [25] applied the approach of Ref. [9] to calculate the rate of gas-liquid nucleation rate in a Lennard-Jones system. They used over 300 trajectories of length about 5000 time steps in a isobaric-isothermal MD simulation and still had statistical errors in the transmissions coefficient of about 100%. Here we use a different approach that is more efficient for the present problem. Looking closer at the kinetic factor, $\kappa = Z\rho_{liq}f_{n_{crit}}^{+}$ (Eq. (4.11) and Eq. (4.35)), we see that, after the calculation of the nucleation barrier, the only quantity that we have to compute is the attachment rate $f_{n_{crit}}^{+}$ of particles to the critical cluster. The Zeldovitch factor Z is already known from the barrier calculation. In order to compute $f_{n_{crit}}^{+}$, we assume that the critical cluster grows and shrinks via the diffusive attachment of single particles. We can then define an effective diffusion constant for the change in critical cluster
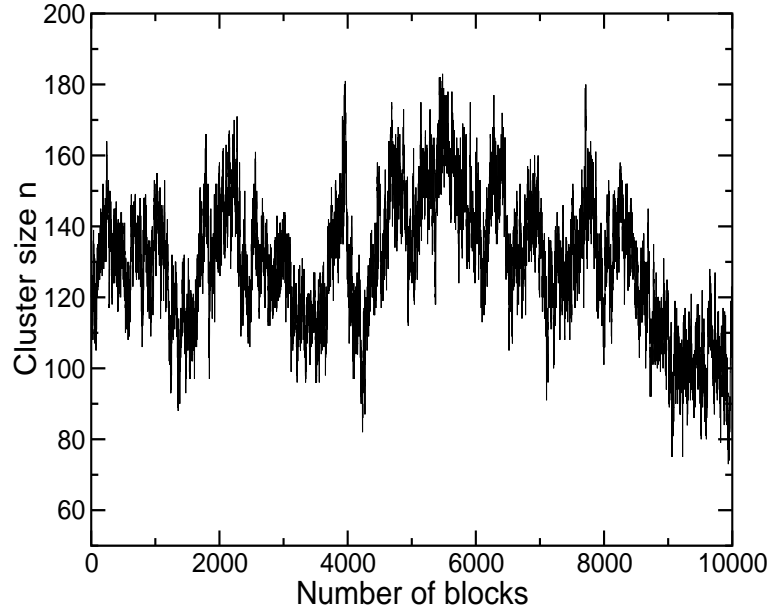
Figure 4.9: The figure shows the development of the size n of the critical cluster during one trajectory at volume fraction $\phi = 0.5277$. Here one block is 100 moves per particle in an NVE Monte Carlo simulation. Note in particular the fluctuations of the cluster size about its critical value

size:

$$D_{n_{\mathrm{crit}}}^{\mathrm{att}} = \frac{1}{2}\frac{\langle \Delta n_{\mathrm{crit}}^2(t)\rangle}{t}. \tag{4.50}$$

Here $\Delta n_{n_{\mathrm{crit}}}^2(t) = [n_{\mathrm{crit}}(t) - n_{\mathrm{crit}}(t=0)]^2$ is the mean square change in the number of particles in the critical cluster. As the slope of this change is related to the corresponding attachment rates via $\langle \Delta n_{\mathrm{crit}}^2(t)\rangle/t = (f_{n_{\mathrm{crit}}}^+ + f_{n_{\mathrm{crit}}}^-)/2$, and as we know that the forward and backward rates are equal $f_{n_{\mathrm{crit}}}^+ = f_{n_{\mathrm{crit}}}^-$ at the top of the barrier we get

$$f_{n_{\mathrm{crit}}}^+ = \frac{1}{2}\frac{\langle \Delta n_{\mathrm{crit}}^2(t)\rangle}{t}. \tag{4.51}$$

This is a general expression for the calculation of the kinetic factor for diffusive barrier crossing. It also connects the expressions from Eq. (2.20) and Eq. (3.7). Using a Molecular Dynamics simulation one only needs to measure the change in size of the critical cluster as a function of time. The only restriction is that, during the measurement, the critical nucleus needs to fluctuate around its critical value. One therefore needs to run a couple of trajectories and select the data where this is the case. In the next section we show how we applied this method to a system of hard-sphere colloids.

4.2.2 Application to hard colloidal spheres

In principle, it is straightforward to apply the above method to the calculation of a kinetic factor for crystal nucleation. However, in the case of hard colloidal spheres one needs to have a simulation method that generates trajectories following Brownian dynamics, and the effect of hydrodynamic interactions also needs to be considered. Trajectories following Brownian dynamics could be generated using a kinetic Monte Carlo scheme proposed by Hinsen and Cichocki [26]. These authors show that, in the limit of very small maximum particle displacement,
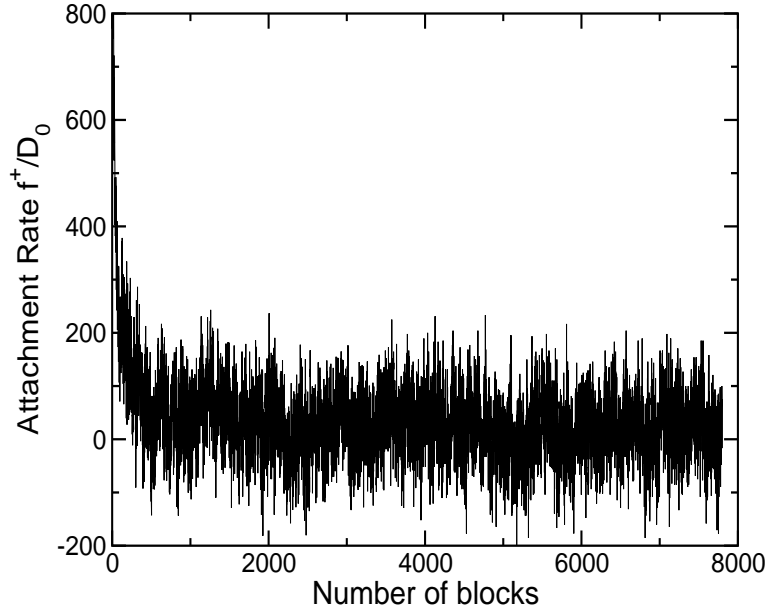
Figure 4.10: Attachment rate of particles to the critical cluster at volume fraction $\phi = 0.5277$. The attachment rate for short times is much higher than for long times. As the diffusion time of a cluster over the nucleation barrier is in the range of the long time behavior of the attachment rate, this value has to be used.

$\Delta x_{max} \to 0$, the trajectories generated by the kinetic Monte Carlo simulation are stochastically equivalent to the process described by the Smoluchowski equation. The limit $\Delta x_{max} \to 0$ means that simulation time would become infinitely long. However, Hinson and Cichocki also propose an extrapolation procedure with which this limit can be approached systematically by repeating simulations with a smaller maximum displacement. In experiments nucleation rates are usually presented in dimensionless form $k\sigma^5/D_0$, where σ is the diameter of a monomer and D_0 the free diffusion coefficient. Therefore we only need to compute the ratio $f^+_{n_{crit}}/D_0$. First we computed the nucleation barrier using a biased NPT Monte Carlo simulation. From these simulations we could determine the critical cluster size and had generated independent configurations in which such a cluster was stabilized. We used these configurations, to perform an unbiased kinetic NVE Monte Carlo simulation, measuring the size of the critical cluster as a function of Monte Carlo cycles. Here one cycle is 10 trial moves per particle. In Fig. 4.9 we show such a measurement at $\phi = 0.5277(P = 16)$. From these data we then extracted the attachment rate using Eqn. (4.51) (see Fig. 4.10). Surprisingly, we see that the attachment rate has a different short time and long time behavior. This implies that, at short times, the diffusion in cluster size is not a Markov process. As the diffusion of the critical cluster over the nucleation barrier is on the time scale of the long time behavior of the attachment rate, this is the value we have to use. To test the dependence of our results on the maximum particle displacement we performed simulations for two different values $\Delta x_{max} = 0.12\sigma$ and 0.012σ. The corresponding values for the free diffusion coefficients are $D_0 = \langle \Delta x^2_{max} \rangle/6$. The ratio of the results for $f^+_{n_{crit}}/D_0$ in both simulations is equal to 4.79. Computing the long time self diffusion coefficient $D^L_S/D_0 = \langle (r(0) - r(t))^2 \rangle/6tD_0$ we get a ratio in both simulations of 5.07. Therefore the difference in the results for the attachment rate is mainly due to diffusion. In our simulations we did not follow the extrapolation procedure for $\Delta x_{max} \to 0$ described in [26], as for $\Delta x_{max} = 0.012\sigma$ we are already in a limit where the attachment rate has effectively reached its limiting value. We justify this by testing our approach on the calculation of the long time self diffusion coefficient, which will be discussed later. So
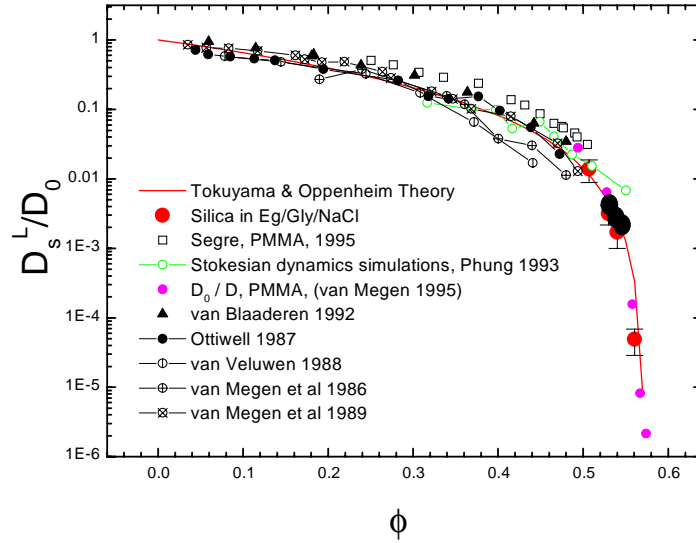
Figure 4.11: Reduced long time self diffusion coefficients D_S^L/D_0 from Monte Carlo simulations compared with experimental measurements. Our simulation results (large black filled circles) are in the range of the statistical errors of the experimental studies.

far in our simulations we did not include the effect of hydrodynamic interactions, which is certainly important at high volume fractions. As proposed by Medina-Noyola [27], we corrected for this effect by replacing the free diffusion coefficient D_0 by the short time self diffusion coefficient D_S^S. We therefore have to multiply our result by a factor $\alpha = D_S^S/D_0$. There are several rather similar functional forms for this factor proposed in the literature. Here we used the phenomenological expression $(1 - \phi/0.64)^{1.17}$ [28], where ϕ is the volume fraction. As a test of our approach, we computed the long-time self diffusion coefficient D_S^L. We could reproduce experimental data within statistical error. The results for the long-time self diffusion coefficient are shown in Fig. 4.11. The resulting value for the reduced attachment rate for our example was $f_{n_{\mathrm{crit}}}^+/D_0 = 21$. For the calculation of the kinetic factor we usually performed about 5 trajectories. The length of the trajectory depends on whether the cluster size fluctuates around the critical size or not; if not the simulation is stopped. From these simulations we calculated the attachment rate. The error estimates vary between a factor of one for the larger critical cluster sizes and a factor of two to three for the smaller cluster sizes. In the regime of smaller critical cluster sizes, the fluctuations in cluster size are almost on the order of the critical cluster size and it becomes therefore more difficult to get a good estimate. To compare the efficiency of our scheme with the previous one we need to compare the number of trajectories to run, but also the absolute length of the trajectory itself. The latter is difficult to compare as different systems were simulated with different algorithms. However, as the number of trajectories we used is about two orders of magnitude fewer the power of our scheme is clear.

Part II

Application to spherical colloids

5

Prediction of absolute crystal-nucleation rate in hard-sphere colloids

Crystal nucleation is a much-studied phenomenon, yet the rate at which it occurs remains difficult to predict. The reason is that the rate-limiting step - the formation of a so-called critical nucleus - cannot easily be probed experimentally. Small crystal nuclei can form spontaneously in a supersaturated solution. But, unless their size exceeds a critical value, they will dissolve rather than grow. The crystal-nucleation rate depends on P_{crit}, the (very small) probability that a critical nucleus forms spontaneously, and on κ, a factor that measures the rate at which critical nuclei grow. Given the absence of a priori knowledge of either quantity, classical nucleation theory [17] (CNT) is commonly used to analyse crystal nucleation experiments, with the unconstrained parameters adjusted to fit the observations. This approach yields no first principles prediction of absolute nucleation rates. Here we approach the problem from a different angle, simulating the nucleation process in a suspension of hard colloidal spheres, to obtain quantitative numerical predictions of crystal nucleation rates. We find large discrepancies between the computed nucleation rates and those deduced from experiment [3,29,30]: the best experimental estimates of P_{crit} seem to be too large by several orders of magnitude.

5.1 Introduction

The probability (per particle) that a spontaneous fluctuation will result in the formation of a critical nucleus, depends exponentially on the free energy ΔG_{crit} that is required to form such a nucleus:

$$P_{crit} = \exp(-\Delta G_{crit}/k_B T), \qquad (5.1)$$

where T is the absolute temperature and k_B is Boltzmann's constant. According to CNT the total free energy of a crystallite that forms in a supersaturated solution contains two terms: the first is a "bulk" term that expresses the fact that the solid is more stable than the supersaturated fluid - this term is negative and proportional to the volume of the crystallite. The second is a "surface" term that takes into account the free-energy cost of creating a solid-liquid interface. This term is positive and proportional to the surface area of the crystallite. According to CNT, the total (Gibbs) free-energy cost to form a spherical crystallite with radius R is

$$\Delta G = \frac{4}{3}\pi R^3 \rho_S \Delta\mu + 4\pi R^2 \gamma, \qquad (5.2)$$

where ρ_S is the number-density of the solid, $\Delta\mu$ (< 0) the difference in chemical potential of the solid and the liquid, and γ is the solid-liquid interfacial free energy density. The function ΔG goes through a maximum at $R = 2\gamma/(\rho_S|\Delta\mu|)$ and the height of the nucleation barrier is

$$\Delta G_{crit} = \frac{16\pi}{3}\gamma^3/(\rho_S|\Delta\mu|)^2. \tag{5.3}$$

The crystal-nucleation rate per unit volume, I, is the product of P_{crit} and the kinetic prefactor κ:

$$I = \kappa \exp(-\Delta G_{crit}/k_B T). \tag{5.4}$$

The CNT expression for the nucleation rate then becomes

$$I = \kappa \exp\left[-\frac{16\pi}{3}\gamma^3/(\rho_S|\Delta\mu|)^2\right]. \tag{5.5}$$

This expression has been used extensively to *analyze* a crystal-nucleation experiments. However, as a rigorous theory for the kinetic prefactor is lacking, CNT has not been very successful in *predicting* absolute nucleation rates. Rather, the kinetic prefactor κ and, more often than not, the effective interfacial free energy γ are *fitted* to match the experimental nucleation rates [17]. This situation is now changing. The computer simulations that we report in this Letter, allow us to predict absolute crystal nucleation rates without making use of any adjustable fit parameters nor, for that matter, of the assumptions underlying CNT. It is obviously important to compare the simulation results with crystal-nucleation experiments on a system that is very well characterized. For this reason, we chose to simulate crystal nucleation in suspensions of hard-sphere colloids. The hard-sphere freezing transition is probably better characterized than any other. Moreover, several groups have performed experimental studies of crystal nucleation in suspensions of hard-sphere colloids [3, 29–31]. Experimental nucleation rate densities are usually expressed in dimensionless form: $I^* \equiv I\sigma^5/D_0$. Here σ is the hard-core diameter of the colloidal particles and D_0 is their self-diffusion coefficient at infinite dilution. In what follows, we always use reduced quantities and hence we will omit the superscript $*$. We use σ as our unit of length, $k_B T$ as our unit of energy and σ^2/D_0 as our unit of time. In the analysis of experiments on hard-core colloids, the kinetic prefactor κ is usually written as $A\phi_{liq}^{5/3}D(\phi_{liq})$, where ϕ_{liq} is the volume fraction of the colloids in the liquid phase, $D(\phi)$ is the (known) reduced diffusivity at volume fraction ϕ, while A and γ are treated as adjustable parameters [3, 28, 30]. Note that, even apart from the use of adjustable parameters to fit the data, the experimental tests of CNT for hard-sphere freezing are, at present, rather indirect as experiments do not probe the shape of the nucleation barrier directly. Nor do they provide information about the *structure* of the critical nucleus.

5.2 Crystal nucleation barrier

We have performed numerical simulations of hard-sphere colloids, that allow us to compute the shape and height of the nucleation barrier and the structure of the critical nucleus. In addition, we have performed kinetic Monte Carlo simulations to compute the kinetic prefactor κ. These allow us to compare our simulation results for the reduced nucleation rate (without adjustable parameters) with the values of I determined in experiment [3, 29, 30].

To study the formation of a critical crystal nucleus, we used the biased Monte Carlo method described in Refs. [25, 32] . This scheme allows us to compute the equilibrium probability $P(n)$ for the formation of a crystalline cluster of size n. The (Gibbs) free energy of a cluster of size n is given by:

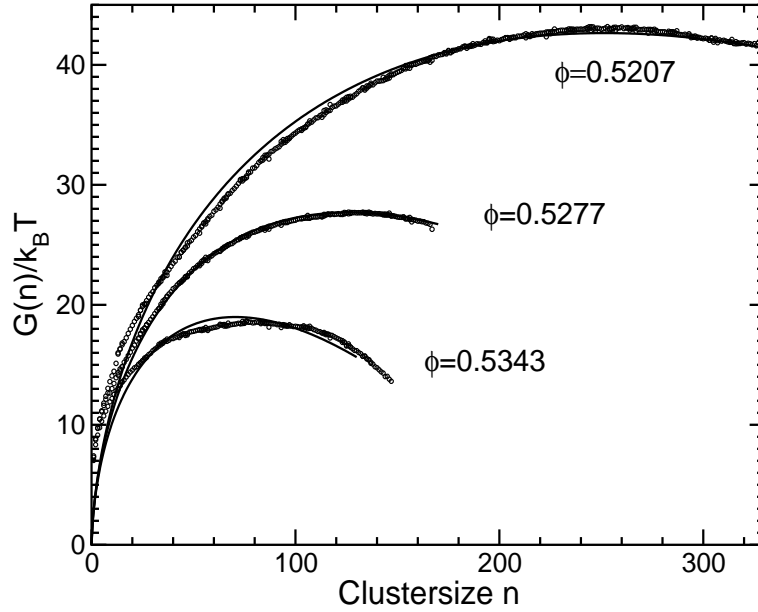$$G(n) = const. - \ln[P(n)]. \tag{5.6}$$

Figure 5.1: Calculated free energy barrier for homogeneous crystal nucleation of hard-sphere colloids. The results are shown for three values of the volume fraction. From top to bottom: $\phi_{liq} = 0.5207, 0.5277$ and 0.5343. The drawn curves are fits to the CNT-expression (Eq. 5.2). The fits yield the following values: $\gamma_{eff}(P = 15) = 0.71$, $\gamma_{eff}(P = 16) = 0.737$ and $\gamma_{eff}(P = 17) = 0.751$.

We computed the nucleation barrier as a function of the cluster size n for hard-sphere fluids that were compressed above the coexistence pressure $P_{coex} = 11.67$ [33]. Simulations were carried out at reduced pressures $P = 15, 16$ and 17, corresponding to volume fractions of the liquid $\phi_{liq} = 0.5207, 0.5277$ and 0.5343. These state points correspond to the lower range of supersaturations where hard-sphere nucleation was studied experimentally [3,29,30].The reason for selecting this density regime is that at higher supersaturations, many crystal nuclei form simultaneously.

Fig. 5.1 shows the computed excess Gibbs free energy associated with the formation of a cluster of size n in a supercooled liquid. The top of the barrier determines ΔG_{crit} and the critical nucleus size. Comparing our results for ΔG_{crit} with the best experimental estimates, we find that the latter are three times too low [3, 30]. One possible source of discrepancy could be that we simulated monodisperse suspensions, while the experimental systems have a size-polydispersity of approximately 5%. We therefore repeated the simulations for a system with 5% polydispersity. However, we found that the only effect of polydispersity is to shift the coexistence curve. To within the numerical error in ΔG_{crit} ($\pm 1 k_B T$), the monodisperse and polydisperse suspensions have the same nucleation barrier at the same supersaturation (i.e. at the same value of $\Delta\mu$). We also compared the computed nucleation barriers with the predictions based on CNT. The dependence of ρ_S and $\Delta\mu$ on P can be accurately computed using the phenomenological equations of state for the solid and fluid phase of hard spheres [34], see appendix 5.6. For γ we take a recent numerical estimate [6]. The resulting CNT predictions for ΔG_{crit} are 30 to 50% too low. These deviations are not small. For instance, for a barrier height of $40 k_B T$, an error of 30% in ΔG_{crit} implies an error of $\mathcal{O}(10^5)$ in $\exp(-\Delta G_{crit}/k_B T)$ and the experimental estimate of $\exp(-\Delta G_{crit}/k_B T)$ is even off by a factor $\mathcal{O}(10^{11})$! While the computed barrier heights are not predicted correctly by CNT, we can still fit our data to the functional form given by CNT (Eq.5.2). Using $n = 4\pi\rho_S R^3/3$, we can express Eq. 5.2 in terms of the cluster size n. The

only adjustable parameter in our fit of the simulation data is the effective interfacial free-energy density γ_{eff}. The figure shows that CNT reproduces the functional form of the nucleation barrier, except for very small clusters. The fit yielded the following values: $\gamma_{eff}(P = 15) = 0.71$, $\gamma_{eff}(P = 16) = 0.737$ and $\gamma_{eff}(P = 17) = 0.751$. Again, we find the same answer for the system with 5% polydispersity: i.e. at the same supersaturation we obtain the same values for γ_{eff} of the monodisperse and polydisperse samples. We note that the numerical estimate of γ_{eff} is higher than the value deduced from the analysis of experimental nucleation data: the data-analysis of Refs. [3, 30] suggests that $\gamma_{eff} = 0.5$. As $\Delta G_{crit} \sim \gamma_{eff}^3$, the experimental estimate of ΔG_{crit} is a factor three too low. If we assume that γ_{eff} depends linearly on pressure, then our simulation results extrapolate to a value of $\gamma \approx 0.64$ at coexistence - in surprisingly good agreement with the numerical estimate [6]. However, in the regime where nucleation experiments have been performed, we find much larger values for γ_{eff} (between 0.7 and 0.75). CNT fails because it uses the value of γ at coexistence in Eq. 5.3 to predict ΔG_{crit}.

5.3   Crystal nucleation rate

Our simulations allow us to give the first parameter-free estimate of the crystal nucleation rate. To this end, we need to compute the reduced kinetic prefactor κ. It has the following form $\kappa = Z\rho f_{n_c}/D_0$, where Z is the Zeldovitch factor [17], ρ is the number density of the supersaturated liquid, and f_{n_c} is the addition rate of particles to the critical nucleus. The Zeldovitch factor $Z = \sqrt{|\Delta G''(n_{crit})|/(2\pi k_B T)}$ can be obtained directly from the simulation results. We have computed f_{n_c}/D_0 using kinetic Monte Carlo simulations of the hard-sphere suspension [26]. In such simulations, the effect of hydrodynamic interactions between colloids is ignored. However, in the spirit of ref. [27], we correct for this effect by multiplying our MC results for f_{n_c} with a factor $\alpha(\phi) \equiv D^s(\phi)/D_0$, where $D^s(\phi)$ is the short-time self-diffusion coefficient at volume fraction ϕ. Several, rather similar, functional forms for $\alpha(\phi)$ have been proposed in the literature. Here we use the phenomenological expression $\alpha(\phi) = (1 - \phi/0.64)^{1.17}$ [28]. When applying the same approach to the computation of the long-time self-diffusion constant, we reproduce the experimental data in the same density range (see [30]) to within the statistical error. We estimate that the error in $\ln \kappa$ is ± 1, i.e. about the same as the error in $\Delta G_{crit}/k_B T$. Figure 5.2 shows our numerical estimate for the reduced nucleation rate I. We have computed I both for a monodisperse suspension and for a suspension with 5% polydispersity. The latter results can be compared directly with the experimental studies of steady-state nucleation [3, 29, 30]. In Ref. [35] the polydispersity is about 2.5%. As can be seen in figure 5.2, the simulated and experimental curves almost intersect, but for most densities we observe discrepancies of many orders of magnitude. Such discrepancies are real and worrisome, as we estimate that our computed nucleation rates are accurate to within one order of magnitude. We therefore argue that the problem must be with the interpretation of the experiments. Hopefully, future "real-space" experiments will provide an explanation for the discrepancy in the computed nucleation rates and barrier heights.

5.4   Structure analysis

The simulations allow us to address a question that cannot, at present, be answered experimentally: *what is the structure of the critical nucleus?* Fig. 5.3 shows an example of a snapshot of a critical nucleus observed in our simulations. CNT makes the assumption that the (pre) critical nuclei are effectively spherical and have the same structure as the stable bulk phase that is nucleating. However, already in 1897, Ostwald pointed out [36] that the phase that nucleates need
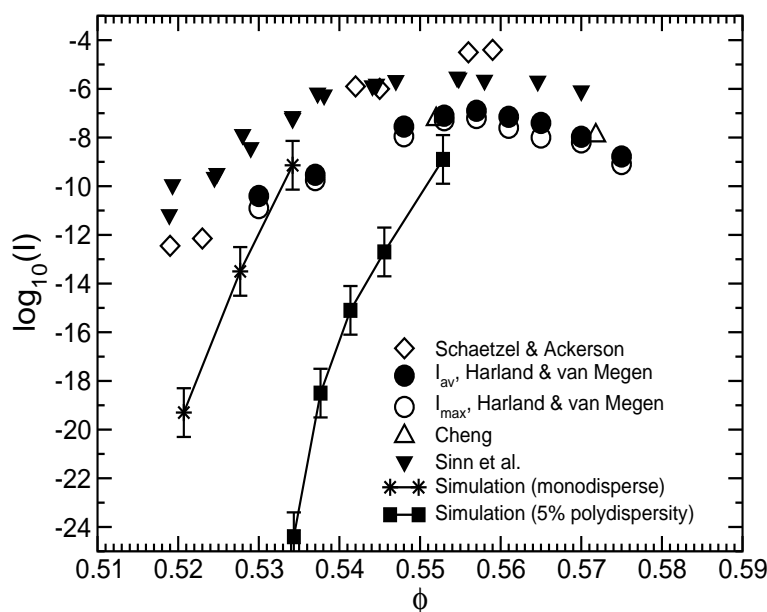
Figure 5.2: Reduced nucleation rates I as a function of the volume fraction of the meta-stable liquid. The simulation data for monodisperse colloids are indicated by the *- the drawn curve joining the simulation points is meant as a guide to the eye. In the same figure we show the experimental results of Ref. [29](◇), Ref. [3](○ and ●), Ref. [30](△) and Ref. [35](▼). We also performed simulations on model systems that have the same polydispersity (5%) as the experimental systems. These simulation results are denoted by the filled squares. The discrepancy between the latter simulations and experiment is unexpected and significant. Several factors could complicate the comparison with the available experiments: firstly, the experiments yield a "time-averaged" nucleation rate that may differ from the steady-state rate that we compute. Secondly, it is conceivable that the experimental systems contain some pre-critical nuclei.

not be the one that is thermodynamically stable. In recent years, several attempts have been made to provide a microscopic explanation for Ostwald's observation [37–39]. Alexander and McTague [37] have argued, on the basis of Landau theory, that in the early stages of crystal nucleation a bcc crystallite should form that would subsequently transform into the stable crystal phase. In fact, simulations of pre-critical nuclei in a Lennard-Jones ("argon") liquid, are indeed found to have a bcc structure, rather than the stable fcc structure [25]. In the case of hard spheres, it is known that the stable crystal structure is face-centered cubic - but this fcc phase is only slightly more stable than the hexagonal close packed (hcp) phase [40]. In fact, the fcc − hcp free-energy difference is so small, that small hard-sphere crystals will always contain an equilibrium concentration of stacking faults [31, 41–43]. It would clearly be interesting to know by what route hard-sphere crystals nucleate: does the small size lift the effective degeneracy between fcc and hcp structures to the extent that one of these dominates, or do hard-sphere crystal nuclei obey the predictions of the Alexander-McTague theory and exhibit a bcc or possibly even icosahedral structure? To answer this question we analysed the structure of the crystalline nucleus. The stable structure of a bulk hard-sphere solid is fcc [40]. However, as the free energy of stacking faults is small [42, 43] small crystallites are expected to exhibit random stacking of fcc and hcp domains. Indeed, direct inspection of the crystal nuclei generated in our simulations show that the critical nucleus is randomly stacked. The next question to ask is if there is any evidence for bcc or *icosahedral* ordering. To this end, we used the analysis technique of ten Wolde et al. [25]. This approach allows us to analyse any cluster structure as a mixture of sim-
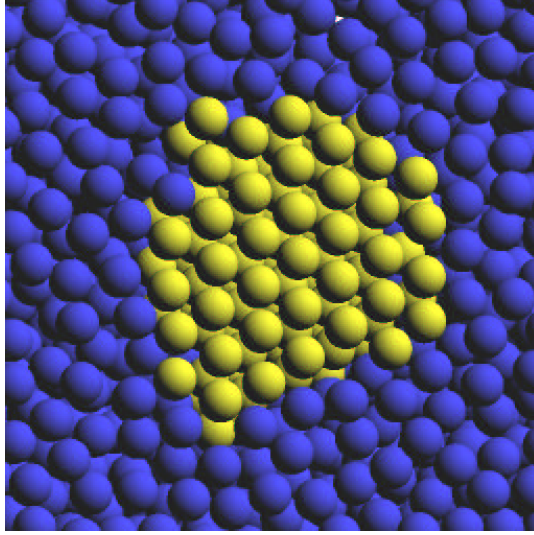
Figure 5.3: Snapshot of a cross-section of a critical nucleus of a hard-sphere crystal at a liquid volume fraction $\phi = 0.5207$. The figure shows a three-layer thick slice through the center of the crystallite. Solid-like particles are shown in yellow and liquid-like particles in blue. The layers shown in the figure are close-packed hexagonal crystal planes. The stacking shown in this figure happens to be fcc-like, i.e. ABC-stacking - however, analysis of many such snapshots showed that fcc and hcp stackings were equally likely.

ple reference structures. We assume that pre-critical nuclei need not have the random-stacked close-packed (rhcp) structure. Rather, we allow for the possibility that the nuclei exhibit a signature characteristic of bcc, *icosahedral* or even *liquid-like* ordering. Every structure is characterized by a set of numbers f_{bcc}, f_{rhcp}, f_{icos}, f_{liq}, where the value of f_α denotes the relative importance of structure α in the cluster. In Fig. 5.4 we show the results for f_{bcc}, f_{rhcp}, f_{icos} and f_{liq} as a function of the size of the largest cluster in the system at P = 15. The results for P = 16 and 17 are qualitatively similar. The figure shows that icosahedral ordering is not observed for any nucleus size. Small clusters still have some bcc or *liquid-like* signature. But in all cases the rhcp signature is dominant. The same conclusion holds for the weakly polydisperse crystals that we studied. This observation is interesting, as it shows that the simplest of all crystals does not confirm the theoretical prediction that bcc (or icosahedral) (pre)nuclei should be favored in the crystallization of simple liquids [37–39]. Our finding is also unexpected in the light of the finding that pre-critical Lennard-Jones nuclei have a bcc structure [25]. As the structure of simple liquids is known to be dominated by the short-ranged repulsive forces, one would have expected that the structure of the pre-critical nucleus in hard-sphere fluids would be bcc, as in the Lennard-Jones case. Random hexagonal close packing (*rhcp* stacking) in freshly nucleated colloidal hard-sphere crystals has been observed in several experiments [31, 41]. It is usually assumed that the origin of the *rhcp* stacking is purely kinetic. While this may be correct for larger crystals, the present simulation indicates that, in the early stages of nucleation, the *rhcp*
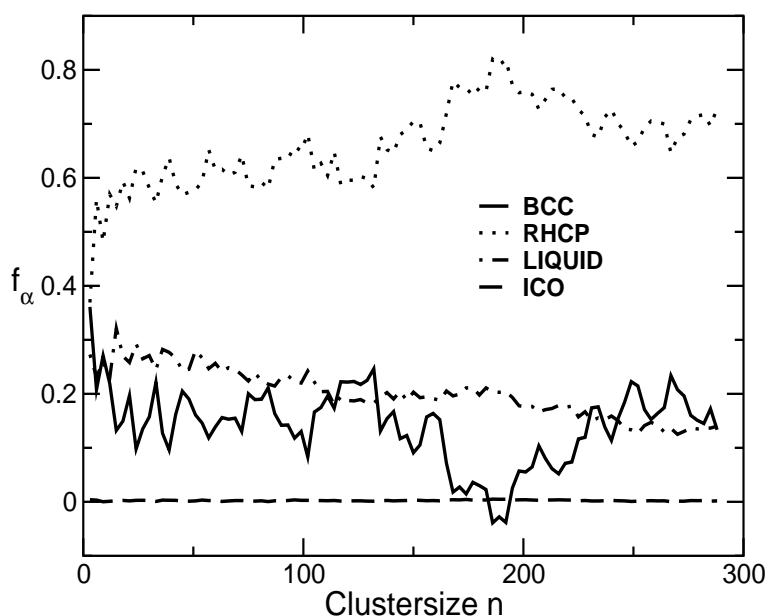
Figure 5.4: Structure analysis of (pre) critical crystal nuclei. The figure shows the relative weight of the structural signatures for rhcp, bcc, icosahedral and liquidlike ordering in hard-sphere crystal nuclei of size n . In order to carry out the structural analysis, we first computed the distribution of bond-order parameters for the various pure structures (see Ref. [25]). This is straightforward for liquid structures. In the case of the randomly-stacked hexagonal close-packed structure, we determined the signature of a randomly stacked bulk crystal. However, no stable bcc or icosahedral structures exist for monodisperse hard spheres. However, we found that we could generate meta-stable bcc structures for slightly (3%) polydisperse hard-sphere crystals. We computed the bcc signature for this structure. In the case of the icosahedral structre, we computed the relevant bond-order parameter distributions for a particle that was constrained to be in an artificially stabilized icosahedral environment of the correct density. The figure shows that bcc and icosahedral structures play no role in the nucleation process. Small clusters are fairly disordered and have an appreciable liquidlike signature. The figure shows that the rhcp signature is dominant for all cluster sizes. However, small crystallites tend to be fairly disordered. In those structures, the bcc and liquidlike signatures become noticeable.

structure is simply more stable than *fcc*. This phenomenon can be interpreted as a manifestation of Ostwald's "step rule" [36]. The hard-sphere fluid nucleates into the *metastable rhcp* structure. Only later does this metastable structure transform into the stable *fcc* structure [42, 43].

5.5   Appendix A: Protocol of the simulation

The barrier was computed using Eq. (5.6). A prerequisite for the calculation of the nucleation barrier is the choice of a "reaction coordinate" that measures the progress from liquid to solid. As our reaction coordinate, we use n, the number of particles that constitute the largest solidlike cluster in the system. A criterion based on the one described in Ref. [25] was used to identify which particles are solidlike (see section 4.1.2. The cutoff for the local environment was set to $r_q = 1.4\sigma$, the threshold for the dot product $q_6q_6 = 20$ and the threshold for the number of connections was set to 6. If two solidlike particles are less than 2σ apart, where σ is the diameter of a particle, then they are counted as belonging to the same cluster. Using this technique we are able to distinguish between particles in a liquidlike environment and particles that belong to

crystalline nuclei. For all but the smallest clusters, $P(n) \ll 1$. We used umbrella sampling [22] to determine $P(n)$ in the range where it is very small. The total simulation was split up into a number of smaller simulations that were restricted to a sequence of narrow, but overlapping, "windows" of n values. It turned out that stacking rearrangements in the crystalline nuclei were slow. To alleviate this problem, we applied the parallel tempering scheme of Geyer and Thompson [23] to exchange clusters between adjacent windows. All simulations were carried out at constant pressure and with the total number of particles (solid plus liquid) fixed. For every window, the simulations took at least 1×10^6 MC moves per particle, excluding equilibration. The results of all simulations are presented in reduced units. In all cases, periodic boundary conditions were imposed. To eliminate noticeable finite-size effects, we simulated systems containing 3375 hard spheres. We also used a combined Verlet and Cell list to speed up the simulations. The kinetic factor was calculated using Eq. (4.51). We performed a kinetic Monte Carlo simulation [26], to measure the size fluctuations of a critical cluster. Kinetic Monte Carlo simulation means in this case a standard Monte Carlo simulation in the limit of very small maximum particle displacements $\Delta x_{max} = 0.01\sigma$. From the barrier calculations we had generated configurations containing a critical cluster, which we used as starting configurations. We run between $5 - 10$ independent trajectories, which was enough to get a reasonable estimate for the attachment rate. More details of the simulations are described in section 4.2.

5.6   Appendix B: Calculation of the chemical potential

Here we describe the calculation of the chemical potential for the monodisperse hard-sphere system. For the system with 5% polydispersity this is described in section 6.5. For the calculation of the chemical potential of the two phases, we performed a thermodynamic integration. The Helmholtz free energy F, per particle and in units of the thermal energy $k_B T$, of a liquid is determined by integrating the equation of state, starting from low densities, where the fluid behaves like an ideal gas [7]:

$$\frac{F(\rho)}{Nk_B T} = \frac{F^{id}(\rho)}{Nk_B T} + \frac{1}{k_B T}\int_0^\rho d\rho' \left(\frac{P(\rho') - \rho' k_B T}{\rho'^2}\right),\tag{5.7}$$

where $P(\rho)$ is the pressure and $F^{id}(\rho)/Nk_B T = \ln(\rho) - 1$ the free energy of an ideal gas at density ρ. The corresponding chemical potential is given by:

$$\frac{\mu(\rho)}{k_B T} = \frac{F(\rho)}{Nk_B T} + \frac{P(\rho)}{\rho k_B T}.\tag{5.8}$$

The calculation of the chemical potential of the solid is slightly more complicated. The reason is that it is not possible to perform the integration from the ideal gas limit, as the solid melts at lower densities. One has to calculate the excess free energy of a solid at a reference density where the solid is stable, which requires a different thermodynamic integration technique, the so called Einstein integration. The idea is to transform the solid reversibly into an Einstein crystal, where the atoms are coupled harmonically to their lattice sites. The free energy can be calculated very precisely and we use the results from Polson et. al. [44] for the excess free energy of a (defect free) hard sphere solid at coexistence: $F^{ex}(\rho_{coex} = 1.0409)/Nk_B T = 5.91889$. From the above equation we can then calculate the chemical potential of the solid at any other density according to:

$$\frac{\mu(\rho)}{k_B T} = \frac{F^{id}(\rho)}{Nk_B T} + 5.91889 + \frac{1}{k_B T}\int_{\rho_{coex}}^\rho d\rho' \left(\frac{P(\rho') - \rho' k_B T}{\rho'^2}\right) + \frac{P(\rho)}{\rho k_B T}.\tag{5.9}$$

For the equation of state $P(\rho)$ we used the analytical expressions by Hall [34] for the liquid and the solid. The integration was performed numerically.

ϕ	$\Delta G(n_{crit})$	n_{crit}	$f^+_{n_{crit}}/D_0$	$\log_{10}[I]$	λ	$\Delta\mu$
0.5207	43.0	260	189	-19.3	0.31	0.34
0.5277	27.8	130	43	-13.5	0.46	0.44
0.5342	18.5	75	66	-9.14	0.27	0.54

Table 5.1: Summary of the simulation results for the calculation of the nucleation rate for monodisperse hard sphere colloids. Here ϕ is the volume fraction of the liquid phase. $\Delta G(n_{crit})$ is the measured free energy to form a cluster of critical size n_{crit}. $f^+_{n_{crit}}/D_0$ is the attachment rate of particles to the critical cluster divided by the free diffusion coefficient. I is the reduced nucleation rate and λ is the estimated typical jump distance from the calculation of the attachment rate. $\Delta\mu$ is the difference in chemical potential between the two phases

5.7 Appendix C: Classical prediction of the kinetic factor

Experimentally determined values for the kinetic factor often differ by orders of magnitude from those predicted by classical nucleation theory (CNT). For this reason it is important to compare our numerical computed kinetic factor with the ones predicted by CNT. The following expression has been proposed in literature [17] (see section 3.1):

$$\kappa_{CNT} = Z\rho_l \frac{24 D_S n_{crit}^{2/3}}{\lambda^2}. \tag{5.10}$$

Here D_S is a self diffusion coefficient in the bulk liquid, ρ_l is the number density of the liquid, n_{crit} is the critical cluster size, λ is a typical atomic jump distance in the liquid and Z is the Zeldovitch factor. In the calculations of the nucleation barrier we saw that the functional form of the nucleation barrier can be fitted accurate to the corresponding analytical expression from CNT. The prediction of the Zeldovitch factor from our numerical calculations and CNT are therefore almost identical. The attachment rate can be identified as $f^+_{CNT} = 24 D_S n_{crit}^{2/3}/\lambda^2$, which we can compare directly to our numerical calculations. If we assume that $D_S = D_S^L$, where D_S^L is the long-time diffusion constant, and treat λ as a fit parameter to reproduce our calculated attachment rates, we get values between $\lambda \approx 0.27 - 0.46\sigma$ (see table 5.1). This is in the order of the inter particle spacing and therefore close to what we would expect for a typical jump distance. In contrast to that, experimental estimates yield values $\lambda = 2.8 - 17\sigma$ [5]. The identification $D_S = D_S^L$ is justified by the fact that the time λ^2/D_S^L corresponds to long-time diffusion.

6

Suppression of crystal nucleation in polydisperse colloids due to increase of the surface free energy

The formation of small crystallites is governed by two competing factors: the free energy gained upon transferring atoms, molecules or colloidal particles from the metastable liquid to the more stable solid, and the free energy needed to create the surface area of the crystallite [17]. Because the ratio of surface area to bulk is large for small particles, small crystallites dissolve spontaneously under conditions where large crystallites are stable and macroscopic crystal growth occurs only if spontaneously formed crystallites exceed a critical minimum size. On theoretical grounds [17], the probability of forming such critical crystal nuclei is generally expected to increase rapidly with supersaturation. However, experiments show [17,45] that the rate of crystal nucleation in many systems goes through a maximum as the supersaturation is increased. It is commonly assumed that the nucleation rate peaks because, even though the probability to form critical nuclei increases with increasing concentration, the rate of growth of such nuclei decreases. Here, we report simulations of crystal nucleation in suspensions of colloidal spheres with varying size distributions. Surprisingly, our simulations show that the probability to form critical nuclei itself goes through a maximum as the supersaturation is increased. This effect is strongest for systems with the broadest size distribution. It is due to the increase with supersaturation of the solid-liquid interfacial free energy. The magnitude of this effect suggests that vitrification at high supersaturation should yield colloidal glasses that are truly amorphous, rather than nano-crystalline.

6.1   Introduction

Colloidal suspensions of identical, hard, spherical particles can be either fluid or crystalline. At low densities, the fluid state is stable, but when the colloids occupy more than 49.4% of the volume, a crystalline phase should form [45]. In practice, several factors influence the crystallization of hard-sphere colloids. First of all, synthetic colloids have a distribution of particle radii with a width that is rarely less than $2 - 3\%$ of the average radius. This non-uniformity of size ("polydispersity") is known to affect the location of the freezing curve. Simulations [46,47] show that higher compressions are needed to freeze a polydisperse suspension. Irrespective of the composition of the coexisting fluid, the polydispersity of the crystal never exceeds 5.7%. Experiments on crystal formation in hard-sphere colloids indicate that crystallization is suppressed in suspensions with a polydispersity exceeding 12% [45]. This must be due to kinetic

factors, as crystallization of strongly polydisperse suspensions is not excluded on thermodynamic grounds.

Classical Nucleation Theory (CNT) [17] offers a simple thermodynamic explanation why small crystal nuclei are less stable (i.e. have a higher free energy) than the supersaturated parent phase. CNT uses macroscopic arguments to estimate the free energy required to form a crystallite. The decrease in free energy due to the transfer of n particles from the metastable liquid to the solid state, is approximated as $n\Delta\mu$, where $\Delta\mu = \mu_{solid} - \mu_{liquid}$ is the difference in chemical potential between the solid and the liquid state. The CNT estimate for the free-energy cost involved in the creation of the surface area A of the nucleus is γA, where γ is the surface free energy of the solid-liquid interface.

Due to the competition between bulk and surface terms, the Gibbs free energy $\Delta G(n)$ required to form an n-particle nucleus goes through a maximum at a value of n called the critical nucleus size. For a spherical nucleus, the maximum value of $\Delta G(n)$ is

$$\Delta G^*(n_{crit}) = \frac{16\pi}{3}\gamma^3/(\rho|\Delta\mu|^2) \tag{6.1}$$

where ρ is the number density of the crystal phase. The rate I at which nuclei are formed depends exponentially on $\Delta G^*(n_{crit})$:

$$I = \kappa \exp(-\Delta G^*(n_{crit})/k_B T) \tag{6.2}$$

where T is the absolute temperature, k_B is Boltzmann's constant and κ is a kinetic prefactor that is proportional to the short-time self-diffusion constant of the colloids. The form of Eq. (6.2) does not rely on the validity of CNT.

In the CNT picture, increasing the supersaturation (i.e. increasing $|\Delta\mu|$), lowers the nucleation barrier. If γ were independent of $|\Delta\mu|$, then ΔG^* would always decrease with increasing supersaturation. In experiments [3,5,28] the rate of colloidal crystal nucleation starts to decrease again for large supersaturations. This effect is attributed to the decrease in the kinetic prefactor κ: in order to crystallize, colloidal fluids must be compressed beyond the freezing curve. But eventually, the suspension will vitrify under compression. This vitrification slows down the particle motion and presumably reduces κ in Eq. (6.2). A problem with this interpretation is that recent experiments on colloidal crystallization in micro-gravity have found evidence for crystallization at densities that are well beyond the glass-transition point [31].

6.2   Crystal barrier calculation

We performed Monte Carlo simulations to study the crystal-nucleation barrier and the structure of the critical nucleus, as a function of both polydispersity and supersaturation. As in the case of monodisperse suspensions [48], we find that all critical nuclei have a randomly-stacked close-packed structure. During crystallization, size-fractionation occurs [46, 47]: the particles that make up the critical nucleus are on average larger than those in the metastable liquid, see also Appendix 6.6. We find that ΔG^*, the height of the nucleation barrier, at fixed $|\Delta\mu|$, does not depend on the polydispersity for polydispersities $\leq 5\%$ (see Fig. 6.1). As the polydispersity is increased beyond 5%, ΔG^* increases rapidly. This implies that the probability to form a critical nucleus, is suppressed in polydisperse suspensions. It follows from Eq. (6.1) (or actually, from its polydisperse equivalent, see section 3.2.1) that, at constant $|\Delta\mu|$, the variation of ΔG^* with polydispersity is due to an increase of the interfacial free energy γ. The increase of γ with polydispersity runs counter to Turnbull's suggestion that the interfacial free energy should be proportional to ΔH, the latent heat of fusion [17]. For the systems that we studied, ΔH crosses
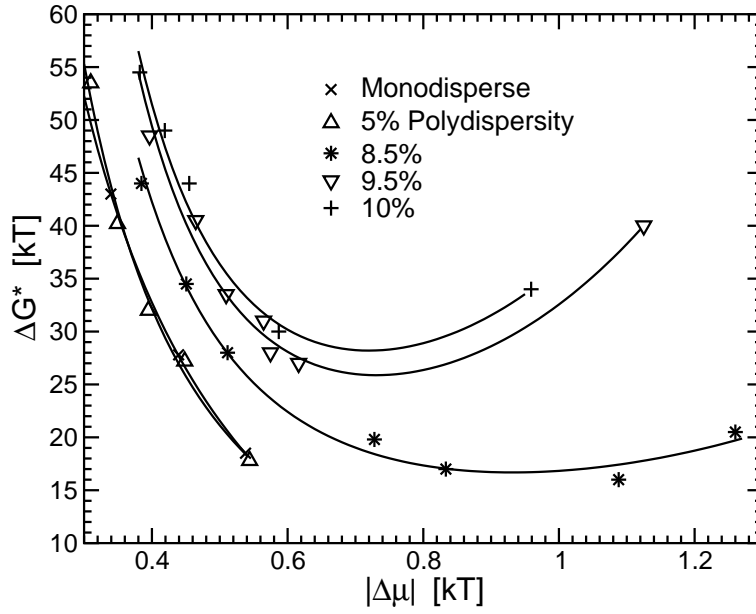
Figure 6.1: Computed dependence of the free-energy barrier for crystal nucleation of polydisperse suspensions of hard, colloidal spheres. The free energy is expressed in terms of k_BT, where k_B is Boltzmann's constant and T is the absolute temperature. $|\Delta\mu|$ (also in units of k_BT) is the absolute difference between the chemical potential of the liquid and the solid. It is a measure for the degree of supersaturation. The curves are fits that have been drawn as a guide to the eye. To facilitate comparison with experiment, we have collected in Table 6.1, the relation between $|\Delta\mu|$ and the volume fraction ϕ of the liquid, for the different systems that we studied.

zero at a polydispersity of 9%, where the liquid becomes denser than the coexisting solid [46,47]. Yet, γ clearly remains non-zero, see Appendix 6.7.

Surprisingly, the variation of ΔG^* with $|\Delta\mu|$ is non-monotonic. As $|\Delta\mu|$ is increased, the nucleation barrier goes through a minimum (Fig. 6.1). This non-monotonic behavior of $\Delta G*$ is due to the increase of γ with $|\Delta\mu|$ (Fig. 6.2). To illustrate this, let us approximate the $|\Delta\mu|$-dependence of γ by $\gamma \approx \gamma_0(1 + a|\Delta\mu|)$. Ignoring the slight $|\Delta\mu|$-dependence of the solid density, it then follows from Eq. (6.1) that ΔG^* must go through a minimum when $|\Delta\mu| = 2/a$. The nucleation theorem [49] suggests that the minimum in ΔG^* is due to the inversion of the densities of the polydisperse fluid and the crystal nucleus, see Appendix 6.8. In CNT it is usually assumed that γ is constant. A linear variation of γ with $|\Delta\mu|$ has been observed in inorganic glasses [17], but there the constant a is negative and hence there is no minimum in ΔG^*. In other systems [50,51], non-monotonic behavior of ΔG^* is induced by a hidden phase transition in the meta-stable phase.

The minimum value of ΔG^* increases rapidly with polydispersity. Using kinetic Monte Carlo simulations, we can estimate the value of the kinetic prefactor [26]. We find that, over the range of supersaturations studied, the kinetic prefactors vary by at most an order of magnitude, see Appendix 6.9. This means that the variation in the rate of nucleation is dominated by the behavior of ΔG^*. We estimate that, for colloidal particles with a radius ≥ 500 nm, homogeneous nucleation will be effectively suppressed (less than one nucleus per cm^3 per day) when the polydispersity exceeds 10%. This finding has important implications for the morphology of polycrystalline colloidal materials. Using a simplified version of the analysis proposed by Shi et al. [50] to estimate the size of crystallites in a polycrystalline sample, it is easy to derive that Rc, the average crystallite size at the end of a nucleation experiment, should scale as
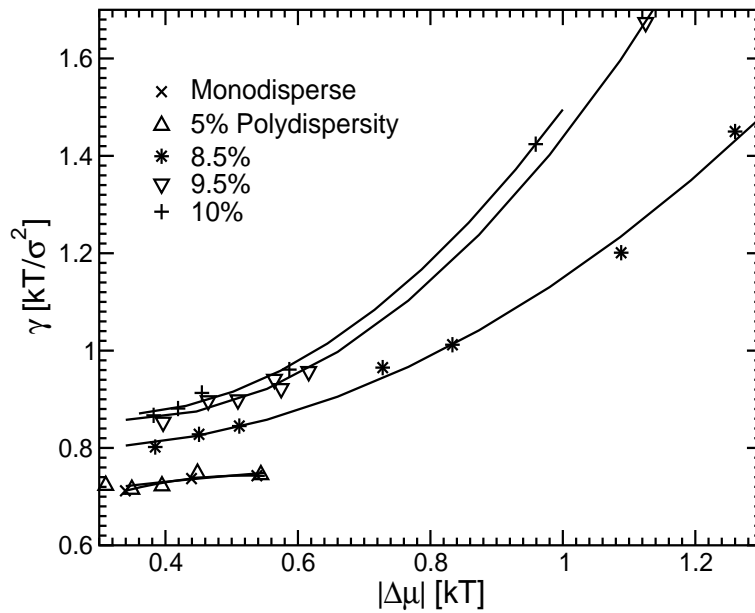
Figure 6.2: Dependence of the interfacial free energy γ of crystal nuclei in polydisperse suspensions of hard, colloidal spheres. The interfacial free energy is expressed in terms of $k_B T/\sigma^2$, where σ is the average hard-sphere diameter. The curves are fits that have been drawn as a guide to the eye.

$\exp(\Delta G^*/4 k_B T)$, Appendix 6.10. Our observation of a minimum in ΔG^* thus implies the existence of a minimum in the typical crystallite size. This should be experimentally observable.

We could only compute ΔG^* if spontaneous nucleation did not occur in the course of a simulation. In practice, this implied that we could not study barriers lower than $15 k_B T$. As a result, we could not test whether ΔG^* in systems with a low polydispersity (less than 8.5%) also has a minimum. If we assume that, also at lower polydispersities, we can extrapolate the increase of γ with $|\Delta\mu|$ to large supersaturations, then we predict that a minimum in ΔG^* should occur even in nearly monodisperse systems. Again, this should be experimentally observable, because we should expect to see the formation of larger crystallites if the solution can be compressed rapidly through the region where ΔG^* is small.

6.3   Conclusions

There are two ways to interpret the experimental finding that crystallization is not observed in suspensions with a polydispersity $> 12\%$: either crystals do not form, or they are too small to be observed. Our simulations support the first interpretation. Using Shi's approach, we can estimate the maximum number of crystallites per unit volume [50]. For a suspension of colloids with a 500 nm radius, we expect to see less than one crystallite per cubic centimeter, once $\Delta G^* > 32 k_B T$. In other words, under those conditions the colloidal glass is truly amorphous.

Our predictions concerning the structure and free energy of colloidal crystal nuclei can be tested experimentally. Recently, the technique of Confocal Scanning Laser Microscopy has been applied by Gasser et al. [52] to study the structure and size of critical crystal nuclei in dense colloidal suspensions. This technique would be perfectly suited to test our predictions. Our prediction concerning the minimum in ΔG^* is even easier to verify. By visual inspection, one could verify whether the crystallites that nucleate in strongly supersaturated solutions are larger than those that form at lower supersaturations. Over a decade ago, Pusey and van Megen published

0%		5%		8.5%		9.5%		10%	
$\Delta\mu$	ϕ	$\Delta\mu$	ϕ	$\Delta\mu$	ϕ	$\Delta\mu$	ϕ	$\Delta\mu$	ϕ
0.339	0.5207	0.310	0.5344	0.385	0.5614	0.397	0.5697	0.382	0.5717
0.439	0.5277	0.349	0.5377	0.451	0.5673	0.465	0.5746	0.419	0.5738
0.538	0.5342	0.395	0.5414	0.512	0.5726	0.509	0.5782	0.455	0.5775
		0.448	0.5456	0.728	0.5864	0.565	0.5808	0.587	0.5878
		0.544	0.5528	0.833	0.5948	0.575	0.5828	0.959	0.6239
				1.088	0.6145	0.616	0.5859		
				1.260	0.6212	1.125	0.6239		

Table 6.1: Supersaturation and volume fraction of polydisperse colloids. $\Delta\mu$ is the supersaturation and ϕ is the volume fraction of the colloidal fluid. The polydispersity ranges from 0% (left) to 10% (right). The polydispersities quoted in this table and in the figures, are those of the metastable liquid.

beautiful images of the morphology of poly-crystalline hard-sphere colloids [53] (Similar morphologies have recently been observed in a study of colloidal crystallization in micro-gravity - Z.D. Cheng, W.B. Russel and P.M. Chaikin, unpublished data). Pusey and van Megen observed an increase of the crystallite size at large supersaturations. However, they attributed this effect to heterogeneous nucleation. Hence, a direct test of our prediction is still lacking.

6.4   Appendix A: Protocol of the simulation

The simulation techniques that are required to compute the free energy of small crystal nuclei, have been described in section 4.1. In the present work, we used constant-pressure, semi-grand canonical Monte Carlo (SGMC) simulations of the type described in [46, 47]. In such a simulation it is not possible to impose the size distribution of the particles directly, but the size distribution can be controlled through variation of the imposed activity-ratio distribution function $\exp[\beta\mu(\sigma) - \mu(\sigma_0)]$. Here $\mu(\sigma)$ is the chemical potential related to a particle with diameter σ. For all simulations, but the two with the highest supersaturation at 10% polydispersity, we used for the chemical potential difference function:

$$\beta[\mu(\sigma) - \mu(\sigma_0)] = -(\sigma - \sigma_0)^2/2\nu, \tag{6.3}$$

which gives rise to a Gaussian activity distribution that peaks at $\sigma = \sigma_0$, with width ν. In the limit $\nu \to 0$ the monodisperse phase is recovered. For high supersaturations and polydispersities we needed to include terms up to cubic in the sphere diameter:

$$\Delta\mu(\sigma) = c_1\sigma + c_2\sigma^2 + c_3\sigma^3. \tag{6.4}$$

This cubic form was need to maintain the desired size distribution under these conditions. It is important to mention that at the relatively low polydispersities ($\leq 10\%$) needed in our simulations, we do not expect that the crystal nucleation barrier is very sensitive to the details of the size distribution. For higher polydispersities ($> 5\%$), the resulting size distribution is a function of the density. For this reason it was necessary to map the variation of the polydispersity with ρ and ν to find a proper parameter set $(\nu, \beta P \langle \sigma_0^3 \rangle)$, with $\beta = 1/k_B T$, at which we could perform our barrier calculations. In table 6.2 we give a summary of the parameter set $\nu, \beta P \langle \sigma_0^3 \rangle$ used in our simulations. Note, that in order to get physically meaningful values for the pressures, it is necessary to scale P^* with for $< \sigma^3 >$, where σ is for example the average diameter of the particles in the liquid. For more details of the simulation method and the scaling see [46, 47].

0%		5%		8.5%		9.5%		10%	
P^*	ν	P^*	ν	P^*	ν	P^*	ν	P^*	ν
15	0	24.6	0.0023	174	0.0044	1147	0.0032	7920	0.002
16	0	25.7	0.0023	227	0.0042	1823	0.00288	12900	0.0017
17	0	27	0.0023	293	0.0039	2990	0.0025	74000	0.001
		28.6	0.0023	600	0.0032	4000	0.0023	$\tilde{P}$	c_3
		31.7	0.0023	940	0.00288	6210	0.002	8.5×10^{-5}	1×10^{-6}
				3045	0.002	10095	0.0017	6.8×10^{-5}	5×10^{-6}
				4215	0.0017	2183190	0.000276199		

Table 6.2: Collection of parameter sets (ν, P^*) used in the simulations. ν is the width of the imposed particle size distribution function and $P^* = \beta P \langle \sigma_0^3 \rangle$ the pressure. Here $\tilde{P} = P^*(\nu/\sigma_0)^3$ is a rescaled pressure. In the infinite pressure limit ($P^* \to \infty, \nu \to 0$) $\tilde{P} = 0.000151765$. This corresponds to an activity distribution where $c_1 = 1$ and $c_2 = c_3 = 0$, see Eq. (6.4). The polydispersity ranges from 0% (left) to 10% (right). The polydispersities quoted in this table and in the figures, are those of the metastable liquid.

To identify solid-like particles in our simulations, we used the same criterion as in the case for monodisperse hard spheres (see section 4.1.2). The only adjustment we had to make is due to the different sizes of the particles. The local environment was defined as the surface to surface distance between particles. All particles where this distance is smaller than $0.4 \times \langle \sigma \rangle$, where $\langle \sigma \rangle$ is the average diameter of all particles, are considered to be neighbors. The threshold for the dot product $q_6 q_6 = 20$ and the threshold for the number of connections was set to 7, as in the monodisperse hard-sphere case. Two solid like particles were considered to be belong to the same cluster if their surface to surface distance was less than $0.8 \times \langle \sigma \rangle$. To eliminate possible finite-size effects, we used systems of 3375 particles. Very long runs, up to 1.6×10^7 trial moves per particle, in combination with parallel tempering [23], were needed to ensure equilibration of the dense, polydisperse fluid.

6.5   Appendix B: Calculation of the chemical potential

The calculation of the chemical potential of the liquid and the solid phases is described in section 5.6. This time we did only calculate the chemical potential difference between the two phases. The coexistence pressure and density has been calculated [46, 47]. We used this data and performed a thermodynamic integration starting at coexistence, where the chemical potential difference is zero:

$$\frac{\Delta\mu(P)}{k_B T} = \frac{1}{k_B T} \int_{\rho_{s,coex}}^{\rho_s} d\rho_s' \left(\frac{P(\rho_s') - \rho_s' k_B T}{\rho_s'^2} \right) + \frac{P(\rho_s)}{\rho_s k_B T} - \frac{P(\rho_{s,coex})}{\rho_{s,coex} k_B T} + \log(\rho_s) - \log(\rho_{s,coex})$$
$$- \left\{ \frac{1}{k_B T} \int_{\rho_{l,coex}}^{\rho_l} d\rho_l' \left(\frac{P(\rho_l') - \rho_l' k_B T}{\rho_l'^2} \right) + \frac{P(\rho_l)}{\rho_l k_B T} - \frac{P(\rho_{l,coex})}{\rho_{l,coex} k_B T} + \log(\rho_l) - \log(\rho_{l,coex}) \right\}.$$

Here $\Delta\mu(P) = \mu_s(P) - \mu_l(P)$ and ρ_l, ρ_s are the number densities of the liquid and the solid. The index *coex* indicates the coexistence data. The equation of state $P(\rho)$ we measured in a constant-pressure, SGMC simulation and performed the integration numerically. A summary of the coexistence pressure we used from Ref. [46, 47] is given in table 6.3. Our results for the chemical potential difference are given in table 6.1.

0%		5%		8.5%		9.5%		10%	
P^*_{coex}	ν	P^*_{coex}	ν	P^*_{coex}	ν	P^*_{coex}	ν	P^*_{coex}	ν
11.7	0	17.3	0.0023	665	0.0044	2321	0.0032	13365	0.002
11.7	0	17.3	0.0023	854	0.0042	3827	0.00288	22026	0.0017
11.7	0	17.3	0.0023	1096	0.0039	6310	0.0025	126754	0.001
		17.3	0.0023	2321	0.0032	8547	0.0023	P	c_3
		17.3	0.0023	3827	0.00288	13365	0.002	1.54469×10^{-4}	1×10^{-6}
				13365	0.002	22026	0.0017	1.65185×10^{-4}	5×10^{-6}
				22026	0.0017	6920522	0.000276199		

Table 6.3: Notation as in caption of Tab. 6.2, but we give the coexistence pressure.

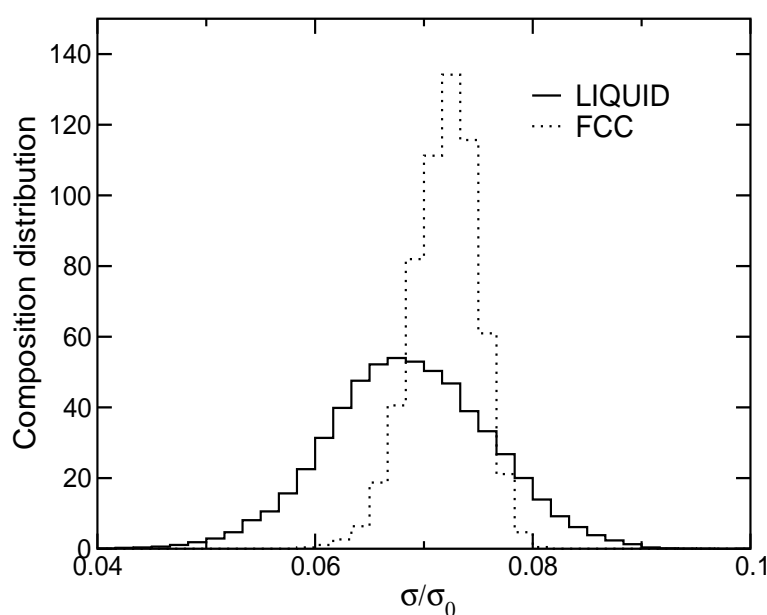## 6.6   Appendix C: Size fractionation and polydispersity

Figure 6.3: Particle size distribution for the liquid and the solid at a pressure of $\beta P \langle \sigma_0 \rangle = 74000$ and $\nu = 0.001$. At such high pressures the average size of the particles and the simulation box is compressed to small values. However, note that this does not affect the distribution function itself.

In our simulations we imposed the same chemical potential difference function on the bulk liquid and the solid phase. This results in different diameter distribution functions, which is shown in Fig 6.3 for our simulations at pressure $\beta P \langle \sigma_0 \rangle = 74000$ and $\nu = 0.001$. On average the size of particles in the bulk solid is larger than that of the corresponding bulk liquid, whereas the polydispersity is smaller. When a crystal nucleus forms in a supersaturated liquid, this behavior is reflected, see Fig. 6.4. The size and polydispersity of the particles close to the center of the crystal nucleus are that of the bulk solid. For larger distances the bulk values of the liquid are approached.
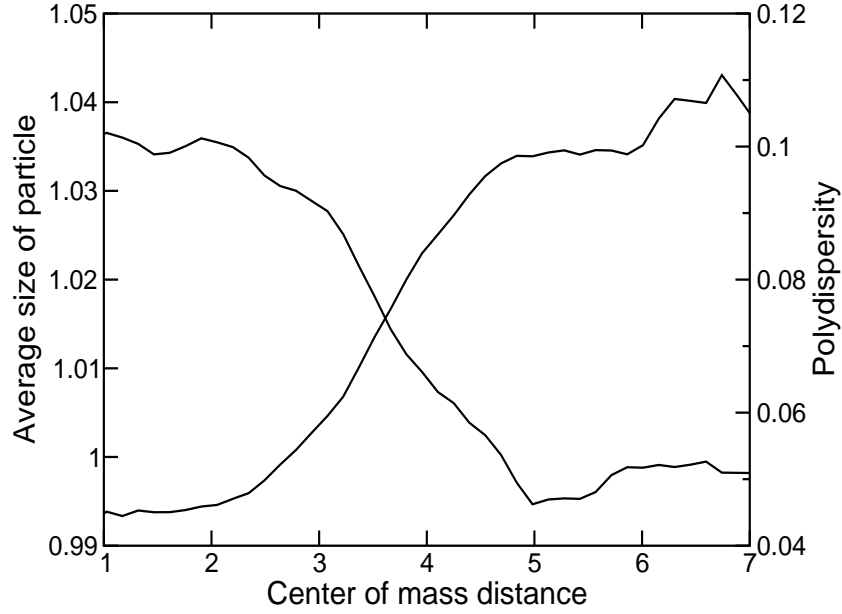
Figure 6.4: Average size and polydispersity of particles as a function of the center of mass of the cluster in units of the average diameter of particles in the bulk liquid. Fractionation in particle size and polydispersity occurs. The particles in the crystal nucleus are in average larger as the particles in the bulk liquid, while they are less polydisperse.

6.7   Appendix D: Turnbull's rule

Turnbull suggested that, as the (crystal-vacuum) interfacial free energy is related to the heat of sublimation in molecular crystals, there should be a relation between the liquid-crystal surface free energy and the heat of fusion Δh [2]. From crystal nucleation experiments in metallic liquids a linear dependence was obtained. We could test if this relation holds for a system of polydisperse hard-sphere colloids. From our barrier calculations we had estimates for the liquid-crystal surface free energy. The enthalphy difference we computed according to:

$$\Delta h = P^* \left(\frac{1}{\rho_s} - \frac{1}{\rho_l} \right) \tag{6.5}$$

where $P^* = \beta P \langle \sigma_0^3 \rangle$ and ρ_l, ρ_s are the number densities of the bulk liquid and solid. In Fig. 6.5 we plot the liquid-crystal surface free energy as a function of the enthalphy difference. As can be seen, in this case we do not find this linear dependence.

6.8   Appendix E: Nucleation theorem

The nucleation theorem relates the change of the nucleation barrier height ΔG^* with the chemical potential difference $\Delta \mu$ between the metastable liquid and the stable solid phase to the excess number of particles in the critical nucleus [49]:

$$\frac{\partial \Delta G^*}{\partial \Delta \mu} = -\Delta n^*, \tag{6.6}$$

where the excess number of particles is given by

$$\Delta n^* = 4\pi \int_0^\infty dr r^2 \left[\rho(r) - \rho_l \right]. \tag{6.7}$$
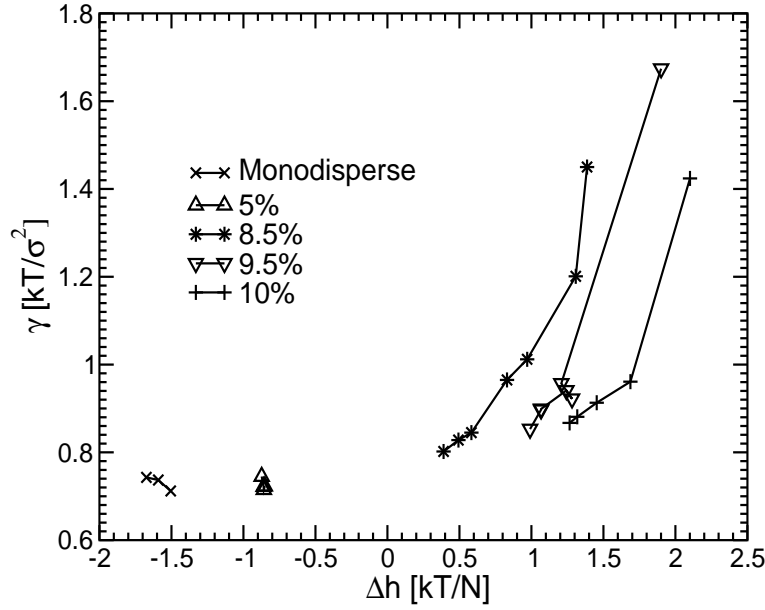
Figure 6.5: Surface free energy γ as a function of the enthalpy difference Δh (per particle) between the liquid and the crystal phase shown for the different polydispersities.

Here $\rho(r)$ is the density in the system as a function of the distance from the center of mass of the critical nucleus and ρ_l is the density of the liquid. Note that in our case the supersaturation $\Delta\mu$ is the same for all particle sizes and the above equation can be applied directly to the polydisperse system. D. Oxtoby suggested [54] that if ΔG^* passes through a minimum the excess number of particles of the nucleus must become lower than that of the surrounding liquid. To test this prediction we compared the number density of the bulk liquid at pressure P, where we performed our crystal barrier calculations, with the number density of a bulk solid at a pressure $P + \Delta P$, where ΔP is the Laplace pressure. The pressure inside a crystal nucleus is slightly higher than that of the surrounding liquid to compensate the chemical potentials. The calculation of the Laplace pressure in a polydisperse system is described in section 3.2.1. In Fig. 6.6 we plot the ratio of the number densities of the liquid and the solid as a function of the difference in the chemical potential between the two phases. As can be seen, indeed we observe a inversion of the number densities for the systems with 9.5% and 10% polydispersity. For the system with 8.5% polydispersity the situation is less clear. Note that at the minimum the number density of the solid becomes higher than that of the liquid and not vice verse. This is the opposite of what we expected. The reason is probably due to the fact that at these polydispersities and densities the number density of the liquid at coexistence is already higher than that of the solid. But when the system is compressed to higher densities at constant poydispersity of the liquid, the solid becomes more and more monodisperse. This means that the number density of the solid increases.

6.9 Appendix F: Kinetic factor

We computed the reduced attachment rate of particles to the critical cluster by using the kinetic Monte Carlo scheme described in section 4.2. We should note that the calculated attachment rates do not differ considerably (less than one order of magnitude) from the results in the monodisperse case, see table 6.4. Considering the high volume fractions at which our simulations were performed, this is not obvious. Although diffusion is probably slowed down
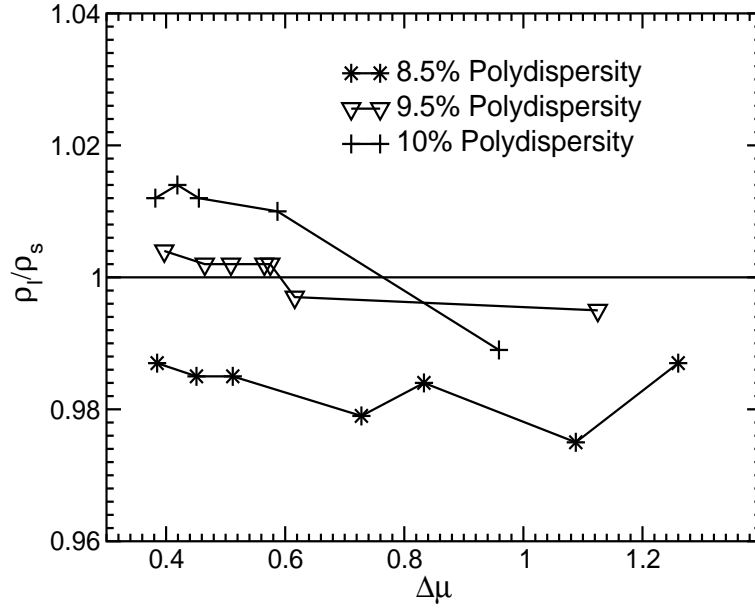
Figure 6.6: Ratio of the number densities ρ_l, ρ_s of the bulk liquid and solid phases. The number density of the liquid was computed at a pressure P, while that of the solid was calculated at slightly higher pressure $P + \Delta P$, where ΔP is the Laplace pressure.

dramatically at such high volume fractions and polydispersities, we did not try to correct for it. The main reason is that it is not straightforward to apply the idea from Medina-Noyola [27] to a polydisperse system and there are only a few experimental measurements on the long-time self-diffusion coefficient, to which we could test this approach. However, considering the fact that the attachment of particles to the critical cluster does still happen, and that for crystallization only diffusion on the scale of the short-time self-diffusion coefficient is needed, we can argue that the variation of the nucleation rate is dominated by the behavior of the nucleation barrier. In general it is save to say that the decrease of the nucleation rate at high densities is a competition between a slowing down of the kinetics and a decreasing probability for the formation of a critical cluster due to an increase in surface free energy.

6.10 Appendix G: Average size of a crystallite

To estimate the average crystallite size at the end of a crystallization experiment, we use a simplified version of the analysis proposed by Shi et al. [50]. We assume that I, the rate of steady-state nucleation, is given by Eq. (6.2), and that v_g, the rate at which the crystallite radius grows, is given by the Wilson-Frenkel law:

$$v_g = \frac{D_S}{\lambda}[1 - \exp(-|\Delta\mu|/k_B T)], \tag{6.8}$$

where λ is a typical atomic jump distance and D_S a self-diffusion constant. Note that both I and v_g are proportional to D_S. The total volume fraction occupied by crystallites as a function of time t is approximately given by the Avrami growth law

$$\phi \approx I\pi v_g t^4/3. \tag{6.9}$$

Crystallization stops when ϕ is of order 1. This happens after a time $t_{max} \sim (Iv_g^3)^{-1/4}$. The average crystallite radius at this time is equal to $R_c \approx v_g t_{max}$. Using the expression for t_{max}

8.5%		9.5%		10%	
$f^+_{n_{crit}}/D_0$	ν	$f^+_{n_{crit}}/D_0$	ν	$f^+_{n_{crit}}/D_0$	ν
40	0.0044	12	0.0032	20	0.002
75	0.0042	60	0.00288	55	0.0017
21	0.0039	15	0.0025	40	0.001
30	0.0032	50	0.0023		c_3
15	0.00288	10	0.002	10	1×10^{-6}
35	0.002	20	0.0017	8	5×10^{-6}
10	0.0017	5	0.000276199		

Table 6.4: Notation as in caption of Tab. 6.2, but we give the reduced attachment rate $f^+_{n_{crit}}/D_0$.

above, it follows that $R_c \sim (\nu_g/I)^{1/4}$.

The crucial point to note is that the average crystallite size depends only on the ratio ν_g/I. As the strongly density dependent diffusion constant D_S drops out of this ratio, its $|\Delta\mu|$-dependence is mainly determined by the variation of $\exp(\Delta G^*/k_B T)$, except for small supersaturations. We therefore expect that the typical crystallite size at the end of a nucleation experiment should scale as $R_c \sim \exp(\Delta G^*/4k_B T)$. Our prediction of a maximum in the nucleation barrier then translates into the prediction of a minimum in the typical crystallite size.

7

Crystallization of weakly charged colloidal spheres: A numerical study

We report a numerical study of crystal nucleation in a system of weakly charged colloids. The interaction between the colloids is approximated by a repulsive hard-core Yukawa potential. We studied the dependence of the nucleation barrier and the nucleation rate on supersaturation as a function of both contact value and range of the interaction potential. We find that, at the same volume fraction, nucleation is much faster for these soft colloids than for hard spheres. This is partly because fluid-solid coexistence in charged colloids occurs at lower volume fractions than for hard spheres. But, in addition, the softness of the potential has a pronounced direct effect on the nucleation barrier through a lowering of the solid-liquid surface free energy. Moreover, the softness of the potential directly affects the pathway for crystal nucleation: even when the stable crystal phase has a face-centered cubic structure, we find that the initial crystal nuclei have a bcc structure.

7.1 Introduction

When a suspension of monodisperse colloids is brought to a sufficiently high density, it will form beautiful, iridescent crystals. The rate at which these crystals form depends strongly on the steepness of the repulsive forces that act between the colloids. While it is difficult to compare absolute nucleation rates in different colloidal systems under differing conditions, experiments [55,56] clearly indicate that charged colloids with a soft, long-ranged repulsion, tend to crystallize much faster than hard-sphere colloids at the same supersaturation. The aim of the present paper is to elucidate the factors that affect the rate of crystal nucleation in a system of weakly charged colloids.

In suspension, the charged colloids are surrounded by a cloud of counterions. This counterion double layer screens the pure Coulomb interaction between the colloids. If we use the linearized Poisson-Boltzmann equation to describe the charge distribution around a charged colloid with hard-core diameter σ, then we obtain the following expression for the pair interaction between two charged macro-ions:

$$\beta U(r) = \begin{cases} \infty & \text{for } r < \sigma \\ \beta \epsilon \frac{\exp(-\kappa(r/\sigma - 1))}{r/\sigma} & \text{for } r > \sigma. \end{cases} \qquad (7.1)$$

$U(r)$ is usually referred to as the "hard-core Yukawa potential", see Fig. 7.1. Here κ is the inverse screening length in units of the hard-sphere diameter σ and $\beta \epsilon$ is the value of the Yukawa
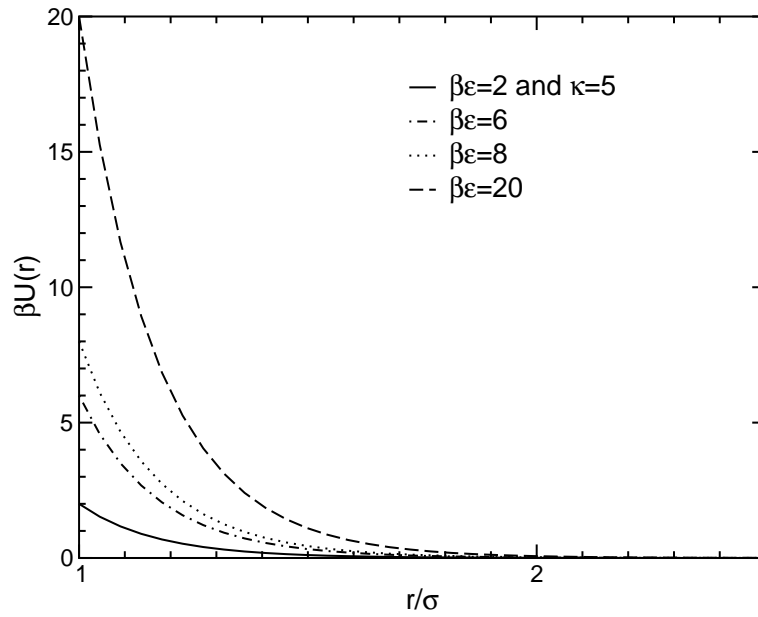
Figure 7.1: Plot of the hard-core Yukawa potential for $\kappa = 5$ as function of the Yukawa repulsion $\beta\epsilon = 2, 6, 8, 20$.

repulsion at contact. β is a measure for the inverse temperature ($\beta = 1/k_B T$), where k_B is the Boltzmann constant. In the linearized Poisson-Boltzmann theory, we have explicit expressions for both κ and ϵ in terms of the size and surface charge of the colloid, and of the concentration of counterions and added salt. However, the linearized Poisson-Boltzmann description provides only an approximation to the real colloid-colloid interaction. For instance, it is expected to break down at short distances and for low added salt concentrations. A way to treat the interaction between charged colloids at short distances was already proposed by Derjaguin, Landau, Verweij and Overbeek (DLVO) in the 1940's [57]. Since then, several modifications of the form of the pair potential between charged colloids have been proposed [58, 59] but, except at very short distances, most expression are very similar to the hard-core Yukawa model. The main difference between the theories is the values that they yield for κ and ϵ. In the original DLVO theory, these parameters depend only on the ionic strength of the solution and on the bare charge of the colloids. In the more recent theories, κ and ϵ may themselves depend on the concentration of charged colloids. In the present work, we simply assume that the interaction between charged colloids is adequately described by a hard-core Yukawa potential. However, we shall return later to the question whether this is allowed. A special case of the hard-core Yukawa model, is the hard-sphere model. The latter model applies in the limit of high salt concentrations $\kappa \to \infty$ and in the limit that the strength of the repulsion is much less than the thermal energy, i.e. $\beta\epsilon \to 0$. This is typically the case for weakly charged colloids. We note that, whilst the hard-core Yukawa model is commonly used to describe slightly charged colloids, it can also be used as a crude model for sterically stabilized colloids. Hence, many of the conclusions that we obtain below, in particular those for systems with a high value of κ, should equally apply to sterically stabilized, uncharged colloids.

The phase behavior of the hard-core Yukawa potential has been calculated in detail by numerical simulation [60]. In these calculations the parameters κ and $\beta\epsilon$ were varied independently. This cannot easily be done in experiments as a variation in κ will change ϵ, unless some other parameter, such as the charge of the colloid, is varied at the same time. The computed phase diagram of ref. [60] shows a fluid-solid (bcc/fcc) and a solid-solid (bcc-fcc) coexistence
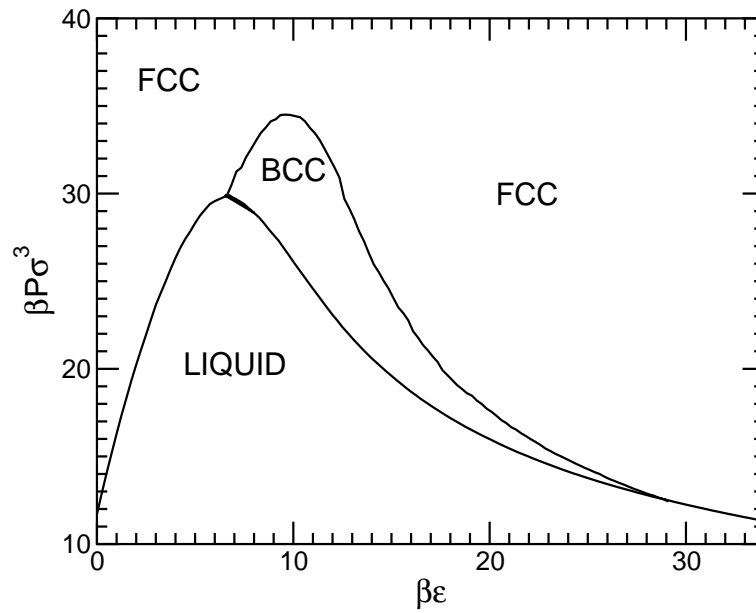
Figure 7.2: Calculated coexistence pressure from ref. [60] for $\kappa = 5$ as function of the Yukawa repulsion $\beta\epsilon$.

line and it exhibits two fluid-bcc-fcc triple points (see Fig.7.2). The main difference between the phase diagram of the hard-core Yukawa model and that of the pure (i.e. point-particle) Yukawa potential [61] is the presence of the second triple point. This triple point sets a lower limit for the strength of the Yukawa interaction for which a bcc phase exists.

Extensive crystallization experiments have been performed on systems of uncharged, hard-sphere colloids using time resolved laser light scattering or microscopy [3–5, 29, 30, 35, 62]. For charged colloidal systems, there are fewer studies of this kind [55, 63–65]. More recently, Gasser et al. [52] published a confocal microscopy study of homogeneous crystal nucleation in slightly charged hard-sphere colloids. In addition, an extensive light-scattering study of crystallization in more highly charged colloids has been performed by Schöpe [56, 66, 67].

In the present paper, we report a computer-simulation study of crystal nucleation in a hard-core Yukawa system. In these simulations, we have varied both the amplitude of the Yukawa repulsion and the magnitude of screening length and studied the effect of both parameters on crystal nucleation.

7.2 Homogeneous nucleation

Crystal nucleation is an activated process. This implies that it costs free energy to form small crystal nuclei in the supersaturated liquid. However, once a nucleus exceeds a critical size, its free energy will decrease as further growth of the crystal takes place. Classical nucleation theory (CNT) provides a simple, thermodynamic description of the free energy of a crystal nucleus. In CNT theory the free energy of a nucleus contains two terms, a bulk- and a surface term. The bulk term takes care of the fact that the chemical potential of the solid phase is lower than that of the liquid phase. The gain in free energy if N particles transform from the liquid to the solid phase is $N\Delta\mu$, where $\Delta\mu = \mu_{liq} - \mu_{sol}$ is the difference in chemical potential between the liquid and the solid phase. The surface term, $A\gamma$, describes the free energy required to create a liquid/solid interface of area A, where γ is the interfacial free energy per unit area. For small nuclei the surface term dominates and the free energy of the nucleus increases as it grows. When

the nucleus is at its critical size n_{crit} the function goes through a maximum:

$$\Delta G^* = \frac{16\pi}{3}\gamma^3/(\rho_s|\Delta\mu|)^2, \tag{7.2}$$

where ρ_s is the number density of the solid phase. For larger nuclei, the free energy goes down again because it is dominated by the (negative) bulk term $-\Delta\mu$. The steady-state nucleation rate per unit volume, I, is the product of the probability that a critical nucleus is formed $P_{crit} = \exp[-\beta\Delta G^*]$, times a kinetic factor Γ which describes the rate with which a critical nucleus growths:

$$I = \Gamma\exp[-\beta\Delta G^*]. \tag{7.3}$$

In order to be able to compare our results with experiments, we express the crystallization rates in dimensionless form: $I^* \equiv I\sigma^5/D_0$, where D_0 is the self diffusion coefficient at infinite dilution. Such an expression for the reduced rate follows logically if all distances are expressed in units σ and time is expressed in units σ^2/D_0. In addition, we choose k_BT as our unit of energy. Other choices are possible (e.g ϵ). However, the present choice facilitates the comparison with earlier hard-sphere results [48]. In the following we will always use reduced quantities and hence we omit the asterisk.

We performed calculations of the nucleation barrier, kinetic prefactor and nucleation rate as a function of supersaturation varying both parameters of the Yukawa potential $\beta\epsilon$ and κ. In ref. [60], the phase diagram has been computed as a function of $\beta\epsilon$ for $\kappa = 5$, and as a function of κ, for $\beta\epsilon = 8$. We chose to study the same range of parameters. As was already mentioned above, in experiments, κ and ϵ are usually varied simultaneously. Hence, in order to compare with experiments, we have to combine and interpolate data from both sets of simulations.

One aspect of particular interest is the effect of the fcc-bcc-liquid triple point on the nucleation pathway. Already in 1897, Ostwald [36] formulated his famous 'step rule'. This rule states that the phase that nucleates from the melt need not be the most stable solid phase, but rather the one that is closest in free energy to the metastable liquid phase. Stranski and Totomanow [68] re-examined this rule and argued that the nucleated phase is the one that has the lowest nucleation barrier. Alexander and McTague [37] extended the Landau free energy expansion to freezing transitions that are weakly first order and concluded from general symmetry considerations that, in three dimensions, formation of the body-centered cubic (bcc) nuclei is uniquely favored for simple fluids. However, simulations by ten Wolde et al. [69] showed that the situation is more subtle, at least for the Lennard-Jones system: the core of the critical nucleus has the same structure as the stable crystal phase (fcc), but the surface bears a structural resemblance to the bcc phase that, for Lennard-Jones systems, is not stable. In the present system, we can "tune" the relative stability of the fcc and bcc solids by moving past the triple point. Hence, this is an ideal system to study nucleation of a metastable phase.

7.3   Simulations

For the calculation of the nucleation barrier we used a biased Monte Carlo method [48,69]. With this method we can compute the equilibrium probability $P(n)$ for the formation of a cluster of size n. This probability is related to the free energy of a crystalline cluster consisting of n particles: $\Delta G(n) = const - \ln[P(n)]$. We first computed the nucleation barrier at fixed $\kappa = 5$ for four different values of the amplitude of the Yukawa repulsion $\beta\epsilon = 2, 6, 8$ and 20. Increasing the contact value $\beta\epsilon$ of the Yukawa repulsion shifts the volume fraction of the liquid phase at freezing to lower values than the hard-sphere value $\eta = 0.494$. In order to be able to interpret our numerical data on the free-energy barrier for crystal nucleation, we need an accurate estimate

	f_{fcc}	f_{hcp}	f_{bcc}	f_{liquid}
$\beta\epsilon = 2$ $\kappa = 5$	12.894 (0.5425)	12.892 (0.5425)	- -	11.38 (0.5032)
$\beta\epsilon = 6$ $\kappa = 5$	23.258 (0.5027)	23.256 (0.5027)	21.49 (0.4808)	19.11 (0.4503)
$\beta\epsilon = 8$ $\kappa = 5$	24.344 (0.4563)	24.35 (0.4563)	24.32 (0.4558)	22.23 (0.4329)
$\beta\epsilon = 20$ $\kappa = 5$	20.872 (0.2888)	20.873 (0.2888)	20.986 (0.2895)	16.16 (0.2529)
$\beta\epsilon = 8$ $\kappa = 10$	11.144 (0.4084)	11.147 (0.4084)	11.067 (0.4054)	10.02 (0.3853)
$\beta\epsilon = 8$ $\kappa = 3.33333$	39.107 (0.5168)	39.110 (0.5168)	- -	38.08 (0.5055)

Table 7.1: Excess free energy per particle for the different bulk structures and the liquid state calculated via a thermodynamic intergration in the limit of infinite number of particles [44]. The statistical accuracy of the computed free energy of the liquid is estimated to be $\pm 0.01 k_B T$. In the table, the values in brackets indicate the volume fraction at which the excess free energy was calculated. The calculated excess free energies for the fcc and the hcp structures can be compared directly, as they were calculated at the same pressure, whereas the others are not. The fcc-hcp free energy difference is always smaller than $(1 \times 10^{-2} k_B T)$.

of the density, pressure and chemical potential of the liquid at freezing. The data of ref. [60] were obtained using a (modified) Gibbs-Duhem integration method. While this technique is useful to estimate the location of solid-liquid coexistence curves, the computed coexistence data were not sufficiently accurate for the present purpose. We therefore computed the location of all coexistence points by direct free-energy calculation of the solid and liquid phases [7]. The results for the excess free energy per particle are summarized in Table 7.1. From the computed free energies, we obtain estimates for the chemical potential at freezing that have an error of $\pm 0.01 k_B T$. We found the following values for the volume fraction of the liquid phase at freezing: $\eta = 0.482, 0.438, 0.405$ and 0.262 for $\beta\epsilon = 2, 6, 8$ and 20, respectively (see Table 7.2).

7.3.1 Nucleation barriers

In Fig. 7.3 we show the results for the barrier height as a function of supersaturation with respect to the stable solid phase (fcc). As the figure shows, the main effect of increasing the strength of the Yukawa repulsion is to lower the nucleation barrier at constant supersaturation $\Delta\mu$.

Note that the decrease of the height of the nucleation barrier is particularly strong when only a weak repulsion is added to the hard-core potential. In particular, switching on a repulsive Yukawa potential with a contact value of only $2 k_B T$ decreases the nucleation barrier by some $10 k_B T$. This implies that for real hard-sphere colloids, the presence of only a small amount of charge can enhance the nucleation rate at constant volume fraction by many orders of magnitude through two mechanisms: first of all, the charge increases the supersaturation at constant density. This effect would shift the nucleation curve to lower densities. But, in addition, the charge lowers the nucleation barrier at constant supersaturation. Further increase of the strength of the Yukawa repulsion leads to some additional decrease of the nucleation barrier, but the effect seems to saturate for values of $\beta\epsilon$ between $8 - 20$. Let us next consider the effect
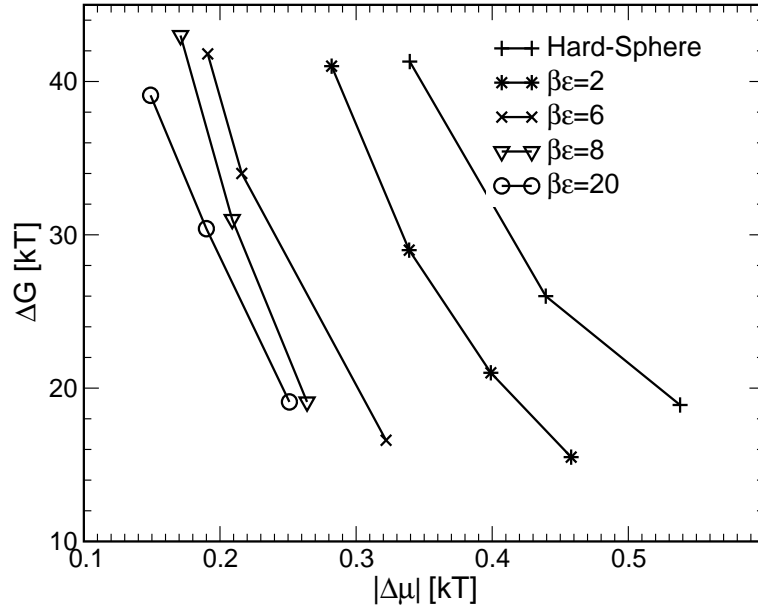
Figure 7.3: Calculated barrier heights of the hard-core Yukawa system with $\kappa = 5$ and $\beta\epsilon = 2, 6, 8, 20$ plotted as a function of supersaturation $\Delta\mu$ of the liquid phase with respect to the stable fcc phase.

of the range of the repulsive potential on the nucleation barrier. We computed the height of the crystallization barrier for $\kappa = 10, 5$ and 3.33333 at a fixed contact value $\beta\epsilon = 8$. In addition, we know the behavior of the system in the hard-sphere limit ($\kappa = \infty$). As κ is decreased, the range of the potential grows. Initially (as κ is decreased from ∞ to 10, the density at which the liquid freezes shifts from $\eta = 0.494$ to $\eta = 0.354$. Subsequently, the freezing density increases again. For $\kappa = 5$, the volume fraction at freezing is $\eta = 0.405$ and for $\kappa = 3.333$, the liquid freezes at $\eta = 0.456$. The variation of the crystallization barrier with κ and $\Delta\mu$ is shown in Fig. 7.4. The figure shows that increasing the range of the repulsive interaction, at constant supersaturation, initially has the effect to lower the nucleation barrier. However, as κ is decreased below 5, the nucleation barrier starts to increase again.

From the CNT expression for the height of the nucleation barrier Eq. (7.2), we can estimate the corresponding values for the liquid/fcc interfacial free energy γ_{fcc}. In Fig. 7.5 we show the variation of the interfacial free energy with $\beta\epsilon$ at fixed κ. Fig. 7.6 shows the variation of the interfacial free energy with κ at fixed $\beta\epsilon$ for various values of the supersaturation $\Delta\mu$. The dependence of the interfacial free energy on the range of repulsion mirrors that of the nucleation barrier and is therefore non-monotonic. Coming from the hard-sphere limit, the interfacial free energy initially goes down, but for κ less than 5, it increases again.

In refs. [48, 70] we found that, for hard spheres, the interfacial free energy γ increases with supersaturation $\Delta\mu$. As can be seen in Fig. 7.6, such behavior is also observed in a system of charged colloids. In polydisperse hard-sphere systems [70], the increase of γ with supersaturation could even result in a non-monotonic dependence of the nucleation barrier on supersaturation. In the present system, the interfacial free energy also increases with supersaturation, but the effect is not strong enough to result in a minimum in the nucleation barrier.
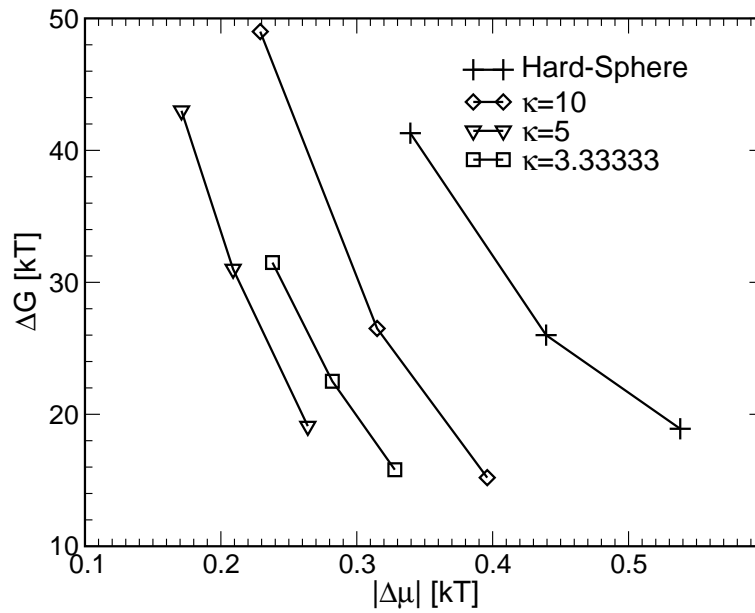
Figure 7.4: Calculated barrier heights of the hard-core Yukawa system with $\beta\epsilon = 8$ and $\kappa = 10, 5, 3.33333$ plotted as a function of supersaturation $\Delta\mu$ of the liquid phase with respect to the stable fcc phase.

7.3.2 Nucleation rates

In order to calculate the absolute nucleation rate Eqn. (7.3), we need to evaluate the kinetic prefactor, which has the following form: $\Gamma = Z\rho_l f^+_{n_{crit}}(\sigma^5/D_0)$ [17]. Here Z is the Zeldovich factor, ρ_l the number density of the liquid phase and $f^+_{n_{crit}}$ the attachment rate of particles to the critical cluster. D_0 denotes the diffusion coefficient of the charged colloids at infinite dilution and σ is the hard-core diameter of the Yukawa particles. The Zeldovich factor $Z = [|\Delta G''(n_{crit})|/(2\pi kT)]^2$ depends only on the second derivative of the nucleation barrier at its maximum. This information we obtain directly from our numerical results for $\Delta G(n)$. In order to compute $f^+_{n_{crit}}/D_0$, we used the kinetic Monte Carlo scheme of ref. [26]. Basically, the method is a numerical scheme to solve the Smoluchowski equation. In doing so, we neglected the hydrodynamic interactions between the colloids. This drawback can be remedied by using the solution suggested by Medina-Noyola [27]. In this approach, the hydrodynamic interactions are taken into account through their effect on the short-time self-diffusion coefficient. In practice, this means that we assume that, at short times, the mean-squared displacement of a particle is not dominated by the infinite-dilution value of the diffusion coefficient D_0, but by the short-time self-diffusion coefficient D_S^S. The latter quantity differs from D_0 precisely because of hydrodynamic interactions. We therefore need to know the value of the ratio D_S^S/D_0 at the liquid density of interest. For hard-sphere suspensions, approximate expressions exist for the density dependence of D_S^S/D_0, e.g. $(1 - \eta/0.64)^{1.17}$ [28]. As a test of this procedure, we used it to estimate the long-time self-diffusion coefficient of dense hard-sphere suspensions. The results agree within the statistical error with the available experimental data, see section 4.2. This gives us confidence that a similar approach can also be used to compute nucleation rates. However, the Medina-Noyola procedure is not directly applicable to the Yukawa system. To resolve this problem, we assumed that we could map the dynamics of the Yukawa system onto that of the hard-sphere system. To this end, we defined an effective packing fraction of the Yukawa system such that the packing fractions at freezing of both systems were equal. This mapping is inspired by the observation
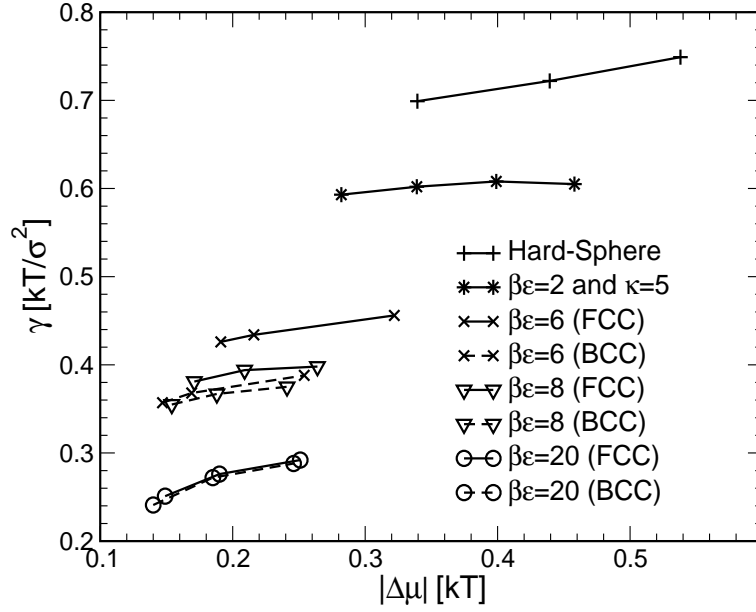
Figure 7.5: Interfacial free energy calculated from the barrier heights Eq. 7.2 for $\kappa = 5$ and $\beta \epsilon = 2, 6, 8, 20$. The solid lines are the results assuming that the nuclei have a fcc structure, and the dashed lines are the results if the nuclei are bcc.

of Löwen et al. [71] that for many different colloidal systems, the ratio D_L^S/D_S^S has a "universal" value of 0.1 at freezing (here D_L^S is the long-time self-diffusion constant). This rule suggests a dynamic "corresponding-states principle" provided all densities are scaled to the freezing density. In fact, experiments by Van Blaaderen et al. [72] suggest that, for dense, charged colloids such a rescaling of the long-time self-diffusion coefficient is justified. While this approach is rather *ad hoc*, the systematic errors that it might induce are smaller than the random errors due to statistical inaccuracies in the determination of the height of the nucleation barrier.

Results

Our results for the computed nucleation rates are shown in Fig. 7.7 and Fig. 7.8, where we plot the nucleation rate as a function of supersaturation. As the kinetic prefactor does not vary strongly with either supersaturation or interaction potential, the variation of the nucleation rate shown in Figs. 7.7 and 7.8 reflects the behavior of the barrier height.

In order to compare the computed crystallization rates with the results of the confocal microscopy experiments of ref. [52], we need to know the potential parameters that best characterize the experimental system they used. From the fact that the suspensions studied by Gasser et al. freeze at a volume fraction $\eta = 0.38$, it is clear that the colloidal particles used in these experiments are slightly charged. It is therefore natural to describe them by a Yukawa model that also has its freezing point at $\eta = 0.38$. This condition is, however, not sufficient to fix the values of both κ and ϵ. For instance, if $\kappa = 5$, then the observed freezing density can be reproduce by choosing $\beta \epsilon \sim 7$. Conversely, if we choose $\beta \epsilon = 8$, then there are in fact, two values of κ that will reproduce the observed freezing density ($\kappa \sim 20$ and $\kappa \sim 6$) [60].

In Fig. 7.9, we show a comparison of the nucleation rates reported in ref. [52] with the simulation results for those κ-$\beta \epsilon$ combinations that yield a freezing point near $\eta = 0.38$. As can be seen from the figure (and from the numbers collected in Table 7.2), different κ-$\beta \epsilon$ combinations yield very different nucleation rates. However, the main effect of the variation of κ and
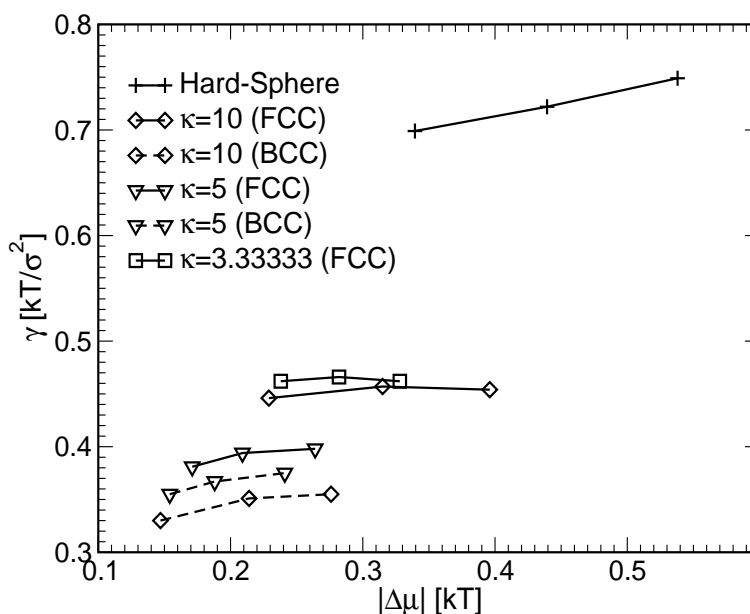
Figure 7.6: Interfacial free energy calculated from the barrier heights Eq. 7.2 for $\beta\epsilon = 8$ and $\kappa = 10, 5, 3.33333$. The solid lines are the results assuming that the nuclei have a fcc structure, and the dashed lines are the results if the nuclei are bcc.

ϵ is to shift the nucleation curves horizontally: the slopes of the different curves are all rather similar. When we compare the computed nucleation rates with the experimental data, we note two things: first of all, the experimental rates tend to be (much) higher than the computed rates (Gasser et al. find $-6.9 \leq \log[I] \leq -6.5$ for η between 0.45 and 0.53). But, more importantly, the experiments suggest that the nucleation rate barely varies with volume fraction. This observation is hard to reconcile with the behavior of any of the Yukawa models that we studied. This discrepancy between experiment and simulation results suggests that it is incorrect to assume that the experimental system can be mapped onto a Yukawa model with density-independent κ and ϵ. On the contrary, it is very likely that the effective potential parameters of weakly charged colloids in the absence of added salt depend strongly on concentration. In fact, recent experiments by Schöpe et al. [66] clearly illustrate this effect: with increasing concentration, the effective potential of charged polystyrene spheres in dilute aqueous solution, becomes increasingly hard-sphere like. If we assume that the same phenomenon occurs in the more concentrated suspensions of ref. [52], then experimental results for the nucleation rates at different densities should be compared with the numerical predictions that correspond to different effective Yukawa potentials.

As can be seen from Fig. 7.9, the variation of the nucleation rate with density can be strongly reduced (and can possibly even become non-monotonic) if, as we expect, ϵ and κ decrease with density. It is, however, not obvious that this effect is large enough to account for the apparent discrepancy between experiment and simulation. Clearly, a truly quantitative comparison between simulation and experiment requires better knowledge of the density dependence of the effective interaction between slightly charged colloidal spheres.

7.3.3 Nucleation pathways

The repulsive Yukawa system offers a unique opportunity to study the effect of meta-stable crystal phases on the pathway for crystal nucleation. The role of meta-stable phases in crystal
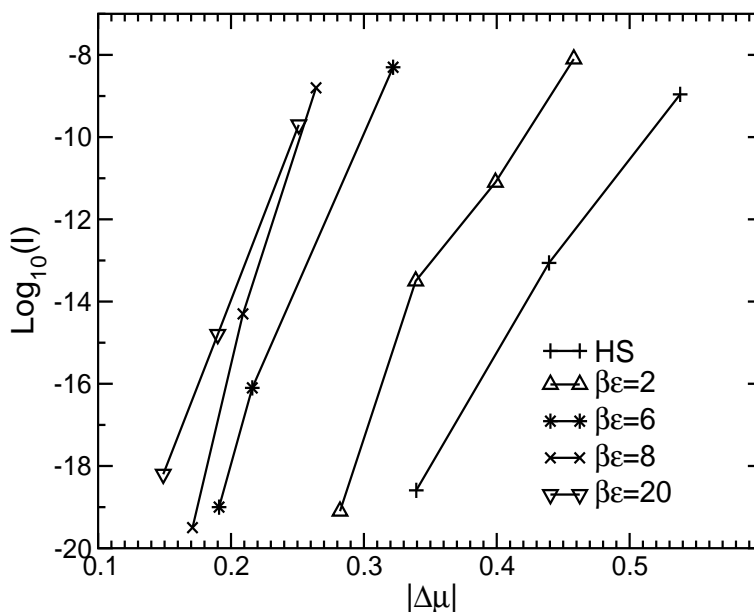
Figure 7.7: Dependence of the crystallization rates on the amplitude of the Yukawa repulsion $\beta\epsilon = 2, 6, 8, 20$ for $\kappa = 5$ plotted as a function of supersaturation $\Delta\mu$ of the liquid with respect to the stable fcc phase.

nucleation was first pointed out by Ostwald [36] who, in 1897, formulated his "step rule". This rule states that the crystal phase that is nucleated from solution need not be the one that is thermodynamically most stable, but the one that is closest in free energy to the fluid phase. Stranski and Totomanow [68] reexamined this rule and argued that the nucleated phase is the phase that has the lowest free-energy barrier of formation, rather than the phase that is globally stable under the conditions prevailing. More recently, Alexander and McTague [37] argued, on the basis of Landau theory, that in the early stages of crystal nucleation the formation of bcc crystallites should be favored. Similar conclusions were subsequently reached by other groups [38, 39]. In the Yukawa system, the fluid phase can coexist with either the fcc or the bcc phase, depending on the values of κ and $\beta\epsilon$ (see Fig. 7.2). We can therefore study crystal nucleation both in the regime where the fcc phase is stable, and where the bcc phase is stable. If Ostwald's rule would strictly apply, we should expect that fcc nuclei should form where bcc crystals are stable, and conversely. On the other hand, if the Alexander-McTague scenario is correct, we should expect to find that bcc nuclei are always preferred. There is little point in testing the Stranski-Totomanow hypothesis as it amounts almost to a tautology ("the phase that nucleates fastest, is the one with the lowest nucleation barrier").

To study the effect of meta-stable intermediates on crystallization, we analyzed the structure of the (pre)critical nucleus in different regions of the phase diagram shown in Fig. 7.2. As can be seen from Fig. 7.2, the pressure range region where the bcc phase is stable is rather narrow. For these pressures, the supersaturation of the fluid phase is small, and hence the nucleation barrier is very high. As a consequence, we could only study the formation of pre-critical nuclei in this regime. In order to study the structure of the (pre)critical nuclei, we used the local bond-order analysis proposed by ten Wolde et. al. [69]. In this analysis the local bond-order signature of a nucleus is decomposed into the signatures of the different bulk structures (liquid, fcc and bcc) using a linear least square fit. The value of the resulting coefficients $\{f_{\text{liq}}, f_{\text{fcc}}, f_{\text{bcc}}\}$ are a measure of the structure of the nucleus.

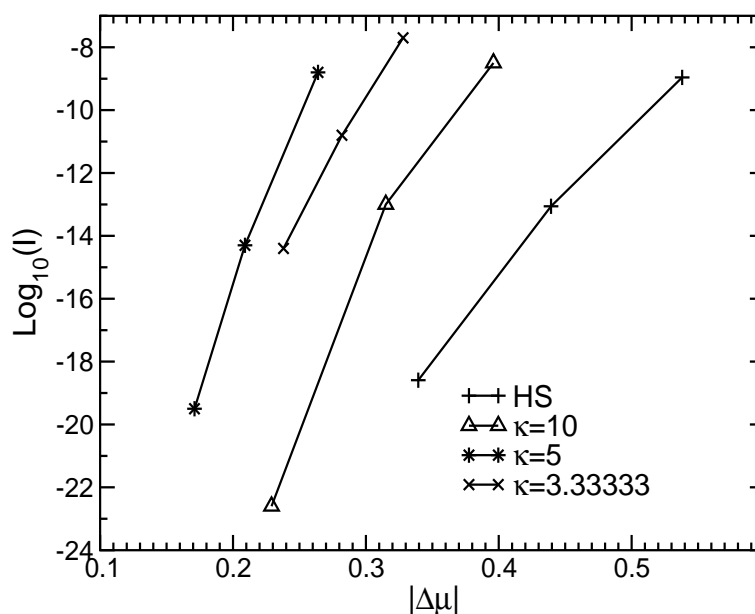Our simulations show that the pre-critical nuclei always have a strong bcc signature. Only

Figure 7.8: Dependence of the crystallization rates on the inverse screening length $\kappa a = 10, 5, 3.33333$ for $\beta \epsilon = 8$ plotted as a function of supersaturation $\Delta \mu$ of the liquid with respect to the stable fcc phase.

for larger (post)critical nuclei well inside the fcc regime, do we find a mixture of bcc and fcc signatures. In this sense, our simulations unambiguously support the prediction that nucleation into bcc nuclei is always uniquely favored, even when the fcc phase is closer in free energy to the fluid phase.

Fig. 7.10 shows the results of our cluster analysis for two distinct nuclei of size $n = 100$ and $n = 200$. The picture shows the variation of the structural signature with the distance from the center of mass of the nucleus. The results shown in this figure apply to the case $\kappa = 10$ and $\beta \epsilon = 8$. This corresponds to the points in the phase diagram where the preference for the fcc structure is strongest. The core of the cluster of size $n = 100$ has a clear bcc signature while the fcc phase does not seem to play a role. However, for the larger nuclei ($n = 200$) the core of the nuclei becomes fcc like while the bcc phase seem to disappear. In this case the cluster transformation happened before it could reach critical size. This phase transition in the pre-critical nucleus allows us to quantify what value of the bcc-fluid interfacial free energy is needed in order to compensate for the difference in chemical potential of the two bulk structures. From our free-energy calculations, we deduce $\mu_{bcc} - \mu_{fcc} = 0.082 \pm 0.005$. We used the CNT expression for the barrier height to estimate the fcc-liquid interfacial free energy: $\gamma_{fcc} = 0.446$. The transformation from bcc to fcc nuclei occurred for $n \approx 100$. At that point, the gain in bulk free energy is $100 * 0.082 = 8.2 k_B T$. This free-energy gain must be compensated by the increase in surface free energy as the crystallite transforms from bcc to fcc. To estimate this surface free energy, we need to know the radius of the crystal nucleus for $n = 100$. If we assume that the nucleus is spherical and that the solid is effectively incompressible, we arrive at the estimate $\gamma_{bcc} = 0.379$.

We find such a pre-critical transformation from bcc to fcc for $\beta \epsilon = 2$ with $\kappa = 5$, and for $\beta \epsilon = 8$ with $\kappa = 10$ and 3.33333. In all the other cases ($\beta \epsilon = 6, 8, 20$ with $\kappa = 5$) even the critical nuclei had a strong bcc signature. This observation has implications for the interfacial free energies shown in Figs. 7.5 and 7.6. In these figures, we show interfacial free energies that were computed from the CNT expression for the barrier height, assuming that the nucleus
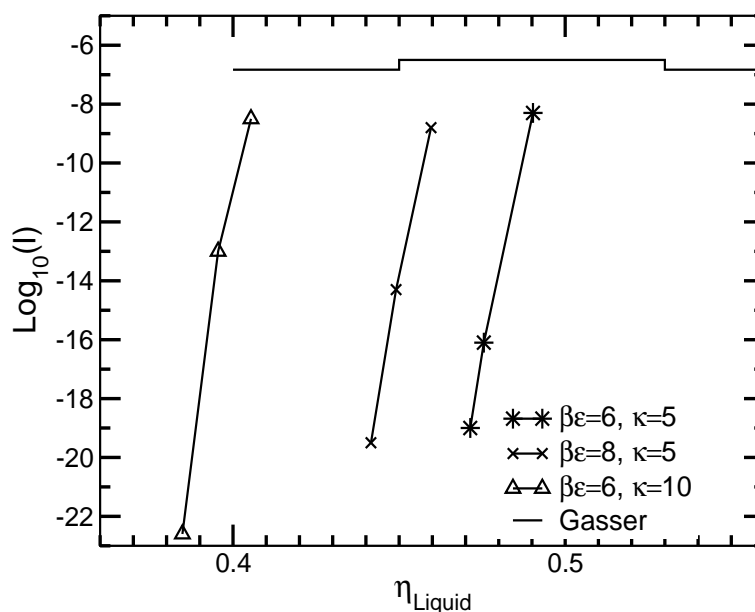
Figure 7.9: Comparison between the experimentally measured nucleation rates [52] and the simulation data. In the plot we added only the data sets which match the freezing density of the experimental system.

had the same structure as the stable crystal phase. We now see that, in some cases, the critical nucleus has a meta-stable bcc structure. This affects the value for $\Delta\mu$ in the CNT expression, and hence our estimate for γ. In the cases where the critical nucleus has a bcc structure, we therefore also estimated the value of γ_{bcc} from the height of the nucleation barrier. The results are also shown in Figs. 7.5 and 7.6.

Thus far we did not mention the possibility that the structure of the crystal nuclei could also be hexagonal closed packed (hcp) or a random stacking of the fcc and hcp domains (rhcp). In the case of hard-spheres it is known that the free-energy difference between the stable fcc and hcp solid structure is very small ($\approx 10^{-3}k_BT$) and therefore stacking faults are expected. Such stacking faults have been observed in experiments and computer simulations. In the case of charged spheres the situation is less clear. Some experiments indicate that the situation changes and there seems to be tendency that crystal nuclei become more fcc-like [73]. Other experiments suggest that the structure of the cluster is still rhcp [52]. To resolve this question for the present model system, we first calculated the free energy difference between the fcc and hcp solid, for all the different parameters of the model potential for which we performed the rate calculations. It turns out that the free energy difference per particle between the fcc and hcp structure was always smaller than $1 \times 10^{-2}k_BT$ (see Table 7.1), which is about the limit of the accuracy that we had in our calculations. This means that thermal fluctuations on the order of a few k_BT could easily transform clusters containing hundreds of particles from fcc to hcp, or generate intermediate stackings. To find out if this really happens we, analysed the stacking of the (111)-planes of 10 nuclei with parameters $\beta\epsilon = 8, \kappa = 10$ and $\beta\epsilon = 8, \kappa = 3.33333$. In both cases, we do find stacking faults, but they seem to be less frequent than in the pure hard-sphere case. We stress, however, that these preliminary conclusions are based on the analysis of only a small number of crystallites.
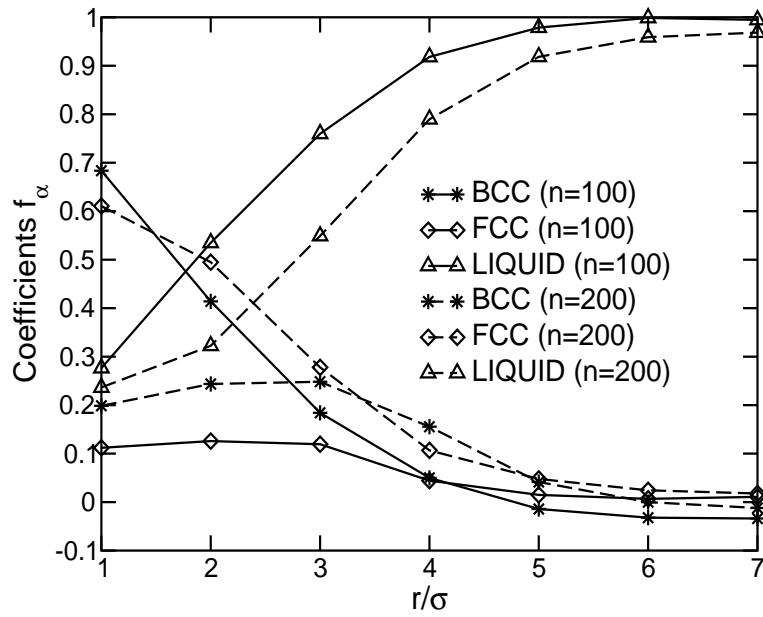
Figure 7.10: Structure analysis of two independent crystal nuclei of size $n = 100$ and 200 from the simulations with parameters $\beta\epsilon = 8$ and $\kappa = 10$. The figure shows the results for the fit parameters for the local bond-order analysis as a function of the distance from the center of mass of the nuclei. The core of the cluster of size $n = 100$ has a clear bcc signature, where the cluster of size $n = 200$ shows a clear fcc structure.

7.4   Appendix A: Protocol of the simulation

The nucleation barrier was calculated analog to the simulations in a system of monodisperse hard-sphere colloids, which is described in detail in section 4.1. The radius for the local environment of a particle was set to 1.5σ. The threshold for the dot product $q_6q_6 = 20$ and the threshold for the number of connection was set to 7. Two solid-like particles were considered to belong to the same nuleus if their distance was smaller than 1.8σ. For our NPT- Monte Carlo simulation we used 3375 particles. In each simulation we performed 600000 moves per particle. To enhance the stacking rearrangement of the cluster we also applied the parallel tempering scheme [22]. The calculation of the kinetic factor referred to in the text is described in section 4.2. The attachment rate was estimated on the basis of five trajectories during which we measured the size fluctuation of the critical cluster.

7.5   Appendix B: Calculation of the chemical potential

The chemical potential for the liquid and solid phases was calculated by a thermodynamic integration using Eq. (5.9):

$$\frac{\mu(\rho)}{k_BT} = \frac{F^{id}(\rho)}{Nk_BT} + \frac{F^{ex}(\rho_{ref})}{Nk_BT} + \frac{1}{k_BT}\int_{\rho_{ref}}^{\rho} d\rho'\left(\frac{P(\rho') - \rho'k_BT}{\rho'^2}\right) + \frac{P(\rho)}{\rho k_BT}. \tag{7.4}$$

Once the excess free energy $F^{ex}(\rho_{ref})$ at a reference density ρ_{ref} is known, the chemical potential can be calculated at any density by a numerical integration. The equation of state $P(\rho)$ was measured with a Monte Carlo simulation. Still, the excess free energy needed to be calculated in a separate simulation. To do that, we also performed a thermodynamic integration where we

	P	η_{liq}	η_{fcc}	η_{bcc}	$\Delta\mu_{fcc}$	$\Delta\mu_{bcc}$	ΔG^*	$f^+_{n_{crit}}/D_0$	$\log_{10}(I)$
$\kappa = 5$	25	0.5103	0.5420	-	0.28	-	41	46	-19.1
and	26	0.5159	0.5484	-	0.34	-	29	84	-13.5
$\beta\epsilon = 2$	27	0.5218	0.5551	-	0.40	-	21	6	-11.1
	28	0.5257	0.5599	-	0.46	-	15.5	19	-8.1
$\kappa = 5$	37	0.4714	0.4827	0.4808	0.19	0.15	48.1	202	-19
and	38	0.4755	0.4864	0.4848	0.22	0.17	34	57	-16.1
$\beta\epsilon = 6$	42	0.4903	0.5031	0.5004	0.32	0.25	16.6	52	-8.3
$\kappa = 5$	38	0.4415	0.4487	0.4481	0.17	0.15	43	218	-19.5
and	40	0.4491	0.4563	0.4558	0.21	0.19	31	200	-14.3
$\beta\epsilon = 8$	43	0.4596	0.4671	0.4668	0.26	0.24	19.1	300	-8.8
$\kappa = 5$	23	0.2859	0.2888	0.2895	0.15	0.14	39.1	167	-18.2
and	25	0.2938	0.2973	0.2974	0.19	0.19	30.4	58	-14.8
$\beta\epsilon = 20$	28	0.3048	0.3084	0.3083	0.25	0.25	19.1	53	-9.7
$\kappa = 10$	18	0.3848	0.3978	0.3949	0.23	0.15	49	80	-22.6
and	20	0.3955	0.4084	0.4054	0.32	0.21	26.5	44	-13
$\beta\epsilon = 8$	22	0.4054	0.4180	0.4150	0.40	0.28	15.2	11	-8.5
$\kappa = 3.33333$	57	0.4937	0.5042	-	0.24	-	31.5	205	-14.4
and	59	0.4996	0.5106	-	0.28	-	22.5	81	-10.8
$\beta\epsilon = 8$	61	0.5055	0.5168	-	0.33	-	15.8	80	-7.7

Table 7.2: Summary of the data for the calculations with the repulsive hard-core Yukawa potential. Here P is the Pressure and $\eta_{liq}, \eta_{fcc}, \eta_{bcc}$ the corresponding volume fraction of the liquid, fcc and bcc phase. $\Delta\mu_{fcc}$ and $\Delta\mu_{bcc}$ is the difference in chemical potential between the liquid and the fcc/bcc phases. ΔG^* are the measured crystallization barriers. $f^+_{n_{crit}}/D_0$ is the reduced attachment rate of particles to the critical cluster. I is the calculated reduced nucleation rate.

couple our system to a system of known excess free energy. The free energy difference between the two systems is then given by [7]:

$$F^{ex}(\lambda = 1) - F^{ex}(\lambda = 0) = \int_{\lambda=0}^{\lambda=1} d\lambda \left\langle \frac{\partial U(\lambda)}{\partial \lambda} \right\rangle_\lambda, \qquad (7.5)$$

where λ is the coupling parameter. $U(\lambda = 0)$ corresponds to the potential energy of our system of interest and $U(\lambda = 1)$ is the potential energy of the reference system. Note that the free energy difference is expressed by an integration over the ensemble average of the potential energy.

For the calculation of the excess free energy of the hard-core yukawa liquid we used as a reference system the pure hard-sphere liquid. In this case the internal energy $U(\lambda)$ is given by:

$$U(\lambda) = U_{HS} + (1 - \lambda)U_{YK}, \qquad (7.6)$$

where U_{HS} and U_{YK} corresponds to the potential energy of the hard-shere and the hard-sphere Yukawa system. For $\lambda = 1$ we have the pure hard-sphere system and for $\lambda = 0$ the hard core Yukawa system is recovered. It follows that the difference in free energy is given by

$$F^{ex}(\lambda = 1) - F^{ex}(\lambda = 0) = \int_{\lambda=0}^{\lambda=1} d\lambda \left\langle U_{YK} \right\rangle_\lambda. \qquad (7.7)$$

In some cases it was also possible to calculate the excess free energy of the solid in the same way. However at strong Yukawa repulsions the freezing density was shifted to such low values that the pure hard-sphere solid would melt. In these cases, and for all free energy calculations of the bcc structure, we coupled our system to an Einstein crystal. The potential energy of this

sytem is given by

$$U(\lambda) = U_{HS} + (1 - \lambda)U_{YK} + \lambda[\sum_{i=1}^{N} c(\mathbf{r}_i - \mathbf{r}_{0,i})^2]. \tag{7.8}$$

Here the sum goes over all particles N, $\mathbf{r}_i$ is the position of particle i, $\mathbf{r}_{0,i}$ is the lattice position of particle i around which it is fluctuating and c is the spring constant. The exact expression for the difference in excess free energy is given in [44]. Our results are summarized in table 7.1.

8

Phase behavior and crystallization kinetics of PHSA-coated PMMA colloids

Polymethylmethacrylate (PMMA) colloids sterically stabilized by a layer of chemically-grafted poly-12-hydroxystearic (PHSA) are widely used in experiments as model hard-spheres. However, due to the coating, the interaction between particles is slightly soft. Here we report a numerical study of the effect of the PHSA coating on the phase behavior and crystallization kinetics of PMMA colloids based on parameters determined from surface-force measurements PHSA [74,75]. We find that the core volume fraction of particles at freezing measured by Pusey and van Megen [41] can only be reproduced by using a thickness of the PHSA layer that is considerably larger than literature values. This may indicate that the particles are in fact slightly charged. Compared to perfect hard spheres, the crystallization rate in these slightly soft particles was found to be increased by about two orders of magnitudes.

8.1   Introduction

A disordered collection of hard spheres is perhaps the simplest possible interacting fluid. The experimental realization of a colloidal suspension that closely mimics the phase behavior of hard-spheres was a milestone in soft matter research [45,53,76]. Pusey and van Megen showed in the 1980s that polymethylmethacrylate (PMMA) particles stabilised by chemically-grafted polyhydroxystearic acid (PHSA) system reproduced closely the equilibrium phase behavior expected of hard-spheres [53]. Other model systems are also known [77,78]. Recently, it was shown that the crystallization kinetics of hard-spheres predicted by computer simulations [48] differed by several orders of magnitude from the crystallization rates measured in model colloids [3–5,29,30,35,62]. Polydispersity in the synthetic colloids cannot account for this discrepancy [70]. Another possible explanation is a slight softness in the interparticle potential. In this report, we investigate how such softness may affect phase behavior and crystallization kinetics.

In the following we first introduce a model potential for PHSA-coated PMMA spheres. Using this potential we calculate the freezing and melting volume fractions. These quantities can be compared to values obtained in experiments [41]. Next, we study how the softness affects the crystallization kinetics by calculating the nucleation barrier and the nucleation rates at different volume fractions.
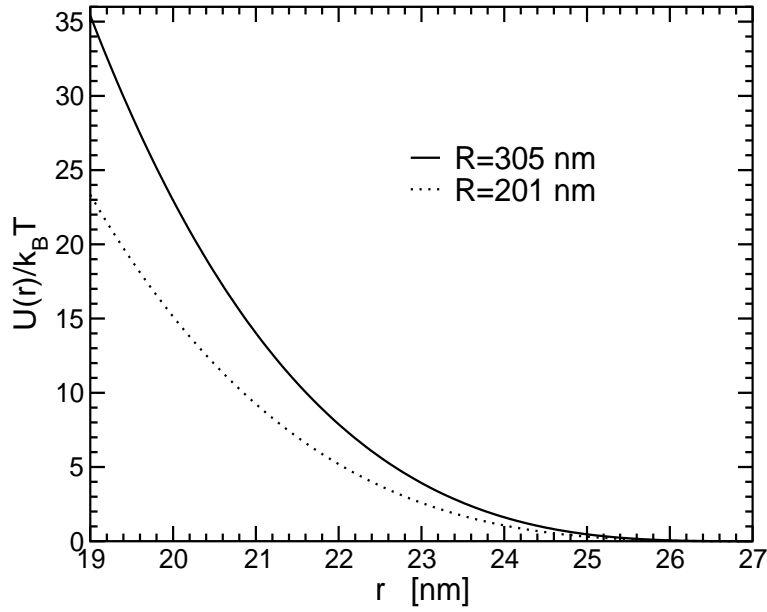
Figure 8.1: Estimated interaction potential between two PMMA spheres coated with a layer of PHSA. The curves were computed using the Alexander-de Gennes scaling blob model. Results are shown for two sphere radii $R = 201\,nm$ and $305\,nm$. For the density of the grafted chains we used a value $s = 2.0\,nm$ and the layer thickness was assumed to be $L = 13.5\,nm$. The prefactor $\alpha = 0.025$ was taken from the experimental data.

8.2   Model potential

The potential that we used to model the interaction between two PHSA-coated PMMA spheres was deduced from surface-force measurements. Costello et al. [74, 75] measured the force between two mica surfaces coated with a PMMA (backbone)-PHSA (sidechain) comb copolymer, with the PMMA backbone directly adsorbed on the mica and the PHSA side chains protruding into the solvent. The interaction thus mimics that between the surfaces of two PHSA-stabilized PMMA colloids. The measurements of Costello et al. followed a model proposed by Alexander and de Gennes [79,80]. In this model, expected to be valid for high grafting densities, each chain is assumed to consist of connected semi-dilute blobs. The chains are stretched by osmotic repulsion between the blobs. This tendency is opposed by the increase in elastic free energy of the chain upon stretching. The resulting expression for the force per unit area between two parallel plates at a distance r is

$$F(r) = \frac{\alpha k_B T}{s^3} \left[\left(\frac{2L}{r}\right)^{9/4} - \left(\frac{r}{2L}\right)^{3/4} \right], \tag{8.1}$$

where s is the mean spacing between between grafting points and L is the thickness of the polymer layer; α is a numerical prefactor and $k_B T$ the thermal energy. The expression is supposed to hold for $0 < r < 2L$. Integration yields the corresponding energy density. From the distance of onset of the interaction, Costello et al. estimated that their layer thickness was $L = 12.5$ nm. A fit of the Alexander-de Gennes model to experimental measurements yielded $\alpha = 0.025$ and $s = 2.8$ nm. By using the Derjaguin approximation (see e.g. Ref. [81]) we can estimate the interaction potential between two spheres. Different methods have been used to measure the thickness of the PHSA layer on PMMA colloids synthesized according to the method of Antl et al. [82], giving values of $L = 7$-13 nm [83–87] and a maximum distance between grafting points
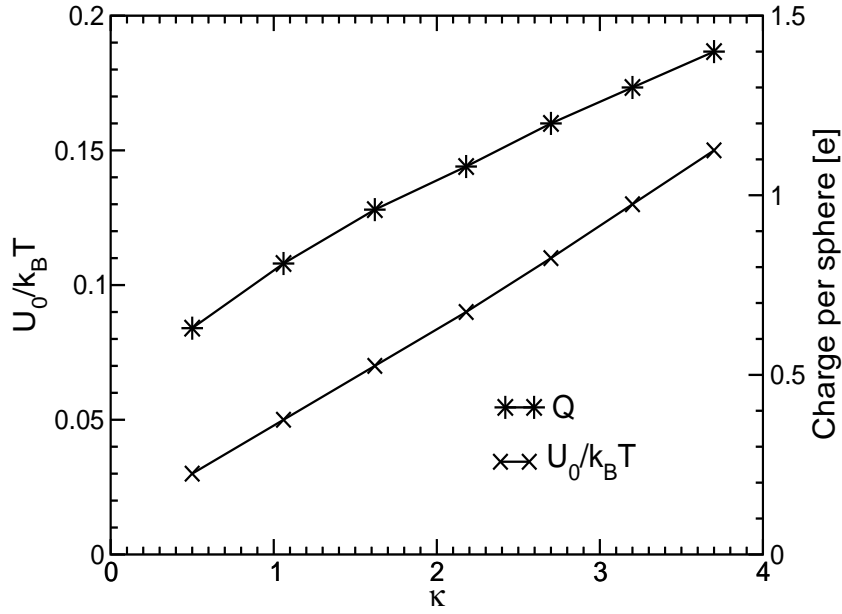
Figure 8.2: Calculated parameter set $U_0/k_B T$,κ of a hard-core yukawa potential that accounts for the observed shift in the freezing density.

of $s = 2.0$ nm [88].

In our simulations we used $L = 13.5$ nm and $s = 2.0$ nm to yield the strongest repulsion compatible with the experimental data. The resulting interaction potentials for spheres with radii $R = 305$ nm and 201 nm are shown in Fig. 8.1. These radii correspond to the particles sizes used by Pusey and van Megen [41] and Harland and van Megen [3] respectively. As can be seen, the interaction potential increases steeply to $10 k_B T$ within $6 - 7$ nm from the point of first contact.

8.3   Phase behavior

We used the potential obtained in the previous section to calculate the freezing and melting densities of the colloidal suspensions. At coexistence the chemical potential and the pressure of the fluid and the solid phase are equal. The chemical potential of the fluid and the solid phase can be calculated from simulations using thermodynamic integration [7]

$$\frac{\mu(\rho)}{k_B T} = \frac{F^{id}(\rho)}{N k_B T} + \frac{F^{ex}(\rho_{ref})}{N k_B T} + \frac{1}{k_B T} \int_{\rho_{ref}}^{\rho} d\rho' \left(\frac{P(\rho') - \rho' k_B T}{\rho'^2} \right) + \frac{P(\rho)}{\rho k_B T}, \qquad (8.2)$$

where P is the pressure, N the number of particles in the system and $F^{id}(\rho)/N k_B T = \ln(\rho) - 1$ is the dimensionless free energy per particle at density ρ. In addition we need to know the excess free energy $F^{ex}(\rho_{ref})$ of the liquid and the solid at a reference density ρ_{ref}, which was calculated in a separate simulation. We performed a thermodynamic integration where we coupled our system to a system of known excess free energy (in this case the hard-sphere system). The result for the excess free energy of the liquid and a fcc solid for the particles with radii $R = 201$ nm are $F^{ex}_{liq}(\rho_{ref} = 0.8495)/N k_B T = 4.9557$ and $F^{ex}_{fcc}(\rho_{ref} = 0.94458)/N k_B T = 6.0262$. For the system with $R = 305$ nm we obtained $F^{ex}_{liq}(\rho_{ref} = 0.8607)/N k_B T = 4.5605$ and $F^{ex}_{fcc}(\rho_{ref} = 0.9559)/N k_B T = 5.6798$. The equation of state for the liquid and solid of the slightly soft system was measured in a Monte Carlo simulation and the integration to calculate the chemical potential was done

numerically. The resulting freezing and melting volume fractions for our model potential were then estimated to be $\phi_f = 0.4137$ and $\phi_m = 0.4579$ (for $R = 201$ nm) and $\phi_f = 0.4380$ and $\phi_m = 0.4850$ (for $R = 305$ nm). Thus, by scaling the freezing volume fractions to that of hard-spheres $\phi_f^{HS} = 0.494$ [33] we obtain the effective hard-sphere diameter $\sigma_{eff} = 1.061\sigma$ and $\sigma_{eff} = 1.041\sigma$ of the two systems. We can compare these diameter to the effective hard-sphere diameter predicted by first order perturbation theory

$$\sigma_{eff} = \int_0^\infty dr\{1 - exp[-U(r)/k_BT]\}. \tag{8.3}$$

The results $\sigma_{eff} = 1.061\sigma$ (for $R = 201$ nm) and $\sigma_{eff} = 1.041\sigma$ (for $R = 305$ nm) are identical to the estimate above. The values for the interaction potential at this distance are $U(r = \sigma_{eff})/k_BT = 0.7056$ and 0.7065. If we use the effective hard-sphere diameter to rescale the melting volume fractions of the soft systems to that of the hard spheres we find $\phi_m = 0.5469$ and $\phi_m = 0.5463$ (to be compared with $\phi_m^{HS} = 0.545$ [33]).

The results for the particles with $R = 305$ nm can be compared directly with the observations of Pusey and van Megen, who found *core* volume fractions at freezing and melting $\phi_f = 0.407$ and $\phi_m = 0.441$ [41]. The corresponding effective hard sphere diameter is $\sigma_{eff} = 1.067$. The experimental volume fractions are some 3.1% lower than the freezing volume fraction determined in our simulations. If we consider the fact that the particles are polydisperse (5%) the discrepancy is even 4.1% [46].

One may seek to obtain a better fit to experiments by varying the parameters s and L. The value of s used gives the minimum surface coverage (at aerial density s^{-2}) necessary for steric stabilization to function [88]. In any case, we find that the effective hard sphere diameter is somewhat insensitive to variations in s. Instead, agreement with the hard-core freezing volume fraction of Pusey and van Megen can be obtained by using a value of $L \approx 22$ nm. While there was no direct determination of the PHSA chain length for the batch of PMMA particles used by these authors, this value of L is twice to three times as long as values obtained from a variety of experiments on PHSA-coated PMMA particles [83–87]. It is therefore possible that there is an additional source of weak repulsion.

One possible source of this additional repulsion is a slight charge on the colloids. If we assume that the interaction between charged colloids is described by a repulsive hard core Yukawa potential: $U_0/k_BT exp[-\kappa(r/\sigma-1)]/(r/\sigma)$ for $r > \sigma$, we can use Eq. (8.3) to estimate the values of the parameter U_0/k_BT and κ needed to account for the observed shift in freezing volume fraction. Here U_0/k_BT is the value of the Yukawa repulsion at contact and κ is the inverse screening lenght in units of the hard-sphere diameter σ. We find that the added repulsion is indeed quite weak, and very soft (see Fig. 8.2). Note that such a weak, soft repulsion can hardly be detected in the surface-force measurement. We can estimate the charge on a particle from the contact value of the interaction potential: $U_0/k_BT = Q^2/4\pi\epsilon_0\epsilon\sigma$, where Q is the charge, ϵ_0 and ϵ are the permittivity of the vacuum and the PMMA. A value $U_0/k_BT = 0.1$ corresponds to an average colloidal charge of about one electron per sphere.

8.4 Crystallization kinetics

8.4.1 Homogeneous nucleation

When a liquid is compressed to densities beyond freezing crystallization can be very slow. The reason is that the free energy of a crystalline nucleus that forms in a supersaturated solution is the sum of two competing terms. The first is a bulk term, that favors the transformation from the liquid to the solid state. If n particles transform from liquid to solid the free energy gain
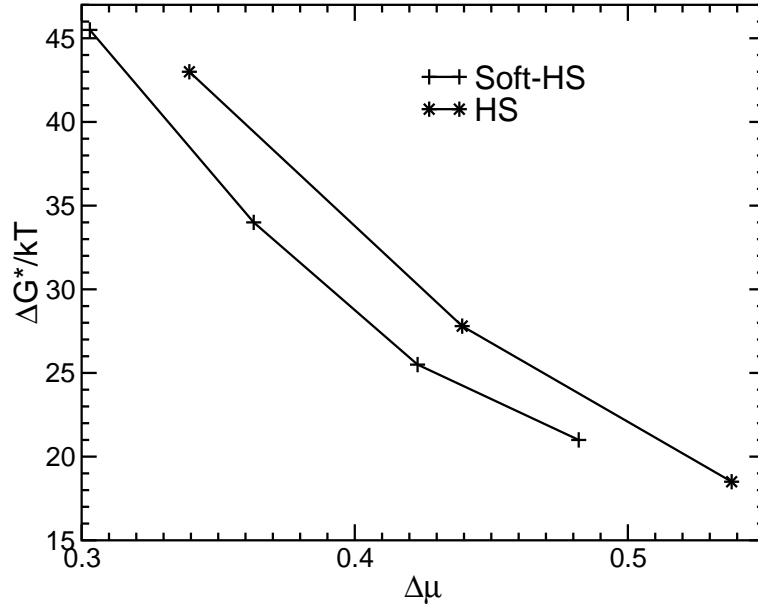
Figure 8.3: Computed crystal nucleation barriers for the slightly soft hard-sphere system plotted as a function of supersaturation. In addition we also show results from previous simulation on the pure hard-sphere system, to which the results can be compared.

is $n\Delta\mu$, where $\Delta\mu$ is the chemical potential difference between the two phases. This term is counterbalanced by the surface term, that describes the free energy required to create a liquid-solid interface $A\gamma$, where A is the surface area and γ the surface free energy density. For small crystallites, the surface term dominates and the free energy increases. The free energy has a maximum at the critical cluster size n_{crit}

$$\Delta G(n_{crit}) = \frac{16\pi}{3}\frac{\gamma^3}{(\rho_s|\Delta\mu|)^2}, \tag{8.4}$$

where ρ_s is the number density of the solid. For larger sizes (smaller surface/volume ratio) the bulk term dominates and the free energy decreases. The crystal nucleation rate per unit volume is given by the product of the probability for the formation of a critical nucleus $P(n_{crit}) \propto \exp(-\Delta G(n_{crit})/k_BT)$ and a kinetic prefactor Γ

$$I = \Gamma\exp[-\Delta G(n_{crit})/k_BT]. \tag{8.5}$$

We stress that, whilst Eq. (8.4) is an approximation (based on classical nucleation theory), Eq. (8.5) is more generally valid. Below, we use simulations to estimate Γ and $\Delta G(n_{crit})$.

8.4.2 Nucleation barrier

The (Gibbs) free energy of a nucleus of size n is given by

$$\Delta G(n) = const - \ln[P(n)]. \tag{8.6}$$

To compute the equilibrium cluster size distribution $P(n)$ we used a biased Monte Carlo scheme in combination with a local bond-order analysis for the identification of crystal nuclei [48]. For the system with $R = 201nm$ we computed the crystal nucleation barrier at four different pressures $P\sigma^3/k_BT = 12.5, 13, 13.5$ and 14, corresponding to volume fractions of the liquid
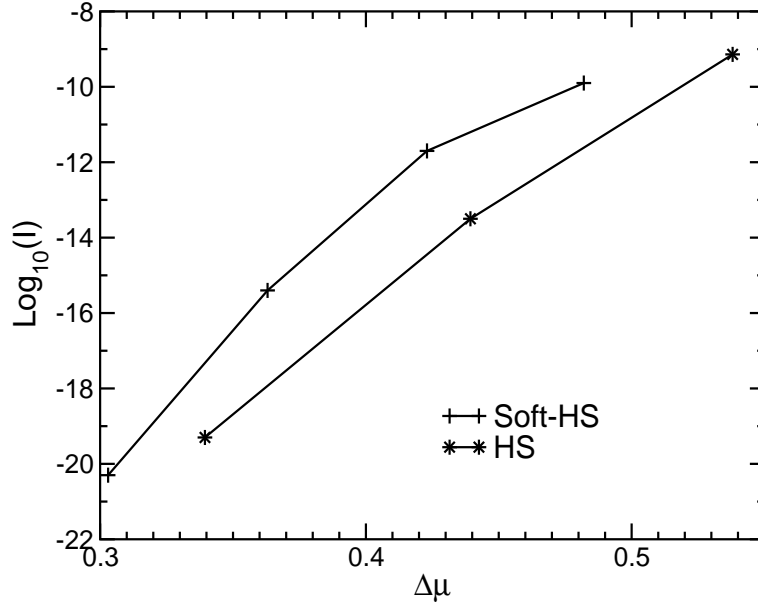
Figure 8.4: Results for the crystal nucleation rate for the slightly soft hard-sphere system compared to the pure hard-sphere as a function of supersaturation $\Delta\mu$.

$\rho_l = 0.43441, 0.43803, 0.44144$ and 0.44480. In Fig. 8.3 we show the results for the crystal nucleation barrier as a function of $\Delta\mu$. In the figure we also show the results for the hard-sphere system. As can be seen, despite the only slight softness, the crystal nucleation barrier is reduced by about $2 - 4k_BT$ at constant $\Delta\mu$, even though the colloidal particles are very nearly hard spheres.

8.4.3   Nucleation rate

To estimate the crystal nucleation rate we also need to compute the kinetic prefactor Γ. In reduced units, Γ has the following form $\Gamma = Z\rho_l f^+_{n_{crit}}(\sigma^5/D_0)$ [17]. Here $Z = [|\Delta G''(n_{crit})|/(2\pi k_BT)]^{1/2}$ is the Zeldovich factor which is a quantity that can be computed once the nucleation barrier is known. ρ_l is the number density of the liquid phase. The only unknown quantity is the reduced attachment rate of particles to the critical cluster $f^+_{n_{crit}}/D_0$, where D_0 is the diffusivity of colloids at infinite dilution. The attachment rate of particles to the critical cluster can be computed by measuring the size fluctuations around the critical size $f^+_{n_{crit}} = \langle (n(t) - n_{crit})^2 \rangle /t$ [48]. To compute this quantity we used a kinetic Monte Carlo scheme [26]. In such simulations the effect of hydrodynamic interactions between the particles is usually neglected. To correct for this we followed the approach proposed by Medina-Noyola [27]. In this scheme the computed $f^+_{n_{crit}}$ is multiplied by a factor D^S_S/D_0, where D^S_S is the short time self diffusion coefficient. For the hard-sphere system we could use the approximate expression $D^S_S/D_0 = (1 - \phi/0.64)^{1.17}$ [28]. In order to apply this expression to slightly-soft spheres, we used the rescaled volume fraction of the corresponding effective hard-sphere diameter. The results for the crystal nucleation rates as a function of $\Delta\mu$ are shown in Fig. 8.4. The decrease in the nucleation barrier transforms into an increase of the crystal nucleation rate of about two orders of magnitudes. In addition we show the crystal nucleation rate as a function of the rescaled volume fraction of the liquid (Fig. 8.5). In this figure too, an increase of the nucleation rate of more than one order of magnitude is observed. While this is significant it is not enough to account for the nucleation rates observed in experiments. Note that in our simulations we used a particle radius $R = 201nm$, which is the
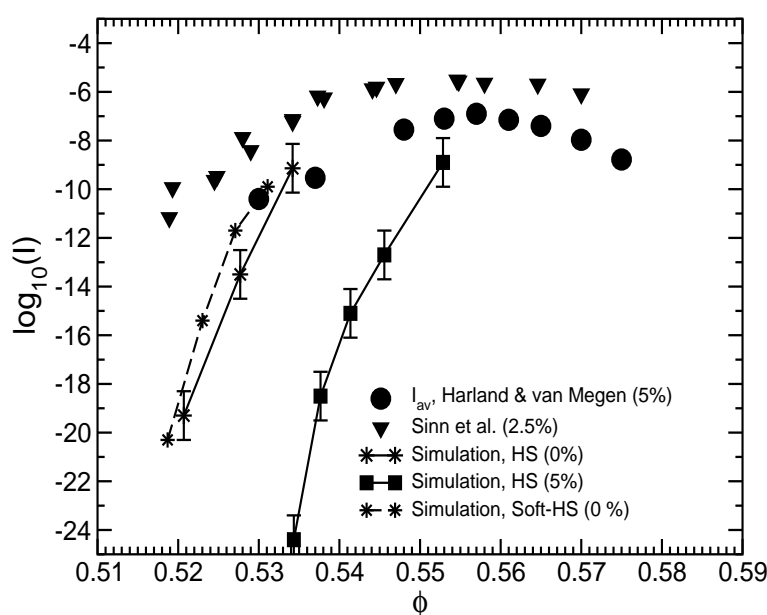
Figure 8.5: Comparison of the crystal nucleation rates computed for the slightly soft hard-spheres and the pure hard-spheres plotted as a function of the volume fraction of the liquid. The volume fraction used for the slightly soft hard-spheres correspond to the effective hard sphere model.

radius of the particles used in the experiments by Harland and van Megen [3]. A comparison to their results is possible if we assume that the effect of the softness on the nucleation rate is the same for particles that have a polydispersity of 5%. The agreement is only slightly better. We also show the results of experiments by Sinn et al. [35]. The particles they used are larger $R = 435\text{nm}$ (and therefore less soft) and have a polydispersity of 2.5%. If we extrapolate both experimental measurements to a monodisperse system, we see that a comparison to our results for the slightly soft system yields at best a discrepancy of four orders of magnitudes.

The fact that the particles are weakly charged and the system has a large Debye screening length might have two additional effects on the crystallization kinetics. First of all, the charge further lowers the surface free energy which increases the nucleation rates. Secondly, as both the surface charge and the Debye screening length may depend on density this can qualitatively change the dependence of the nucleation rate on supersaturation [89]. A better agreement with experimental nucleation rates would be obtained if we make the (not unreasonable) assumption that the colloids become more hard-sphere like at higher densities.

9

Wall induced crystallization in a hard-sphere system

We compute the free energy barrier associated with the formation of a crystal nucleus on a smooth hard wall. We find that the nucleation barrier is much smaller than in a homogeneous system. Spontaneous crystallization starts already for pressures that are about 5.4% higher than the estimated coexistence pressure. When crystal nuclei form, a (111) face crystal plane forms at the wall. Initially, this crystal grows laterally, rather than in the third dimension. The calculated free energy of a crystal nucleus that forms at the wall is about two orders of magnitudes lower than classical nucleation theory (CNT) estimates for the homogeneous system. Our simulations support theoretical estimates based on available data for the interfacial free energy. The presence of a nucleation barrier is incompatible with the assumption that the crystal phase wets the interface [90]

9.1   Introduction

Many liquids can be cooled far below the melting temperature and kept there without freezing [1]. This phenomena is known as undercooling. The reason why in the real world water usually freezes at $0°$ C is due to the presence of heterogeneous nucleation sites. In the case of undercooled water a single snowflake can induce the freezing process.

The reason why a liquid can be undercooled is best understood in the framework of classical nucleation theory (CNT). In CNT the free energy of a crystal nucleus that forms spontaneously in the supersaturated liquid is described by two competing terms. The first is a bulk term which describes the gain in free energy if n particles transform from the liquid to the solid state $n\Delta\mu$, where $\Delta\mu = \mu_l - \mu_s$ is the difference in chemical potential between the two phases. This term is opposed by the energy needed to create a liquid/solid interface $A\gamma$, where A is the surface area and γ the liquid/solid interfacial free energy density. Turnbull [91] extended CNT to the case of heterogeneous nucleation of a crystal that forms on a plane substrate. The difference with the homogeneous case is that there are now two interfaces present. The Gibbs free energy of a crystal containing n particles is given by:

$$\Delta G(n) = n\Delta\mu - A_{ws}(\gamma_{ws} - \gamma_{wl}) + A_{ls}\gamma_{ls}, \qquad (9.1)$$

where the indices w, l, s refer to the wall, liquid and solid. For a given value of n, the shape that minimizes $\Delta G(n)$ is a spherical vector, with a contact angle θ of the two phases with the wall
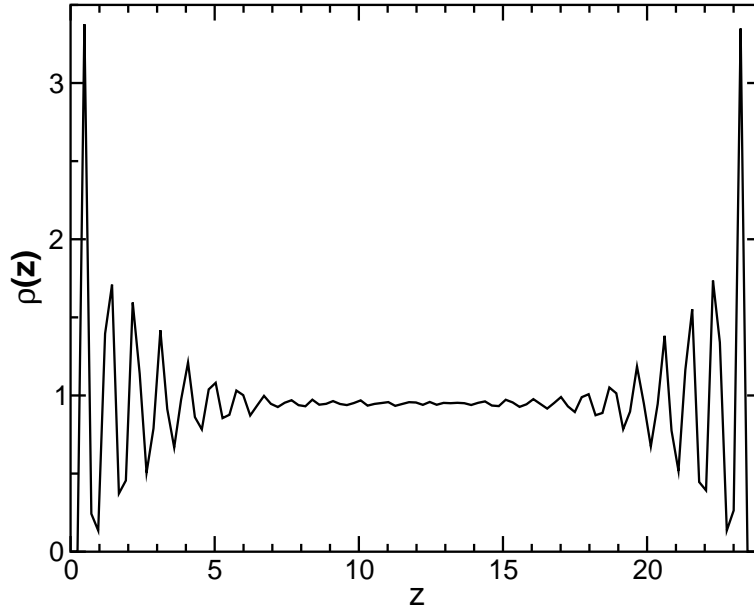
Figure 9.1: Calculated density profile of the particles between the two plane walls at a pressure P = 12.1 after 100000 trajectories.

given by:

$$\cos(\theta) = \frac{\gamma_{wl} - \gamma_{ws}}{\gamma_{ls}}. \tag{9.2}$$

The resulting height of the nucleation barrier is:

$$\Delta G^* = \frac{16\pi}{3} \frac{\gamma_{ls}^3 f(\theta)}{(\rho_s \Delta\mu)^2}, \tag{9.3}$$

where ρ_s is the number density of the bulk solid and the factor $f(\theta)$ is defined by

$$f(\theta) = \frac{(2 + \cos(\theta))(1 - \cos(\theta))^2}{4}. \tag{9.4}$$

Note that the only difference to the result for the homogeneous case is the factor $f(\theta)$. Depending on the values for the interfacial free energy densities and the resulting value for $\cos(\theta)$ we distinguish between three different cases. The first case is when $\cos(\theta) < -1$ (or $\theta > 180°$), which corresponds to the situation where $\gamma_{wl} - \gamma_{ws} < -\gamma_{ls}$. This implies that under these conditions the crystal will not form on the substrate, because this would increase its free energy. This situation is analog to homogeneous nucleation. The second case is when a finite contact value is seen: $-1 < \cos(\theta) < 1$ (or $0 < \theta < 180°$) with the following condition for the interfacial free energy densities $-\gamma_{ls} < \gamma_{wl} - \gamma_{ws} < \gamma_{ls}$. This means that a crystal lowers its free energy by attaching to the wall. This case is also referred to as partial wetting of the wall. The last case is when $\cos(\theta) = 1(\theta = 0°)$ or $\gamma_{ls} < \gamma_{wl} - \gamma_{ws}$. In this case the solid phase prefers to form a thin layer on the wall which is referred to as complete wetting. In that case the barrier to nucleation disappears.

In this chapter we investigate how the crystallization process in influenced by to the presence of a wall. In particular we focus on a system of colloidal hard-spheres between two planar hard walls. The hard-sphere system has the advantage that it is thermodynamically well characterized. Even more importantly, it can be studied experimentally. The estimated value
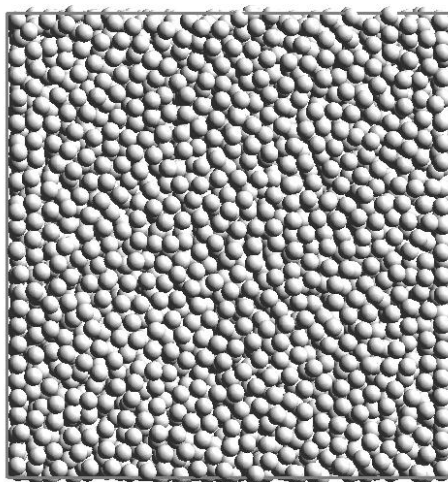
Figure 9.2: Snapshot of the configuration which shows the particles between the two plane walls at the end of these 100000 trajectories.

for the wall/liquid interfacial free energy density at the freezing volume fraction $\eta = 0.494$ is $\gamma_{wl} = 1.99 k_B T/\sigma^2$ [92], where σ is the hard-sphere diameter and $k_B T$ the thermal energy. The values for the wall/solid interfacial free energies for different orientations $(111), (110), (100)$ are estimated to be $\gamma_{ws} = 1.42, 3.08, 2.01 k_B T/\sigma^2$ [92]. The values for the liquid/solid interfacial free energy again for the three orientations in same order are $\gamma_{ls} = 0.58, 0.64, 0.62 k_B T/\sigma^2$ [6]. Based on these values we can speculate which of the three cases applies for the hard-sphere wall system. For the (110) plane we find that it prefers not to attach to the wall. The condition $\gamma_{wl} - \gamma_{ws} < -\gamma_{ls}$ is fulfilled $-1.09 < -0.64$. In contrast to that, the (100) and the (111) prefer to partially wet the wall. Both planes fulfill the corresponding condition $-\gamma_{ls} < \gamma_{wl} - \gamma_{ws} < \gamma_{ls}$ $(-0.62 < -0.02 < 0.62$ and $-0.58 < 0.57 < 0.58)$. We should note that the condition for wetting $\gamma_{ls} < \gamma_{wl} - \gamma_{ws}$ is almost fulfilled by the (111) plane $0.58 < 0.57$. Taking into account the statistical errors which might be present in the calculation of the interfacial free energy densities, the situation of partial wetting and complete wetting of the (111) plane is not completely clear. In fact, there are earlier simulations that report complete wetting [90] starting about 3% below the coexistence pressure. Clear evidence for surface freezing has been reported for a patterned surface. In this case, surface freezing already sets in 29% below the coexistence pressure [93].

Below we consider whether crystalline layers wet a plane wall below the bulk freezing density. We find that this is not the case. Next, we calculate the free energy of a nucleus that partially wets the wall and compare the measured barrier height to a prediction from CNT at this pressure in the corresponding homogeneous system.

9.2 Coexistence region

To explore the coexistence region we performed Monte Carlo simulations in the constant normal-pressure $(NP_\perp T)$ ensemble. Here N refers to the number of hard-spheres in our rectangular simulation box of size L_x, L_y, L_z. Periodic boundary conditions are applied in the x and y directions and two plane hard walls at distance L_z confining the system in the z direction. $P_\perp$ is the component of the stress tensor perpendicular to the plane wall, and T is the tempera-
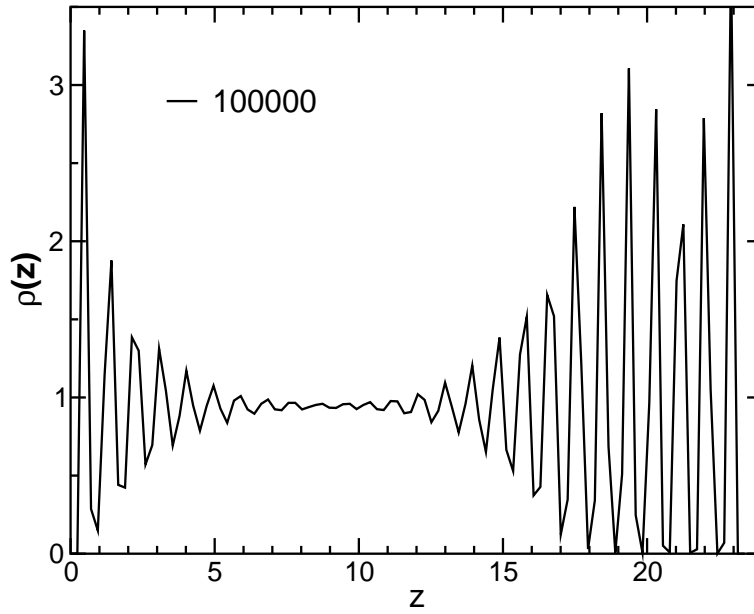
Figure 9.3: Calculated density profile of the particles between the two plane walls at a pressure $P = 12.2$ after 100000 trajectories. The system started to crystallize.

ture. As our unit of length we used the hard-sphere diameter σ, whereas T only sets the energy scale, but does not affect the phase transition. The hard-sphere system is completely specified by the volume fraction η of the system. The coexistence volume fractions for the bulk fluid and solid phase are known [33]: $\eta_f = 0.494$ and $\eta_m = 0.545$. The corresponding coexistence pressure is $P_{coex} = 11.57\sigma^3/k_BT$. In the following we always use reduced units. To avoid finite size effects we simulated a system containing $N = 13824$ particles. The wall area was fixed at $L_xL_y = 600.25\sigma^2$, the distance between the two walls in z direction fluctuated but was close to 24σ. The simplest way to detect prefreezing is to measure the density profile of the particles between the two walls. In case solid layers form at pressures lower than P_{coex}, this will be visible in the density profile through a pronounced dip, indicating a clear separation between crystal planes. However this was not observed, even at pressures higher than P_{coex}. In Fig. 9.1 we show the observed density profile at the end of a simulation performed at a pressure $P_\perp = 12.1$. The corresponding bulk volume fraction is $\eta = 0.4966$. In the simulation we performed 100000 trajectories, where one trajectory consists of 20 moves per particle, plus about 10 volume moves. A snapshot of the corresponding side view of the last configuration of this simulation is shown in Fig.9.2. The situation changes when the pressure was increased to $P_\perp = 12.2$. The liquid started to crystallize, which can be seen from the density profile shown in Fig.9.3. Already from these simulations it becomes clear that the liquid prefers to partially wet the wall rather than complete wetting. However the density region where the liquid does not crystallize spontaneously becomes very narrow. In the homogeneous system nucleation is very slow for $P < 17$ ($\eta < 0.53$). In addition we used a local bond-order analysis [48] to distinguish between particles with a liquid-like and solid-like local environment. The result of this analysis is shown in Fig.9.4, where we show a snapshot of the particles on the wall at pressure $P_\perp = 12.1$. The particles in blue have a liquid-like environment and the particles in yellow have a solid-like environment. Only some smaller crystal nuclei can be identified. We should note that solid cluster did only form at the wall and not in the bulk.
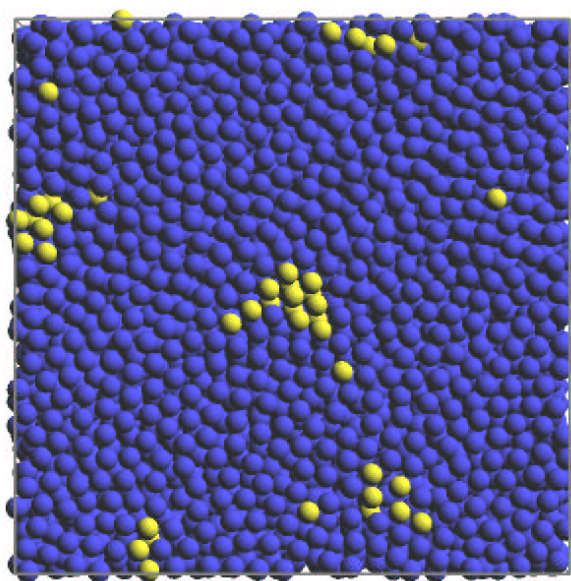
Figure 9.4: Snapshot of particles at the wall. A local bond-order analysis was used to distinguish between particles with a liquid-like (blue particles) and solid-like (yellow particles) environment. The snapshot is taken from a simulation at pressure P = 12.1.

9.3   Crystallization Barrier

Next, we computed the free energy of a small nucleus at the wall. According to thermodynamic fluctuation theory the (Gibbs) free energy of a nucleus of size n is given by [20]

$$\Delta G(n) = const - \ln[P(n)], \qquad (9.5)$$

where $P(n)$ is the equilibrium distribution of cluster sizes. This is the fundamental relation which enables us to compute the nucleation barrier in a simulation. We perform a Monte Carlo simulation in the constant normal-pressure $(NP_\perp T)$ ensemble in combination with a local-bond order analysis as described above. As for all but the smallest cluster $P(n) \ll 1$ we used umbrella sampling [22]. The total simulation was split into a number a number of smaller simulations, where each simulation was restricted to sample only a narrow range of cluster sizes. We used N = 13824 particles and simulated 100000 trajectories of same lenght as described before. The result for the free energy barrier calculated at a pressure $P_\perp = 12.1$ is shown in Fig. 9.5. The estimated barrier height is $\Delta G^* = 17 k_B T$ at a critical cluster size $n_{crit} = 150$. We can compare this estimate with a prediction for the barrier height in a homogeneous system. In an earlier publication we showed that given the correct value for the interfacial free energy CNT describes the barrier height quite well [48]. But we also found that the interfacial free energy depends on density. As the present system is close to coexistence we use its average coexistence value $\gamma = 0.61$ [6]. We then get $\Delta G^*_{CNT} = 1334 k_B T$ at a critical cluster size of $n_{crit} = 52000$. The overall reduction of the nucleation barrier due to the plane wall is about two orders of magnitudes. This should have dramatic consequences for colloidal hard-sphere systems. The colloidal suspension is usually prepared in a cylindrical container. The curvature of the cylinder is quite small so that one would expect that crystallization is always initiated by the wall. Finally we look closer with which plane the crystal nuclei attaches to the wall and what the actual shape is. In Fig. 9.6 and Fig. 9.7 we show a snapshot of a critical nucleus of size n = 150. We can clearly see that the (111) plane attaches to the wall, as expected. Note that the shape of the nucleus on the plane

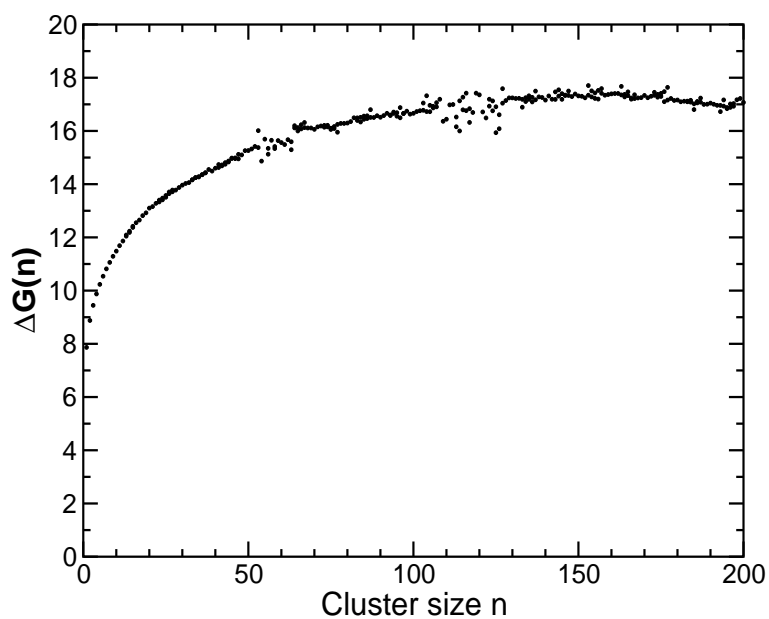Figure 9.5: Calculated nucleation barrier $\Delta G(n)$ of a crystal nucleus formed at the wall as a function of its size n.

is flat and the nucleus prefers to spread on the surface rather to grow in the bulk. This is in agreement with the CNT predictions based on the surface free energy values. The (111) partially wets the wall but the condition for complete wetting is almost fulfilled.

The fact that the range of metastability becomes very narrow might provide a powerful tool for the determination of the freezing density in experimental systems. The initial crystal formation at a flat surface can be observed using real space imaging. The corresponding density should differ less than 1% from the coexistence value.
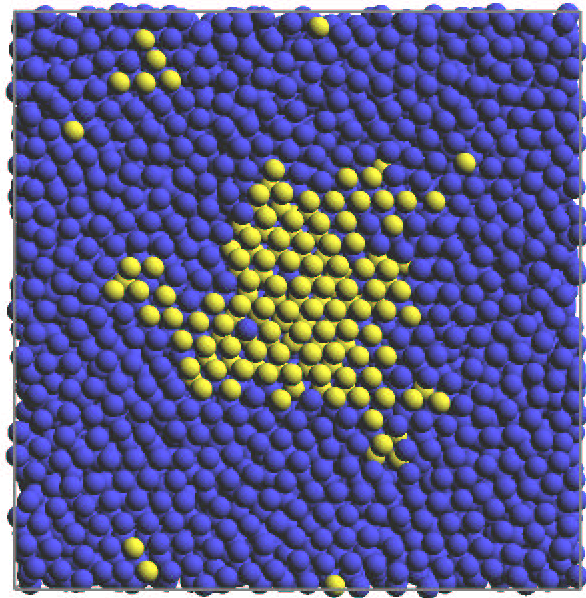
Figure 9.6: Snapshot of a crystal nucleus of size $n = 150$ shown in yellow. In the figure we displayed all solid particles in the system.
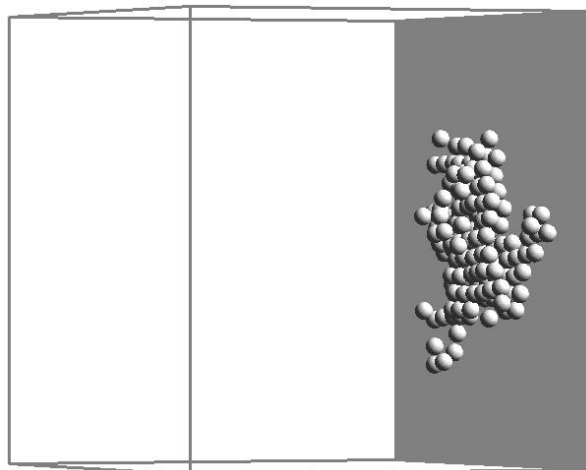

Figure 9.7: Snapshot of a crystal nucleus of size $n = 150$.

Bibliography

[1] FAHRENHEIT, D.B., 1724, *Phil. Trans. Roy. Soc.*, **39**, 78.

[2] TURNBULL, D. and FISCHER, J.C., 1949, *J. Chem. Phys.*, **17**, 71.

[3] HARLAND, J.L. and MEGEN, W.VAN , 1997, *Phys. Rev. E*, **55**, 3054.

[4] HEYMANN, A., STIPP, C., SINN, C., and PALBERG, T., 1998, *J. Coll. Interf. Sci.*, **206**, 119.

[5] PALBERG, T., 1999, *J. Phys.: Condens. Matter*, **11**, 323.

[6] DAVIDCHACK, R.L. and LAIRD, B.B., 2000, *Phys. Rev. Lett.*, **85**, 4751.

[7] FRENKEL, D. and SMIT, B., *Understanding Molecular Simulations: from Algorithms to Applications* (Academic Press, San Diego, 1996).

[8] CHANDLER, D., 1978, *J. Chem. Phys.*, **68**, 2959.

[9] RUIZ-MONTERO, M.J., FRENKEL, D., and BREY, J.J, 1997, *Mol. Phys.*, **90**, 925.

[10] GIBBS, J.W., 1876, *Trans. Connect. Acad.*, **3**, 108.

[11] GIBBS, J.W., *Scientific Papers Vol. I,II* (Longmans Green, London, 1906).

[12] VOLLMER, M. and WEBER, A., 1926, *Z. Phys. Chem.*, **119**, 227.

[13] FARUAS, L., 1927, *Z. Phys. Chem.*, **125**, 236.

[14] BECKER, R. and DÖRING, W., 1935, *Ann. Phys.*, **24**, 719.

[15] ZELDOVICH, J., 1942, *J. Expr. Theor. Phys. (Russia)*, **12**, 525.

[16] FRENKEL, J., *Kinetic Theory of Liquids* (Calendron, Oxford, 1946).

[17] KELTON, K.F., 1991, *Solid State Physics*, **45**, 75.

[18] WOLDE, P.R.TEN , Numerical Study of Pathways for Homogeneous Nucleation (available from: http://www.amolf.nl) Ph.D. thesis, University of Amsterdam, Amsterdam, The Netherlands, 1998.

[19] WOLDE, P.R.TEN , RUIZ-MONTERO, M.J., and FRENKEL, D., 1996, *Faraday Discuss.*, **114**, 9932.

[20] LANDAU, L.D. and LIFSHITZ, E.M., *Statistical Physics* (Pergamon Press, Oxford, 1969).

[21] REISS, H. and BOWLES, R.K., 1999, *J. Chem. Phys.*, **111**, 7501.

[22] TORRIE, G.M. and VALLEAU, J.P., 1974, *Chem. Phys. Lett.*, **28**, 578.

[23] GEYER, C.J. and THOMPSON, E.A., 1995, *J. Am. Stat. Assoc.*, **90**, 909.

[24] PRESS, W.H., TEUKOLSKY, S.A., VETTERLING, W.T., and FLANNERY, B.P., *Numerical Recipies* (Cambridge University Press, Cambridge, 1992).

[25] WOLDE, P.R.TEN , RUIZ-MONTERO, M.J., and FRENKEL, D., 1999, *J. Chem. Phys.*, **110**, 1591.

[26] CICHOCKI, B. and HINSON, K., 1990, *Physica A*, **166**, 473.

[27] MEDINA-NOYOLA, M., 1988, *Phys. Rev. Lett.*, **60**, 2705.

[28] DUIJNEVELDT, J.S.VAN and LEKKERKERKER, H.N.W., *Science and Technology of Crystal Growth* (edited by J. P. van der Eerden and O. S. L. Bruinsma, Kluwer-Academic, Dordrecht, 1995).

[29] SCHÄTZEL, K. and ACKERSON, B.J., 1993, *Phys. Rev. E*, **48**, 3766.

[30] CHENG, Z., Colloidal Hard Sphere Crystallization and Glass Transition Ph.D. thesis, Pinceton University, Princeton, US, 1998.

[31] ZHU, J. ET AL., 1997, *Nature*, **387**, 883.

[32] DUIJNEVELDT, J.S.VAN and FRENKEL, D., 1992, *J. Chem. Phys.*, **96**, 4655.

[33] HOOVER, W.G. and REE, F.H., 1968, *J. Chem. Phys.*, **49**, 3609.

[34] HALL, K.R., 1970, *J. Chem. Phys.*, **57**, 2252.

[35] SINN, C., HEYMANN, A., STIPP, A., and PALBERG, T., 2001, *Progr Coloid Polym Sci*, **118**, 266.

[36] OSTWALD, W., 1897, *Z. Phys. Chem.*, **22**, 289.

[37] ALEXANDER, S. and MCTAGUE, J.P., 1978, *Phys. Rev. Lett.*, **41**, 702.

[38] KLEIN, W. and LEYVRAZ, F., 1986, *Phys. Rev. Lett.*, **57**, 2845.

[39] GROH, B. and MULDER, B.M., 1999, *Phys. Rev. E*, **59**, 5613.

[40] BOLHUIS, P.G., FRENKEL, D., MAU, S.C., and HUSE, D.A., 1997, *Nature*, **388**, 235.

[41] PUSEY, P.N. ET AL., 1989, *Phys. Rev. Lett.*, **63**, 2753.

[42] PRONK, S. and FRENKEL, D., 1999, *J. Chem. Phys.*, **110**, 4589.

[43] MAU, S.C. and HUSE, D.A., 1999, *Phys. Rev. E*, **59**, 4396.

[44] POLSON, J. M., TRIZAC, E., PRONK, S., and FRENKEL, D., 2000, *J. Chem. Phys.*, **112**, 5339.

[45] PUSEY, P.N., *Les Houches; Liquids, Freezing and Glass Transition* (edited by J.P. Hansen, D. Levesque, and J. Zinn-Justin, North-Holland, Amsterdam, 1991).

[46] KOFKE, D.A. and BOLHUIS, P.G., 1996, *Phys. Rev. E*, **54**, 634.

[47] KOFKE, D.A. and BOLHUIS, P.G., 1999, *Phys. Rev. E*, **59**, 618.

[48] AUER, S. and FRENKEL, D., 2001, *Nature*, **409**, 1020.

[49] OXTOBY, D.W. and KASHCHIEV, D., 1994, *J. Chem. Phys.*, **100**, 7665.

[50] SHI, F.G., TONG, H.Y., and AYERS, J.D., 1995, *Appl. Phys. Lett.*, **67**, 350.

[51] WOLDE, P.R.TEN and FRENKEL, D., 1997, *Science*, **277**, 1975.

[52] GASSER, U., WEEKS, E.R., SCHOFIELD, A., PUSEY, P.N., and WEITZ, D.A., 2001, *Science*, **292**, 258.

[53] PUSEY, P.N. and MEGEN, W.VAN , 1986, *Nature*, **320**, 340.

[54] OXTOBY, D., 2001, *Nature*, **413**, 694.

[55] DHONT, J.K.G., SMITS, C., and LEKKERKERKER, H.N.W., 1992, *J. Coll. Interf. Sci.*, **152**, 386.

[56] SCHÖPE, H.J. and PALBERG, T., 2001, *Progr Colloid Polym Sci*, **118**, 82.

[57] VERWEIJ, E.J.W. and OVERBEEK, J.TH.G., *Theory of the Stability of Lyophilic Colloids* (Elsevier, NY, 1948).

[58] ALEXANDER, S. ET AL., 1984, *J. Chem. Phys.*, **80**, 5776.

[59] BITZER, F., PALBERG, T., LÖWEN, H., SIMON, R., and LEIDERER, P., 1994, *Phys. Rev. E*, **50**, 2821.

[60] AZHAR, F.EL., BAUS, M., RYCKAERT, J.P., and MEIJER, E.J., 2000, *J. Chem. Phys.*, **112**, 5121.

[61] MEIJER, E.J. and FRENKEL, D., 1991, *J. Chem. Phys.*, **94**, 2269.

[62] ELLIOT, M.S., HADDON, S.B., and POON, W.C.K., 2001, *J. Phys.: Condensed Matter*, **13**, 553.

[63] OKUBO, T., OKADA, S., and TSUCHIDA, A., 1997, *J. Coll. Interf. Sci.*, **189**, 337.

[64] OKUBO, T. and OKADA, S., 1997, *J. Coll. Interf. Sci.*, **192**, 490.

[65] OKUBO, T., TSUCHIDA, A., and KATO, T., 1999, *Colloid and Polymer Sci*, **277**, 191.

[66] SCHÖPE, H.J., Physikalische Eigenschaften kolloidaler Festkörper Ph.D. thesis, Johannes Gutenberg Universität Mainz, Mainz, Germany, 2000.

[67] SCHÖPE, H.J. and PALBERG, T., 2002, *J. Noncryst. Mat. accepted*,

[68] STRANSKI, I.N. and TOTOMANOW, D., 1933, *Z. Phys. Chem.*, **163**, 399.

[69] WOLDE, P. R.TEN , RUIZ-MONTERO, M.J., and FRENKEL, D., 1995, *Phys. Rev. Lett.*, **75**, 2714.

[70] AUER, S. and FRENKEL, D., 2001, *Nature*, **413**, 711.

[71] LÖWEN, H., PALBERG, T., and SIMON, R., 1993, *Phys. Rev. Lett.*, **70**, 1557.

[72] BLAADEREN, A.VAN , PEETERMANS, J., MARET, G., and DHONT, J.K.G., 1992, *J. Chem. Phys.*, **96**, 4591.

[73] HOOGENBOOM, J. and BLAADEREN, A.VAN , 2002, *J. Phys. Chem. submitted*,

[74] COSTELLO, B.A.DE and LUCKHAM, P.F., 1993, *J. Coll. Interf. Sci.*, **156**, 72.

[75] COSTELLO, B.A.DE , LUCKHAM, P.F., and TADROS, TH.F., 1992, *Langmuir*, **8**, 464.

[76] VRIJ, A. ET AL., 1983, *Faraday Discuss. chem. Soc.*, **76**, 19.

[77] BLAADEREN, A.VAN and WILTZUIS, P., 1995, *Science*, **270**, 1177.

[78] RUTGERS, M.A., DUNSMUIR, J.H., XUE, J.Z., RUSSEL, W.B., and CHAIKIN, P.M., 1995, *prb*, **53**, 5043.

[79] ALEXANDER, S., 1977, *J. Phys. (Paris)*, **38**, 983.

[80] GENNES, DE P.G., 1988, *Adv. Colloid Interface Sci.*, **27**, 189.

[81] RUSSEL, W.B., SAVILLE, D.A., and SCHOWALTER, W.R., *Colloidal Dispersions* (Cambridge University Press, Cambride, 1989).

[82] ANTL, L. ET AL., 1986, *Colloids Surf.*, **17**, 67.

[83] MEWIS, J., FRITH, W.J., STRIVENS, T.A., and RUSSEL, W.B., 1989, *A.I.Ch.E.J.*, **35**, 415.

[84] CAIRNS, R.J.R., OTTEWILL, R.H., OSMOND, D.J.W., and WAGSTAFF, I., 1976, *J. Colloid Interface Sci.*, **54**, 51.

[85] DOROSZKOWSKI, A. and LAMBOURNE, R., 1971, *J. Polym. Sci. C*, **34**, 253.

[86] MEGEN, W.VAN and UNDERWOOD, S.M., 1990, *Langmuir*, **6**, 35.

[87] MARKOVIC, I., OTTEWILL, R.H., and UNDERWOOD, S.M., 1986, *Langmuir*, **2**, 625.

[88] CEBULA, D.J., GOODWIN, J.W., OTTEWILL, R.H., and JENKIN, J. G. ANDTABONY, 1983, *Colloid Polymer Sci.*, **261**, 555.

[89] AUER, S. and FRENKEL, D., 2002, *J. Phys.: Condens. Matter*, **14**, 7667.

[90] COURTEMANCHE, D.J. and SWOL, F.VAN , 1992, *Phys. Rev. Lett.*, **69**, 2078.

[91] TURNBULL, D., 1950, *J. Chem. Phys.*, **18**, 198.

[92] HENI, M. and LÖWEN, H., 1999, *Phys. Rev. E*, **60**, 7057.

[93] HENI, M. and LÖWEN, H., 2000, *Phys. Rev. Lett.*, **85**, 3668.

Summary

In this thesis we simulate the crystal nucleation process in a colloidal dispersion of spherical particles with purely repulsive interaction. The main problem when studying crystal nucleation, experimentally as well as in computer simulations, is that crystal nucleation is an activated process. First, small crystal nuclei need to form spontaneously in a supersaturated solution, but unless their size exceeds a critical value, they will redissolve rather than grow. The crystal nucleation rate is the product of the probability for the formation of a critical cluster and a kinetic prefactor that describes the rate with which a critical nucleus grows. Our simulation techniques enable us to overcome this problem and to predict absolute crystal nucleation rates. In addition we are able to study the pathway for the formation of small crystal nuclei.

In chapter 2 we begin with a general introduction to how molecular simulations can be used for the calculation of a reaction rate constant. This is done in the framework of linear response theory. We focus on the main results for the reaction rate constant and the practical aspects of the numerical calculation. This formulation is applied to the special case where the barrier crossing is diffusive. The final result is applicable to the calculation of a crystal nucleation rate.

Chapter 3 summarizes classical nucleation theory (CNT) which is most commonly used to predict nucleation rates. We explicitly demonstrate that the expression for the nucleation rate is identical to that derived in chapter 2. Furthermore, we extend the formulation of CNT to a multicomponent system.

We end the first part of the thesis with chapter 4, which provides an introduction to the numerical techniques needed to predict a crystal nucleation rate. The calculation of the rate is split into two parts. First we compute the nucleation barrier and second we compute the kinetic prefactor. In all cases we perform Monte Carlo simulations, in combination with a local bond order analysis for the identification of solid particles, for the calculation of the nucleation barrier. As the formation of cluster is extremely rare we need to use umbrella sampling. The kinetic prefactor must be calculated in a separate kinetic Monte Carlo simulation.

In the second part we apply our novel techniques to colloidal dispersions of spherical particles with purely repulsive interaction. As crystallization of hard-sphere colloids has been extensively studied, this system was an obvious choice to begin with (chapter 5). This study constitutes the first example where computer simulations of crystal nucleation rates are directly compared with experiments. To our surprise, we find that our results are at odds both with the existing experiments and with CNT. We state explicitly that, according to our estimates, the computed nucleation rates are accurate to within one order of magnitude. The discrepancy with experiments must therefore be attributed to problems in the experimental data analysis. In addition we find that CNT underestimates the nucleation barrier by about 50%. Based on our barrier calculations and a precise knowledge of $\Delta\mu$ (the difference in chemical potential between the liquid and the solid phases) we deduce the liquid solid surface free energy γ for a critical nucleus. We find that these estimates for γ are much higher than the coexistence value, and γ increases with density. The dependence of γ on density was not considered in existing theories. Hence, our work poses a challenge to experimentalists and theoreticians alike. We should also

note that our calculations for the kinetic prefactor are in good agreement with a simple classical estimate. Finally, we study the structure of critical nuclei. It is known that the stable crystal structure is face centered cubic (fcc). However we find that our critical cluster constitutes a random stacking of the (111) planes of the fcc and the hexagonal closed packed (hcp) structure. This is in agreement with experimental observations and in contrast to a theoretical prediction that a fluid always crystallizes via a body centered cubic (bcc) intermediate. It can be seen as a manifestation of Ostwald's step rule, that a liquid first nucleates in a metastable structure and only later transforms to the stable one.

In practice, the colloidal particles used in the experiments have a distribution of particle radii (referred to as polydispersity) which is rarely less than $2-3\%$ of the average radius. In order to compare our measured nucleation rates with experiments we already needed to study the effect of a small polydispersity (up to 5%) in the previous chapter. The result was that within numerical error the monodisperse and polydisperse suspensions have the same nucleation barrier at constant supersaturation $\Delta\mu$. However, experiments on hard-sphere colloids indicate that crystallization is suppressed if the polydispersity exceeds 12%. So far this has been attributed to kinetic reasons as crystallization of highly polydisperse suspensions is not excluded on thermodynamic grounds. This observation was the motivation for our second project where we further studied the crystallization kinetics for polydispersities up to 10% (chapter 6). Our calculations of the crystal nucleation barrier show that when polydispersity is increased beyond 5%, the barrier height increases rapidly at constant $\Delta\mu$. This means that the probability for the formation of a critical nucleus is decreased and crystal nucleation is suppressed. According to CNT this increase in the barrier height is attributed to an increase of γ with polydispersity. Even more surprising is that the variation of the barrier height with supersaturation at the same polydispersity is non-monotonic. With increasing $\Delta\mu$ the barrier height first decreases then goes through a minimum and starts to increase again. Again, using the equation for the barrier height from CNT, this observation is attributed to an increase of γ with $\Delta\mu$. The minimum of the barrier height increases rapidly with polydispersity. Our estimate for the minimum barrier height of a system of hard-sphere colloids with a polydispersity of 10% is about $30k_BT$. This implies that for a suspension of colloids with a radius of $500nm$ we expect to see less than one crystallite per cubic centimeter. This has important implications for the morphology of polycrystalline colloidal materials. Vitrification at high supersaturations should yield colloidal glasses that are truly amorphous, rather than nano-crystalline. Finally we propose how our observation of the minimum in the nucleation barrier can be tested experimentally. Using a simple analysis we show that the minimum barrier height causes a minimum in the typical crystallite size at the end of a nucleation experiment. By visual inspection one can test if crystallites formed at high supersaturation are larger than those that form at lower supersaturation.

During the course of the work described above a new experiment was reported, where nucleation and growth in colloidal crystallization were studied by real-space imaging. The reported nucleation rates are much higher, and an estimate for the surface tension was much lower than the values we found in our simulations. The difference between this system and ours is that the particles were weakly charged. This inspired our next project, the crystallization of weakly charged colloidal spheres (chapter 7). We model the interaction between the charged colloids with a repulsive hard-core Yukawa potential. We study the dependence of the crystal nucleation rate as a function of supersaturation on the range and the contact value (charge on the sphere) of the interaction potential. We find that at the same volume fraction crystallization of the weakly charged spheres is much faster than for hard-spheres. This is partly due to the fact that the fluid-solid coexistence of the charged spheres occurs at lower volume fractions, which implies a higher supersaturation. In addition, we find that the charge has a strong direct effect on the nucleation barrier by lowering γ. This effect is strongest when only a weak charged is

added. Furthermore we find that the functional dependence of the barrier height as a function of supersaturation does not change considerably for different charges. This is in contrast to the experiment where only a slight dependence of the nucleation rate on supersaturation is observed. Our simulations indicate that one possible explanation is a strong density dependence of the interaction potential. Moreover, we study the structure of small crystal nuclei. All simulations are performed in a region of the phase diagram where fcc is the stable phase. However in all cases we find that the initial crystal nuclei have a bcc structure. We attribute this effect to the fact that the liquid/bcc surface free energy is lower than that of the liquid/fcc interface.

Colloids that consist of a polymethylmethacrylate (PMMA) core coated with a thin layer of poly-12-hydroxystearic (PHSA) are commonly used as a model system for hard spheres. However, due to the coating, the particles are slightly soft. In chapter 8 we study the effect that such a softness has on the phase behavior and the crystallization kinetics. In our simulations we use an interaction potential extracted from surface force measurements on that system. This potential is characterized by two parameters, the thickness and the density of the PHSA layer. We find that the freezing density measured in the experiments corresponds to a layer thickness that is about a factor two larger than the thickness measured in the surface force experiment. We suggest that this discrepancy might be due to a slight charge on the particles. Based on a comparison between the experimental and numerical results we can estimate the magnitude this charge would need to have. The charge is indeed very small (less than one electron per sphere). For the crystallization kinetics we find that the nucleation rate is increased by two orders of magnitudes at constant $\Delta\mu$. While this is significant, it cannot account for the discrepancy between the nucleation rates observed in experiments and simulations (chapter 5).

Finally we apply our techniques to study crystal nucleation in a heterogeneous system. We simulate a system of hard spheres that are confined between two plane hard walls. We find that the presence of the walls narrows the density regime where the liquid is metastable with respect to the solid. Already at volume fractions less than 1% higher than coexistence spontaneous crystallization occurs, compared to about 4% in the homogeneous system. We see that the wall induces the crystal formation. First a (111) face crystal plane forms at the wall. Then it prefers to grow laterally rather than in the third dimension. The calculated barrier height of such a nucleus is about two orders of magnitude lower than an estimate based on CNT in the corresponding homogeneous system. Our simulations support arguments based on the values of the surface free energy densities which suggest that a crystal should partially wet the wall with the (111) plane. We propose that the fact that crystal formation happens at volume fractions less than 1% higher than coexistence can be used for a precise determination of the freezing point in the experimental system.

Samenvatting (Summary in Dutch)

Dit proefschrift gaat over kristalnucleatie in colloïdale dispersies van bolvormige deeltjes met repulsieve interacties. Het grootste probleem bij de bestudering van nucleatie, zowel in experimenten als in computersimulaties, is dat nucleatie een geactiveerd proces is. De eerste stap in dit proces is het spontaan vormen van een kleine kiem in de oververzadigde oplossing. Wanneer deze kiem kleiner is dan een bepaalde kritische grootte zal de kiem oplossen in plaats van groeien. De nucleatiesnelheid is het product van de kans dat zich een kritische kiem vormt en een kinetische factor die de snelheid beschrijft waarmee de kritische kiem groeit. Met behulp van de in dit proefschrift beschreven computersimulaties is het mogelijk dit probleem op te lossen en zo de absolute nucleatiesnelheid te berekenen. Daarnaast is het mogelijk om het mechanisme waarmee een kritische kiem groeit te bestuderen.

In hoofdstuk 2 wordt een algemene manier besproken om reactiesnelheden met behulp van computersimulaties te bepalen. Deze methode maakt gebruik van lineaire respons theorie. In de beschrijving hiervan wordt met name gekeken naar de berekening van de reactiesnelheid en naar de praktische aspecten van de numerieke berekening. Deze methodologie wordt toegepast op het speciale geval van een diffusieve reactie, hetgeen ons in staat stelt om de absolute nucleatiesnelheid te berekenen.

Hoofdstuk 3 bevat een samenvatting van de klassieke nucleatie theorie (CNT: Classical Nucleation Theory). Deze theorie wordt het meest gebruikt voor de berekening van nucleatiesnelheden. We laten zien dat de CNT dezelfde formule oplevert voor de berekening van de nucleatiesnelheid als de formule die in hoofdstuk 2 is afgeleid. Tevens wordt een beschrijving gegeven van de CNT in het geval van een systeem dat bestaat uit meerdere componenten.

Het eerste deel van dit proefschrift word afgesloten met een beschrijving van de numerieke technieken die gebruikt worden bij de berekening van de nucleatiesnelheid. De simulatie bestaat uit twee componenten: de eerste component is de berekening van de nucleatiebarrière en de tweede component is de berekening van de kinetische factor. Beide berekeningen worden uitgevoerd met behulp van Monte Carlo simulaties waarbij gebruik wordt gemaakt van local bond order analyses om een kristal kiem te identificeren. Omdat de vorming van deze kiemen maar zelden plaats vindt tijdens een simulatie, gebruiken we umbrella sampling. De kinetische factor wordt berekend in een aparte, kinetische Monte Carlo simulatie.

In het tweede gedeelte van dit proefschrift worden deze nieuwe technieken toegepast op colloïdale dispersies van bolvormige deeltjes met repulsieve interacties. In eerste instantie hebben we ervoor gekozen te kijken naar een harde bollen systeem, omdat kristallisatie van harde bollen al uitgebreid bestudeerd is (hoofdstuk 5). Deze computersimulaties zijn de eerste waarmee nucleatiesnelheden direct kunnen worden vergeleken met experimentele waarden. Tot onze verrassing kwamen de berekende waarden niet overeen met de CNT en met experimentele waarden. Bovendien zijn de berekende nucleatiesnelheden, volgens onze afschattingen, tot op ordegrootte nauwkeurig. Het verschil met de experimentele data moet dan ook worden toegeschreven aan problemen bij het analyseren van de experimenten. Tevens voorspelt de CNT een nucleatiebarrière die 50% lager is dan de door ons berekende waarde. Met behulp van de

grootte van de nucleatiebarrière en het verschil in chemische potentiaal tussen het kristal en de vloeistof (oververzadiging) is de oppervlaktespanning tussen vaste stof en vloeistof berekend. Het bleek dat de oppervlaktespanning veel hoger is dan in het geval van chemisch evenwicht tussen de twee fases. Bovendien hing de oppervlaktespanning sterk af van de dichtheid. In de bestaande theorieën over kristalnucleatie is geen afhankelijkheid van de dichtheid op de oppervlaktespanning opgenomen. Onze resultaten zijn daarom ook voor experimentatoren en theoretici interessant. Een ander belangrijk punt is dat de berekende kinetische factor wel goed overeenstemt met het klassieke resultaat. Tenslotte hebben we ook de structuur van de kritische kiem bestudeerd. Het is bekend dat de meest stabiele kristalstructuur fcc (face centered cubic) is. Echter, onze bevinding is dat de kritische kiem bestaat uit willekeurige stapelingen van zowel het (111) vlak van de fcc structuur als de hcp (hexagonal close packed) structuur. Dit is in overeenstemming met experimenten maar in tegenspraak met eerdere theoretische voorspellingen dat een vloeistof altijd stapsgewijs kristalliseert met een bcc structuur als tussenfase. Dit kan worden gezien als een voorbeeld van de Ostwald step rule die voorspelt dat een vloeistof eerst een metastabiele toestand vormt alvorens te kristalliseren tot een stabiele structuur.

De colloïdale deeltjes die gebruikt worden in experimenten hebben een verdeling in de straal van de deeltjes die meestal meer is dan $2 - 3\%$ van het gemiddelde. Om onze berekende kristalgroeisnelheid te kunnen vergelijken met experimenten is het belangrijk om het effect van lage polydispersiteit (kleiner dan 5%) te bestuderen. Het bleek dat voor deze lage polydispersiteit de nucleatiebarrière gelijk is aan die voor harde bollen bij identieke oververzadiging. Echter, experimenten met colloïden duiden erop dat kristallisatie onderdrukt wordt wanneer de polydispersiteit groter is dan 12%. Tot nu toe werd dit toegeschreven aan de kinetische factor aangezien deeltjes met een hoge polydispersiteit volgens de thermodynamica wel degelijk kunnen kristalliseren. Dit motiveerde ons om de kristallisatiesnelheid voor deeltjes met een polydispersiteit groter dan 5% te onderzoeken (hoofdstuk 6).

Onze berekeningen laten zien dat de nucleatiebarrière als functie van de oververzadiging snel groter wordt zodra de polydispersiteit toeneemt boven de 5%. Dit betekent dat de kans op vorming van een kritische kiem afneemt en dat kristalnucleatie onderdrukt wordt. Volgens de CNT moet het groter worden van de nucleatiebarrière worden toegeschreven aan het groter worden van de oppervlaktespanning. Nog spectaculairder is dat de nucleatiebarrière als functie van de oververzadiging niet monotoon is. Bij toenemende oververzadiging wordt de barrière in eerste instantie lager om vervolgens weer te stijgen. Ook dit moet volgens de CNT worden toegeschreven aan een veranderende oppervlaktespanning. De minimale hoogte van de nucleatiebarrière neemt snel toe met de toenemende polydispersiteit. De minimale barrière voor systemen met een polydispersiteit van 10% is ongeveer $30\,k_BT$. Dit betekent dat voor colloïdale suspensies met een gemiddelde deeltjesdiameter van ongeveer $500\,nm$ er gemiddeld minder dan 1 kristalliet is per kubieke centimeter. Dit heeft belangrijke gevolgen voor de morfologie van polykristallijne colloïdale materialen. Vitrificatie bij hoge oververzadiging zou moeten resulteren in colloïdale glazen die volledig amorf zijn in plaats van nano-kristallijn. Tenslotte voorspellen we hoe het minimum van de nucleatiebarrière experimenteel zou kunnen worden waargenomen: Met een simpele analyse laten we zien dat de minimale barrière resulteert in een minimum van de kristalliet grootte aan het einde van een nucleatie-experiment. Vervolgens kan men met optische methoden testen of de kristallieten die gevormd zijn bij hogere oververzadiging groter zijn dan die die gevormd zijn bij lagere oververzadiging.

Tijdens het in dit proefschrift beschreven onderzoek werd in de literatuur een experimentele studie gerapporteerd, waarin nucleatie en groei van colloïdale kristallen in de reële ruimte werd bestudeerd met behulp van confocale microscopie. Vergeleken met de computersimulaties was de gemeten nucleatiesnelheid veel hoger en de oppervlaktespanning veel lager. Een essentieel verschil met de simulaties was dat de deeltjes in het experiment een kleine lading hadden.

Dit inspireerde ons om het gedrag van geladen colloïdale deeltjes te onderzoeken (hoofdstuk 7). Het model dat we hiervoor hebben gebruikt is de repulsieve harde-bollen Yukawa potentiaal. Hiervoor hebben we de kristallisatiesnelheid bestudeerd als functie van de mate van oververzadiging en de lading van de colloïden. Het blijkt dat bij dezelfde volumefractie zwak geladen colloïden veel sneller kristalliseren dan harde bollen. Dit komt gedeeltelijk doordat het vaste stof/vloeistof evenwicht van zwak geladen colloïden plaats vindt bij lagere volumefracties. Dit impliceert een hogere oververzadiging. Een ander effect is dat de lading direct van invloed is op de nucleatiebarrière door een verlaging van de oppervlaktespanning. Dit effect is vooral aanwezig wanneer slechts zwak geladen colloïden worden gebruikt. Bovendien blijkt de vorm van de barrière als functie van de oververzadiging vrijwel onafhankelijk van de lading. Dit is in tegenspraak met het eerdergenoemde experiment waarin slechts een kleine afhankelijkheid van de oververzadiging op de nucleatiesnelheid werd waargenomen. Onze simulaties suggereren dat in het experiment de interactiepotentiaal sterk afhankelijk is van de dichtheid. Tevens is de kristalkiem in de simulatie erg klein. Alle simulaties zijn uitgevoerd in het gebied van het fasediagram waarin de fcc structuur de stabiele fase is. Echter, in alle simulaties heeft de initiële kristalkiem een bcc structuur. Dit kan worden toegeschreven aan het feit dat de vrije energie van een bcc/vloeistof oppervlak lager is dan die van een fcc/vloeistof oppervlak.

Colloïden bestaande uit een polymethylmethacrylaat (PMMA) kern gecoat met een dunne laag poly-12-hydroxystearic (PHSA) zijn een veel gebruikt experimenteel modelsysteem voor harde bollen. Echter, door de coating zijn deze deeltjes niet geheel hard. In hoofstuk 8 bestuderen we het effect van een zachte potentiaal op de kristallisatiesnelheid. In de simulaties hebben we een interactiepotentiaal gebruikt die afkomstig is van oppervlakte-kracht metingen. Deze potentiaal kan worden gekarakteriseerd met twee modelparameters: de dikte en de dichtheid van de PHSA laag. Uit deze experimenten volgt dat de dichtheid bij de kristallisatie-overgang overeenkomt met een laagdikte die een factor twee groter is dan de laagdikte gemeten in het oppervlakte-kracht experiment. Een mogelijke oorzaak hiervoor is dat de deeltjes een kleine lading hebben. Door de experimentele en numerieke resultaten te vergelijken is het mogelijk een ruwe schatting te maken voor de grootte van deze lading. Het blijkt dat de lading per bol kleiner is dan een enkele elektron per bol. De kristallisatiesnelheid is twee ordegroottes groter bij een constant verschil in chemische potentiaal tussen de vloeistof en vaste fase. Hoewel dit een significant verschil is, is het niet mogelijk om hiermee het verschil in kristallisatiesnelheid tussen experiment en simulatie te verklaren (hoofstuk 5).

Tenslotte hebben we onze technieken toegepast op kristalnucleatie in een heterogeen systeem, te weten harde bollen tussen twee harde wanden. Onze bevinding is dat de aanwezigheid van harde wanden het regime waarin de vloeistof metastabiel is ten opzichte van de vaste stof verkleint. Reeds bij een volumefractie die minder dan 1% hoger is dan de evenwichtswaarde vindt spontane kristallisatie plaats, in vergelijking met 4% voor een homogeen systeem. Het is duidelijk dat de harde wand kristallisatie bevordert. Tijdens kristallisatie word allereerst een (111) kristalvlak op de wand gevormd. Vervolgens heeft het systeem een voorkeur om in de laterale richting te groeien in plaats van loodrecht op de harde wand. De berekende nucleatiebarrière is twee ordegroottes lager dan een schatting gebaseerd op de CNT voor het corresponderende homogene systeem. Deze simulaties vormen een ondersteuning voor argumenten die gebaseerd zijn op de waarden voor de oppervlakte vrije energie dichtheid welke suggereren dat het kristal de harde wand gedeeltelijk met een (111) vlak zou bedekken. Wij stellen dat de waarneming dat kristalvorming optreedt bij volumefracties die 1% hoger zijn dan de evenwichtswaarde kan worden gebruikt voor een precieze bepaling van het vriespunt van een experimenteel systeem.

Curriculum Vitae

The author of this thesis was born on December 1 1972 in Stuttgart, Germany. After finishing high school (1992) he studied Physics at the University of Konstanz, Germany. During his studies, in 1994/95, he spent one year as a exchange student at the University of Bristol, United Kingdom. In the course of 1995–6 he gained some months' experience in industry, working in the research and technical sales departments of Robert Bosch GmbH in Stuttgart. For his diplom project he joined the group of Prof. R. Klein (at Konstanz University), where he studied wall effects on the dynamics of a single colloidal particle and on the structure of a colloidal dispersion. He graduated in January 1999, but by November 1998 had already moved to the FOM-Institute for Atomic and Molecular Physics in Amsterdam, where he started to work on this PhD project in the computational physics group of Prof. D. Frenkel.

Acknowledgments